MICROMAGNETIC STUDY OF HEAT ASSISTED MAGNETIC RECORDING USING RENORMALIZED MEDIA CELLS

A DISSERTATION
SUBMITTED TO THE FACULTY OF THE GRADUATE SCHOOL
OF UNIVERSITY OF MINNESOTA
BY

PIN-WEI HUANG

IN PARTIAL FULFILLMENT OF THE REQUIREMENTS
FOR THE DEGREE OF
DOCTOR OF PHILOSOPHY

RANDALL VICTORA, ADVISOR

MAY, 2014

Acknowledgements

I would like to use this opportunity to express my sincere thanks and gratitude to those many people who have guided, helped, advised, and supported me during my Doctoral studies.

First and foremost, I would like to thank my thesis advisor, Professor Randall Victora, for opening the door for me in the field of magnetic recording and leading me through it. My work would not have been possible without him. As a thesis advisor, he has been a source of inspiration for the past four years, providing precious insight and constructive criticism to the research that I have worked on. His never-diminishing passion and enthusiasm for the field of magnetic recording have encouraged and inspired me so much, especially when I faced difficulties in the research. As a teacher and a friend, he has also shown me how a boss, a scientist or a person with righteousness and integrity would be. It has been my great honor and privilege to be his student and work with him.

During my Ph.D period at the University of Minnesota, I have also received much knowledge, help and good advice from other faculties in MINT center such as Professor Jian-Ping Wang and Professor Beth Stadler. I am here to express my appreciation to them.

I am also very thankful to my dissertation committee members, Professor Allen Goldman, Professor Beth Stadler, and Professor Jian-Ping Wang for taking their time serving on the committee for both of my thesis preliminary and thesis final oral exams.

There are also many other people who have also contributed to my work and life during my Ph.D period. I would like to thank my colleagues and coworkers, who were Tao Qu, Yao Wang, Hweerin Sohn, Sean Morgan, Yang Dong, Ali Ghoreyshi, Sumei Wang,

Todd Klein, Yi Wang, Yinglong Feng, Angeline Klemm, Patrick Quaterman, Yipeng Jiao, Rizvi Ahmed, Xi Chen, Stephanie Hernandez, and many other friends in the MINT group that I cannot list them all here. I enjoyed the time very much working with them. I also want to express special thanks to Professor David Leon at Keuka College, who has been my very first mentor and friend since my first arrival in Minneapolis in Aug. of 2010, for his help and advice in all aspects of life during all these years.

I would also like to acknowledge Seagate Technology, for funding my research, and researchers from Seagate Technology, for valuable discussion in my research.

Finally, I would like to express my love and thanks to my parents, my wife, my brother and sister, and my brother-in-law Dr. Jerry Kao. Without their love and support in my life, I would never have gone this far.

Dedication

In dedication to my beloved parents for making me be who I am.

Abstract

Perpendicular magnetic recording is currently very near to its physical limit, making it difficult for researchers to keep the pace of the growth of areal density of hard disk drives. Heat-assisted magnetic recording (HAMR) is considered to be the next generation technology for magnetic recording beyond 1 Tb/in^2. Complete understanding of HAMR processes is necessary to optimize the design parameters. In this thesis, current state-of-the-art modelling methods are developed aiming at HAMR recording. First a simple torque-based method for calculating the transient behavior of temperature-dependent magnetic anisotropy is introduced. By using this method several physical quantities at finite temperature including effective anisotropy, anisotropy field, and their fluctuations are obtained. A composite grain that includes a high Curie temperature soft layer can reduce the anisotropy fluctuations. Then a new scheme for the simulation of HAMR that systematically includes fluctuating material properties above a predefined length scale, while retaining magnetostatic interactions is introduced. Renormalized media parameters, M_s, K_u, A_ex and α, suitable for useful length scales, are found numerically. These renormalized parameters are then used to model the Voronoi-cell-composed medium in the HAMR simulation. Transition jitters are obtained under various conditions. The results show that moderate maximum temperature of the heat spot, intergranular exchange coupling, media thickness of at least 10 nm, nonzero canting angle of the head field, relatively low head velocity, and large head-field strength are helpful for a successful recording. This scheme of HAMR simulation is used to find the dependencies of recording performance on the grain size and damping. The simulated results are used to compare with

an experimental demonstration. Finally, composite FeRh/FePt for HAMR media is investigated with micromagnetic simulation. It is found to potentially lower recording temperature, while retaining high anisotropy field gradient. The transition width is predicted to depend on the media cooling rate. The thickness of the FeRh layer and the applied field can significantly affect the switching time of FePt layer, and therefore alter recording performance. Applied field magnitudes and angles are identified that allow successful switching within 100 pS. It is shown that by using up to 15 nm of FeRh with 6 nm of FePt, the jitter for 5.6 nm grains can be nearly equal to the grain-size limited value, for head velocities as high as 20 m/s.

Table of Contents

Acknowledgements i

Dedication iii

Abstract iv

List of Tables viii

List of Figures ix

1. INTRODUCTION 1

1.1 Origins of Magnetism.....2

1.2 Challenges of Ultrahigh Density Recording 5

1.3 The Origin and Working Principle of HAMR.....6

1.4 Media Development of Materials for HAMR 8

1.5 Medium Noise in HAMR.....11

1.6 Transducer and Thermal Profile in HAMR.....20

1.7 Other Techniques: BPM+HAMR, SMR+HAMR, ECC+HAMR.....22

1.8 Thesis Outline.....25

2. MODELING METHODS – MICROMAGNETIC SIMULATION.....26

2.1 Energy Terms 27

2.2 Landau-Lifshitz-Gilbert Equation 32

2.3 FFT-based Calculation of Magnetostatic Fields 34

3. MAGNETIC ANISTORPY AT FINITE TEMPERATURES.....41

3.1 Modeling Method.....42

3.2 Results 46

3.3 Conclusion 52

4. SIMULATION OF HAMR USING RENORMALIZED MEDIA CELLS 53

4.1 Modeling Method 54

4.2 Magnetic Recording 63

4.3 Conclusion 74

4.4 Appendix 75

5. GRAIN SIZE DEPENDENCY, ENHANCED DAMPING, AND A SIMULATION/EXPERIMENT COMPARISON 76

5.1 Enhanced Damping and Residual Magnons 77

5.2 Grain Size Dependency 79

5.3 Simulation/Experiment Comparison 81

5.4 Conclusion 83

6. APPROACHING THE GRAIN-SIZE LIMIT FOR JITTER USING FERH/FEPT IN HAMR 84

6.1 Modeling Method 86

6.2 Transition Width Estimates 87

6.3 Switching Times 90

6.4 Recording Simulations 93

6.5 Conclusion 95

7. SUMMARY 97

BIBLIOGRAPHY 98

APPENDIX 112

List of Tables

Table 1.1 List of intrinsic properties of high anisotropy magnetic materials 11

Table 4.1 Temperature categories and corresponding fitting rules of the renormalized material parameters 66

List of Figures

Figure 1.1 Cartoons which illustrate how an HDD works 2

Figure 1.2 Paramagnetic (upper) and ferromagnetic (lower) spin moments 3

Figure 1.3 Hysteresis loop, *M* vs. *H*, for a ferromagnetic sample 4

Figure 1.4 Diagram of the trilemma in magnetic recording 6

Figure 1.5 Illustration of the working principle of HAMR 7

Figure 1.6 Two schemes of heat-assisted magnetic recording. (a) magnetically dominant scheme, and (b) optically dominant scheme 8

Figure 1.7 A typical perpendicular magnetic medium of columnar Voronoi grains 10

Figure 1.8 A cross-sectional view of a typical HAMR medium 10

Figure 1.9 The dependence of T_c on the particle size 11

Figure 1.10 Illustrations of microtracks with grain size distributions. (a) w/o distribution; (b) w/ distribution 15

Figure 1.11 Magnetization transition profile for different grain size distribution 15

Figure 1.12 The medium SNR as a function of normalized standard deviation for H_K and T_c 16

Figure 1.13 Schematic of the quadrilemma of magnetic recording 19

Figure 1.14 Thermal modeling for in-plane and out-of-plane thermal conductivities 22

Figure 2.1 Schematic of the magnetic sample of rectangular shape for demagnetization field calculation 35

Figure 3.1 Scatter plot of in-plane anisotropy torque vs. sin2θ. The white straight line is the linear regression line 45

Figure 3.2 Simulation results for the temperature dependence of uniaxial anisotropy. The solid line is for eye guidance 46

Figure 3.3 Comparison of predicted $K(T)$ - M^{ρ} between simulated results and Callen-Callen theory with $\rho = 3$ 47

Figure 3.4 Temperature dependence of (a) anisotropy field, (b) field fluctuations and (c) their ratio.....48

Figure 3.5 Single-sided amplitude spectrum of a time-domain anisotropy at T = 650 K.....49

Figure 3.6 Finite size effect of the anisotropy and its fluctuations at T = 650 K.....50

Figure 3.7 Schematic diagrams of composite and homogeneous materials 51

Figure 4.1 Schematic for the simulation of HAMR. The atomic spins are coarse-grained into renormalized block spins that are used for the elements of a 3-D grid mapped into Voronoi medium grains 54

Figure 4.2 Linear relationship between $\langle H_{\mathrm{K}} \rangle_0$ and $\langle M \rangle_0$ near T_{c} of a 6^3 nm^3 FePt cubic grain.....57

Figure 4.3 Renormalized Parameters as functions of temperature and length scale. (a) Gilbert damping parameter; d represents different length scales; “agg” is equal to the number of atomic spins in aggregation. (b) Saturation magnetization. (c) Anisotropy constant. (d) Exchange stiffness parameter 59

Figure 4.4 Average switching times of a 6^3 nm^3 FePt cubic grain as functions of applied field at different length scales 63

Figure 4.5 (a) Layout of MR read head and the recording medium. The downtrack direction is along the x-axis. (b) Recorded magnetization (M_z) pattern with base conditions as described in the text. (c) The readback signal of (b) with the readhead specified in (a). (d) The heat spot with T_{max} = 850 K and FWHM = 40 nm.. The graded area is of the range [700K, 850K].....68

Figure 4.6 Effect on T_{max} on transition jitter and the amplitude noise of readback signal. The dotted horizontal line indicates σ_{grain} casued by the Voronoi structure only, which is 1.07 nm. A_{int} denotes the intergranular exchange coupling.....70

Figure 4.7 Effect of v on transition jitter and the amplitude noise of readback signal. The hollowed symbols represent the thicker (12 nm) medium, while solid ones represent the 6 nm medium.....72

Figure 4.8 Effect of θ on transition jitter and the amplitude noise of readback signal 73

Figure 4.9 Effect on H^{appl} on transition jitter and the amplitude noise of readback signal.....74

Figure 5.1 Renormalized damping constant, starting with 0.005 and 0.02, as a function of temperature. The renormalized length scale is 1.5 nm.....77

Figure 5.2 Transition jitter versus grain pitch with two different sets of modified renormalized damping constants.....80

Figure 5.3 (a) Square-wave recorded patterns at different grain sizes. The red lines at the edges of the patterns are drawn to roughly measure the resultant write widths (red words). (b) Square-wave recorded pattern with average grain pitch of 10.6 nm 81

Figure 5.4 DC SNR rolls off with decreasing write field 83

Figure 6.1 Switching probabilities at various anisotropy fields and temperatures. Although the distribution of P_{sw} is narrower for Fe/FePt grain, the H_K gradient with temperature is much smaller than FePt 85

Figure 6.2 (a) Switching probabilities as a function of temperature (T_{rev}) at which fields reverse directions with different cooling rates. H_{appl} is 12 kOe at a 45° angle. (a) 256 6×6×6 nm^3 FePt grains. Switching probabilities as a function of T_{rev}. H_{appl} is 12 kOe at a 45° angle. (b) 256 6×6×21 nm^3 FeRh(15nm)/FePt(6nm) grains 88

Figure 6.3 The temperature differences between high (P_{90}) and low (P_{10}) switching probabilities at various cooling rates for FePt and composite FeRh/FePt grains 89

Figure 6.4 Applied-field-dependent (a) average switching times of a 96×96×21 nm^3 thin film composed of composite FeRh(15nm-thick, continuous)/FePt(6^3 nm^3, granular), and (b) switching times of 6×6×21 and 6×6×13.5 nm^3 soft/hard ECC grains. Applied field angle is 45° 92

Figure 6.5 Switching time distribution on the coordinates of field magnitude and canting angle 93

Figure 6.6 Recorded patterns: (a) FePt(6nm), v = 20 m/s, σ_{jitter} = 1.22 nm; (b) FePt(12nm), v=20 m/s, σ_{jitter} = 1.14 nm; (c) FeRh(15nm)/FePt(6nm), v = 20 m/s, σ_{jitter} = 0.98 nm 95

CHAPTER 1. INTRODUCTION

Hard-disk drives (HDDs) have come a long way over the past 58 years (up to the year 2014) since IBM, in 1956, built the very first commercial hard-disk drives (known as RAMAC) which were able to store 5 megabytes of information on 50 aluminum platters (24 inches in diameter). Storage capacity has jumped multiple orders of magnitude due to various innovations, with the achievement that today's desktop PCs are capable to be equipped with 3.5-inch HDDs containing up to 6 terabytes with a 7200-rpm spindle speed [1]. With the help of giant magneto-resistive (GMR) read heads [2], perpendicular magnetic recording (PMR) schemes [3], and exchange-coupled composite (ECC) media [4], the average annual growth rate of areal density had been about 41% from 1956 to 2010. However, GMR and PMR (including ECC) have almost led the areal density to the physical limit (750 Gb/in^2) in around 2010. According to International Data Corporation (IDC), the areal density annual growth rates have slowed and are predicted to be less than 20% from 2011 to 2016. Looking forward, the next generation of HDDs after 2016 will most likely be, in chronological sequence, two-dimensional magnetic recording (TDMR) [5], heat-assisted magnetic recording (HAMR) [6], and bit-patterned media (BPM) [7], [8] to reach 1 Tb/in^2 and beyond. Figure 1.1 is a cartoon schematically illustrating how an HDD works. As can be seen on the right-hand side of Figure 1.1, there is an inductive write head that generates fields to alter the magnetization directions of grains. Adjacent to the write head is a GMR read head, picking up the magnetic flux from those recorded bits in the recording medium. Note that every recorded bit is perpendicularly aligned. The soft underlayer is to

enhance the vertical component of the write field. The left-hand side of Figure 1.1 shows how the bits and tracks are arranged on the medium. It can be seen that tracks are supposed to be isolated to avoid any interference. Because the written pattern on the two edges of a track is often very noisy, the reader width is generally made shorter than the writer width to exclude the edge noise.

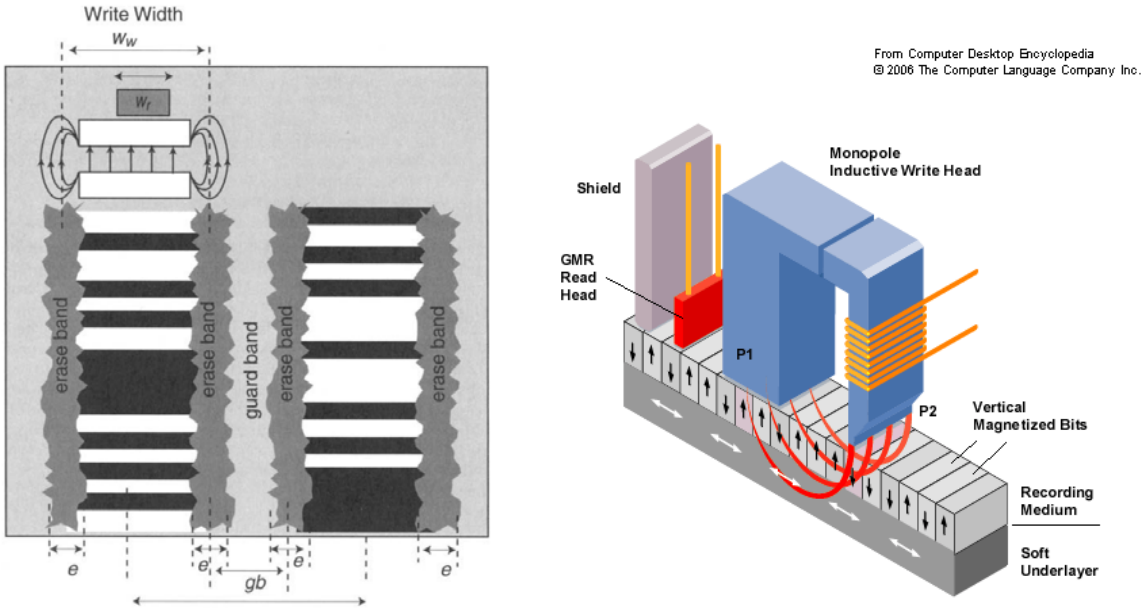

Figure 1.1: Cartoons which illustrate how an HDD works.
(Left: Ref. 9; Right: From *Computer Desktop Encyclopedia*.)

1.1 Origins of Magnetism

Magnetism originates from localized polarization of the electron clouds of certain atoms, where electrons are unpaired in the orbitals of the atoms. This causes the electrons on the atom to have a net angular momentum. The net angular momentum then generates a magnetic field that has a unified direction of flow. Any other spins that experience the field will have a tendency to align themselves with the field. When atoms are brought

together within an atomic distance, there is a probability of an electron to hop from one atom to another. This is known as the Heisenberg exchange interaction [10]. The interaction then causes the spin moments of the atoms to align parallel or anti-parallel. In most materials the spin moments are small and aligned at random, known as paramagnetism; however, in certain materials such as transition elements (nickel, cobalt and iron), the spin moments are large and align in parallel, known as ferromagnetism. Figure 1.2 depicts the schematic diagram of paramagnetism and ferromagnetism.

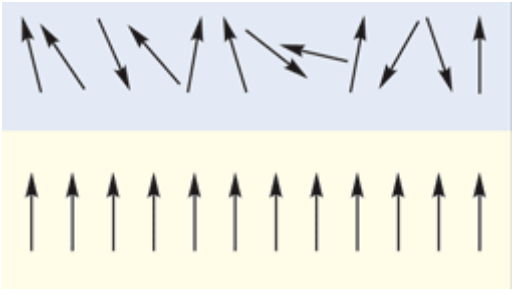

Figure 1.2: Paramagnetic (upper) and ferromagnetic (lower) spin moments.

Hysteresis Loop and Domains

For a ferromagnetic sample, the magnetization M of the sample is defined as the sample's total magnetic moment divided by the sample's volume, with unit $\mathrm{emu/cm^3}$ in the CGS system. The magnitude of M depends on material species, temperature, shape of the sample, and magnetic field etc. When a magnetic field is exerted on the sample, the magnetization will react to the field, H, following a loop called a hysteresis loop, as shown in Figure 1.3. From the hysteresis loop, several critical parameters can be extracted to characterize the magnetic sample. For example, M_r and M_s represent the remanent

magnetization ($H = 0$) and saturation magnetization (large H) respectively. H_c is termed the coercive field that measures the difficulty of demagnetizing the sample. Materials with large H_c and M_r are called hard magnets, while those with small H_c and M_r are called soft magnets. When the temperature of the ferromagnetic sample is increased to or beyond a critical temperature, the Curie temperature T_c, the sample will turn into a paramagnet. The behavior of magnets can be described by the four fundamental parameters, M_r, M_s, H_c, and T_c.

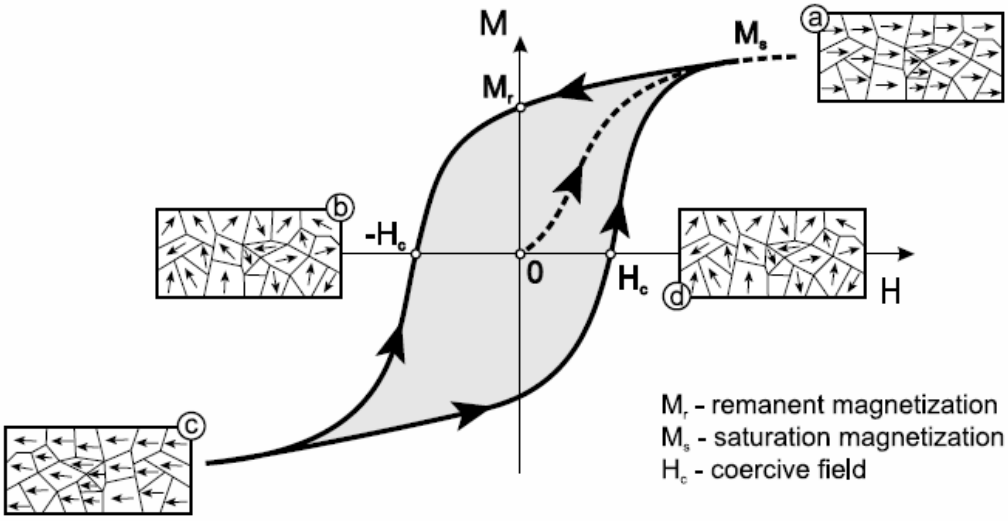

Figure 1.3: Hysteresis loop, ***M*** vs. ***H***, for a ferromagnetic sample.
[Source: http://www.fy.chalmers.se/edu/lab/labpm/em4_magnetic_hysteresis.pdf]

When a magnet is magnetized, there is always a field generated inside the magnet attempting to oppose the magnetization of the magnet, and therefore the magnetostatic energy is increased. This field is known as demagnetization field H_d, which is produced by the un-neutralized magnetic charges existing on the surface or within the magnetic body.

Domains are then formed as a consequence of minimizing the total energy, the sum of magnetostatic energy (stored in the demagnetization field) and domain wall energy (will be mentioned shortly). Therefore a normally sized ferromagnetic material is mostly demagnetized in its natural state, i.e., without any external field exerted. From domain to domain there are domain walls with finite lengths. As the magnet shrinks to a smaller size, the number of domains (and therefore domain walls) will decrease. There exists a critical size of magnet below which no domain wall can be accommodated inside the magnet, leading to a single domain particle. If the grain size is kept shrinking, the grain will eventually be thermally unstable, known as superparamagnetism, and the time averaged magnetic moment will vanish.

1.2 Challenges of Ultrahigh Density Recording

In magnetic recording, there is a prevailing consensus that any design methodology is to tackle (or find trade-offs in) a well-known "trilemma," as shown in Figure 1.4. Firstly, we know that a bit is generally composed of many tiny grains, and increasing the areal density means shrinking the bit size. To maintain available signal-to-noise ratio (SNR), the number of grains N comprising a bit needs to be constant. Therefore smaller magnetic grains are necessary. However, since the information stored in a grain is required to be stable at room temperature for at least 10 years, $K_{\mathrm{u}}V$ has to be larger than 60 $k_{\mathrm{B}}T$, where K_{u} is the magnetic crystalline anisotropy and V is the grain volume. As the grain volume V is shrunk to meet the requirement of keeping N constant, the anisotropy K_{u} has to increase. However a grain with large K_{u} means a large coercive field H_{c}, requiring a larger

write field for reversing the magnetization of the grain. Unfortunately, the maximum write fields are limited to about 1.7 T in today's write head technology.

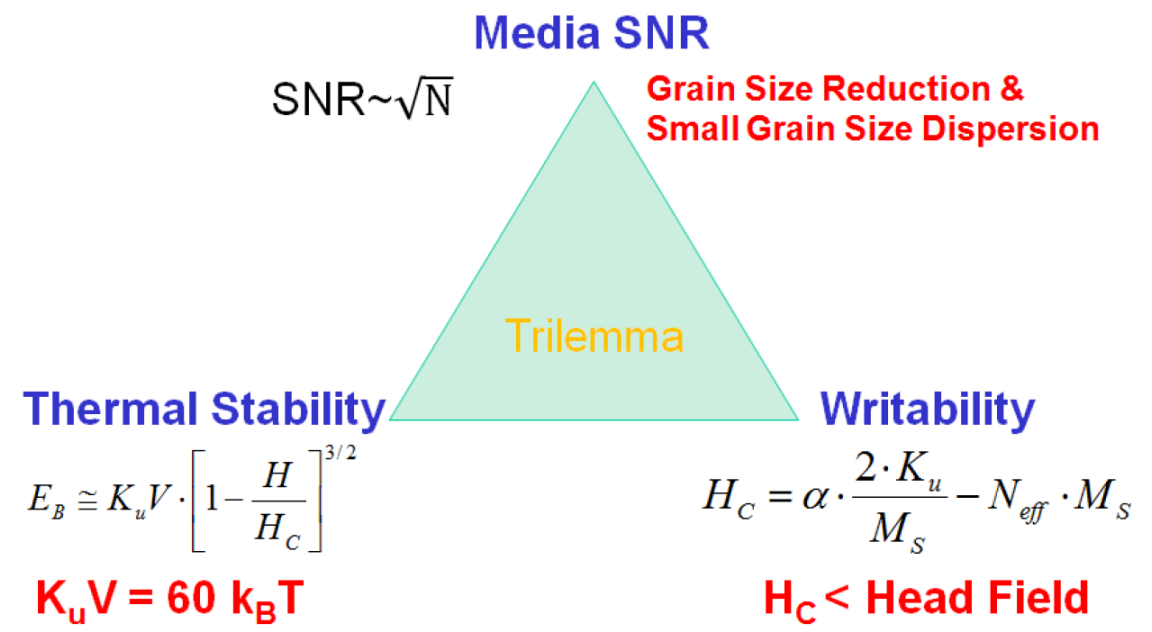

Figure 1.4: Diagram of the trilemma in magnetic recording.
[Source: Hweerin Sohn, doctoral dissertation, UMN, 2012]

1.3 The Origin and Working Principle of HAMR

Heat-assisted (or thermally-assisted) magnetic recording (HAMR) is a writing scheme in which a laser heats a bit as it is magnetized. It is aimed at solving the trilemma described in Sec. 1.2 by controlling another degree of freedom of grains, the temperature. The working principle of HAMR is illustrated in Figure 1.5. As can be seen, the coercivity of magnetic grains is known to decrease with increasing temperature. Therefore by temporarily heating the media during recording processes, information can be written on the grains with ultrahigh room-temperature coercivity by available write head fields. Then

the heated grains are rapidly cooled with field pointing in a desired direction, by which information is stably recorded on the media.

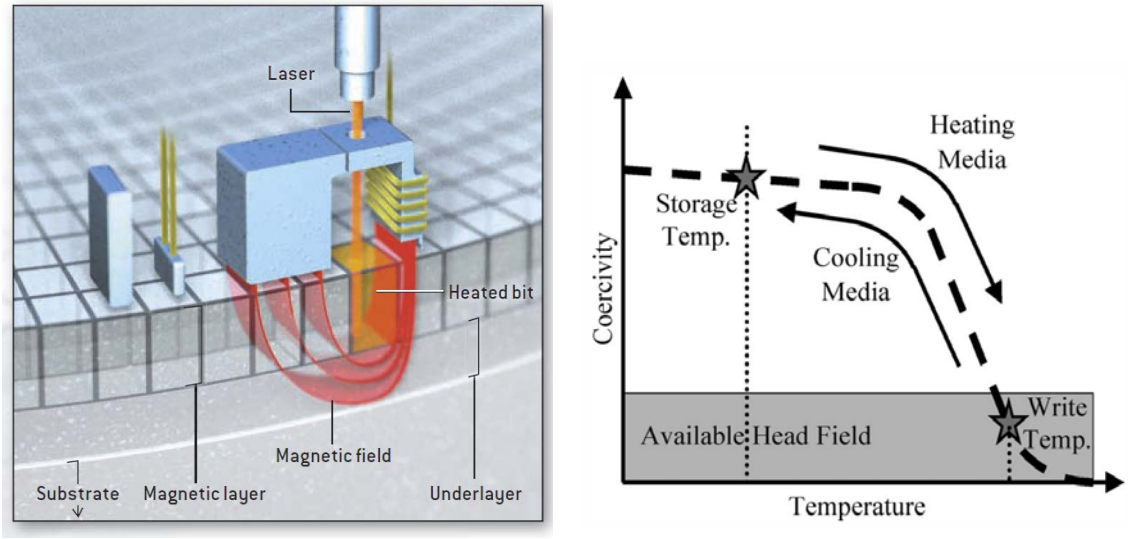

Figure 1.5: Illustration of the working principle of HAMR.
(Left: Fischetti, *Scientific American* (2006); Right: Ref. 6.)

HAMR used to have an alternative name, hybrid recording, as it combines the localized write field with thermal writing in magneto-optical (MO) recording. The idea of using optically-delivered heat to assist the switching of magnetic grains with high room temperature coercivity in magnetic recording was first proposed by Kryder [11] in 1993 and was later discussed in more details by several groups [12], [13]. There are roughly two forms of this technique, as illustrated in Figure 1.6. The light is delivered via either a far-field (Figure 1.6a) or a near-field (Figure 1.6b) delivery system. In Figure 1.6a the optical spot region is much larger than the write field region so that the written area is defined by the write field, whereas in Figure 1.6b the field region is larger than the optical region and therefore defines the written area. To increase areal density, we can either make the optical

spot or the field region as small as possible, resulting in magnetically-dominant or optically-dominant performance of recording. The best case would be for both of the regions to be made small.

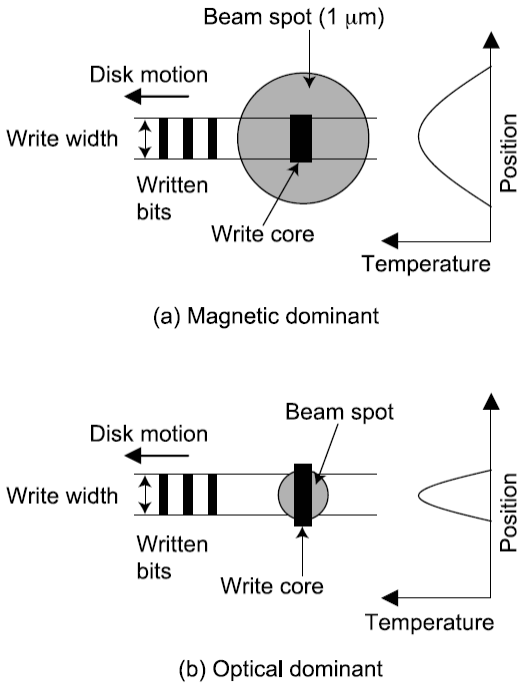

Figure 1.6: Two schemes of heat-assisted magnetic recording. (a) magnetically dominant scheme, and (b) optically dominant scheme. [Source: Ref. 14]

1.4 Media Development of Materials for HAMR

High Anisotropy Media

Generally, recording media for ultrahigh density recording require 1) high anisotropy, 2) high remanent magnetization (for readback signal), 3) nearly square hysteresis loop (for sharp transitions), and 4) uniform, small, and magnetically isolated magnetic grains packed

in a smooth surface.

The recording layer of the media, conventionally, is composed of many magnetically hard ferromagnetic grains with a columnar cell geometry resembling Voronoi cells [15], as can be seen in Figure 1.7 [16]. The cross-sectional view of a typical HAMR media is plotted in Figure 1.8 [6]. Since HAMR is aimed at realizing up to 4 Tb/in^2 density of magnetic recording, the grains have to be made smaller than 6 nm in size. Therefore high anisotropy (and thus high ordering) materials are needed. Materials such as $L1_0$-ordered FePt, FePd, CoPt and MnAl are considered to be potential candidates [6]. Multilayer structures such as Co/Pt and Co/Pd are another potential class of high anisotropy materials [17], [18]. $SmCo_5$ and $Fe_{14}Nd_2B$ are rare-earthed class of materials which also display ultrahigh anisotropy. However, mostly, the rare earth elements (Sm and Nd) have high affinity for oxygen and will cause the magnets to corrode quickly in air within several hours or days [19], [20], hindering its practical application. Table 1.1 shows the intrinsic magnetic properties of these hard ferromagnets [21], in which the minimum diameter D_p is calculated by requiring the thermal energy barrier

$$E_\mathrm{B} = K_\mathrm{U} V \left(1 - \frac{4\pi M_\mathrm{S}}{H_\mathrm{K}}\right)^2 \tag{1.1}$$

be larger than 60 $k_\mathrm{B}T$. The grain volume V is assumed the volume of a cylindrical grain with height 10 nm. Among the above-mentioned ferromagnets, $L1_0$ FePt (001) is currently considered to be the most feasible and promising one for HAMR recording media. The Curie temperature T_c of FePt can be varied by doping with Ni or Cu at the expense of reducing anisotropy [22], [23]. In addition to doping, particle size would alter the chemical

ordering and exchange energy, and therefore influence T_c [24], [25], as shown in Figure 1.9.

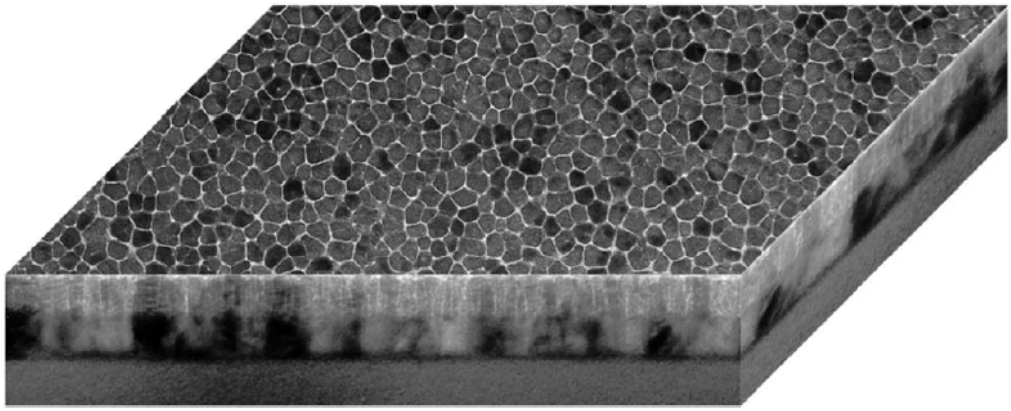

Figure 1.7: A typical perpendicular magnetic medium of columnar Voronoi grains. [Source: Ref. 16]

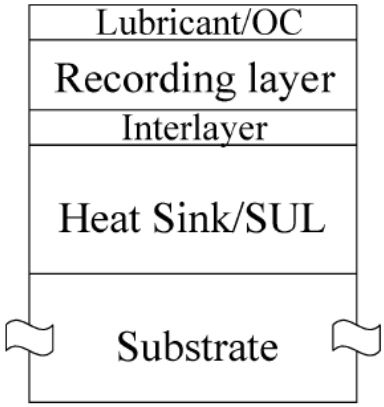

Figure 1.8: A cross-sectional view of a typical HAMR medium. [Source: Ref. 6]

Type	Material	K_1 (10^7 erg/cm^3)	Ms (emu/cm^3)	H_K (kOe)	Tc (K)	D_p (nm)
Co-alloy	Co_3Pt ($L1_2$)	2	1100	36	--	6.9
$L1_0$ alloys	FePd	1.8	1100	33	760	7.8
	FePt	7	1140	123	750	2.6
	CoPt	4.9	800	123	840	3.0
	MnAl	1.7	560	69	650	5.2
Multilayer	Co_2/Pt_9	1	360	56	500	6.6
Rare-earth transition metals	$Fe_{14}Nd_2B$	4.6	1270	73	585	3.7
	$SmCo_5$	20	910	440	1000	1.4

Table 1.1: List of intrinsic properties of high anisotropy magnetic materials. [Source: Ref. 21]

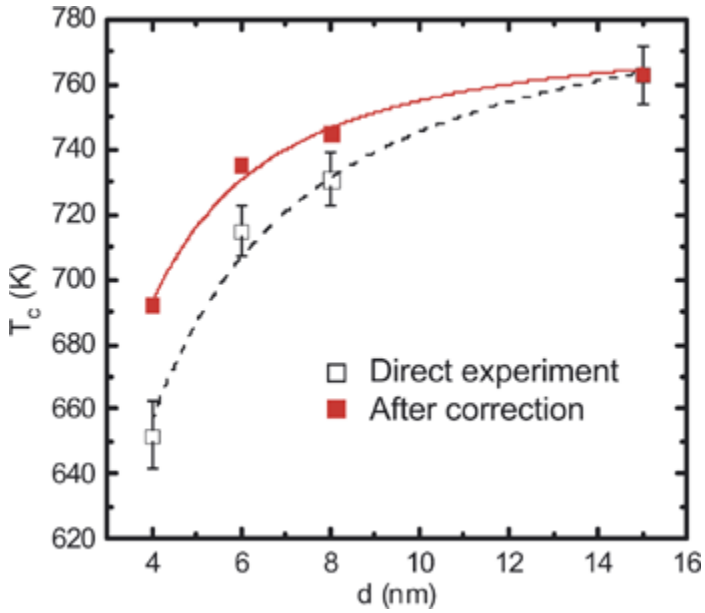

Figure 1.9: The dependence of T_c on the particle size. [Source: Ref. 25]

1.5 Medium Noise in HAMR

In almost any system, it is always the case that signals coexist with noise. Noise in magnetic recording stems from three major sources, the readback amplifier, the readback head, and the recording medium. Thanks to the advance in read head technology, readback noise is currently almost diminished to a negligible level. Nowadays the dominant noise

source is mainly from the medium [26]. Medium noise is composed of particulate noise and transition noise, where particulate noise mainly originates from medium DC noise, or modulation/amplitude noise [27]. In ultrahigh density recording, transition noise has become even more important than DC noise; therefore in this section transition noise will be primarily discussed. In conventional PMR, transition noise results largely from the variation of anisotropy fields of grains, grains' irregularity, and magnetic field distributions. In HAMR, however, the temperature T of grains will be an additional source of medium noise, so the variations of temperature-related parameters have to be taken into account.

Transition Jitter (Noise)

In this subsection, the mathematical expression of transition jitter is derived following Ref. 28, 29, and 30. Assume there are a series of microtracks as shown in Figure 1.10a. The size of grains is considered to be equal for all tracks. The relative locations of the microtracks are assumed random. The microtrack width is determined by the grain diameter D. The coercivity of the grains for i^{th} track is assumed $H_{\text{K}i}$, which is a random variable as a function of i, i.e., the distribution of coercivities is zero for the same microtrack but nonzero among different microtracks. The transition center for the i^{th} microtrack is determined by equating the net magnetic field to the coercive field of the track:

$$H_{\text{h}}(x_i) + H_{\text{d}}(x_i) = H_{\text{K}i}\,, \tag{1.2}$$

where $H_{\text{h}}(x)$ and $H_{\text{d}}(x)$ are the head field and the demagnetization field respectively. In Eq. (1.2), the distribution of $H_{\text{K}i}$ results in a distribution of the transition centers x_i. In order

to take into account the finite grain size, Eq. (1.2) should be modified into

$$H_{\mathrm{h}}(x_i-\xi)+H_{\mathrm{d}}(x_i-\xi)=H_{\mathrm{K}i}\,, \tag{1.3}$$

where ξ is a random variable with uniform distribution in [–D/2, D/2]. This is because that the transition center of magnetization on each track is always located at grain boundaries. Therefore the actual transition center is not only determined by Eq. (1.2), but also by a shift ξ to the nearest grain boundary. Eq. (1.3) can be expanded to the leading order around the average transition center x_0:

$$\left[\frac{dH_{\mathrm{h}}(x)}{dx}+\frac{dH_{\mathrm{d}}(x)}{dx}\right]\Bigg|_{x=x_0}(x_i-\xi-x_0)=H_{\mathrm{K}i}-H_{\mathrm{c}}\,,$$

$$H_{\mathrm{c}}=H_{\mathrm{h}}(x_0)+H_{\mathrm{d}}(x_0)\,. \tag{1.4}$$

In Eq. (1.4), H_{c} can also be interpreted as the mean value of the coercivity distribution $H_{\mathrm{K}i}$. Eq. (1.4) can be rearranged to give

$$x_i-x_0=\frac{H_{\mathrm{K}i}-H_{\mathrm{c}}}{\alpha}+\xi\,,$$

$$\alpha=\left[\frac{dH_{\mathrm{h}}(x)}{dx}+\frac{dH_{\mathrm{d}}(x)}{dx}\right]\Bigg|_{x=x_0}. \tag{1.5}$$

The first term on the right hand side of Eq. (1.5) shows the two competing effects from the coercivity distribution and the field gradient. The second term ξ represents the distribution due to the finite grain size. The two random variables, $H_{\mathrm{K}i}-H_{\mathrm{c}}$ and ξ, account for the distribution of the transition center x_i-x_0, whose statistical variance can be obtained basing on the variances of $H_{\mathrm{K}i}-H_{\mathrm{c}}$ and ξ. The variance of the coercivity $\sigma_{H_{\mathrm{c}}}^2$ is determined by the grains' magnetic properties. The variance of the random shift $\sigma_\xi^2=D^2/12$ can be

derived analytically because ξ is assumed uniformly distributed in [–*D*/2, *D*/2]. If the two random variables $H_{\mathrm{K}i} - H_{\mathrm{c}}$ and ξ are statistically independent, we can simply add their variances to give the variance of $x_i - x_0$

$$\sigma_x^2 = \frac{\sigma_{H_c}^2}{\alpha^2} + \frac{D^2}{12}. \tag{1.6}$$

Eq. (1.6) shows the variance of the transition center of magnetization. The response (readback) signal from a reader with width RW is an average of the contributions of N microtracks, where N equals RW/S with S being the correlation length of the microtracks in the cross-track direction. If the N microtracks are statistically independent, $S = D$. The variance of the readback signal σ_{j}^2 is then given by $\sigma_{\mathrm{j}}^2 = \sigma_x^2/(\frac{RW}{S})$. Customarily, σ_{j} is called *transition jitter*. So far the derivation is based on a constant *D* assumption. If the grain size has a distribution with mean *D* and standard deviation σ_D. A simplified model can be used to incorporate the grain size distribution into Eq. (1.6). As shown in Figure 1.10b, an additional degree of freedom is added to the width of track. The effect of grain size distribution can be considered by multiplying the second term with β, a function of σ_D/D. The change of σ_x due to β can be seen in Figure 1.11 [29].

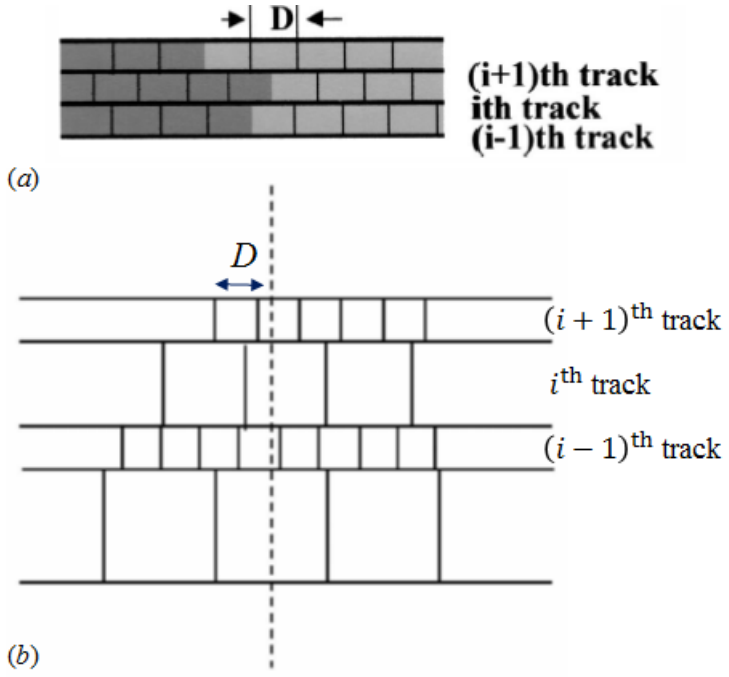

Figure 1.10: Illustrations of microtracks with grain size distributions. (a) w/o distribution; (b) w/ distribution. [Source: Ref. 28, 29]

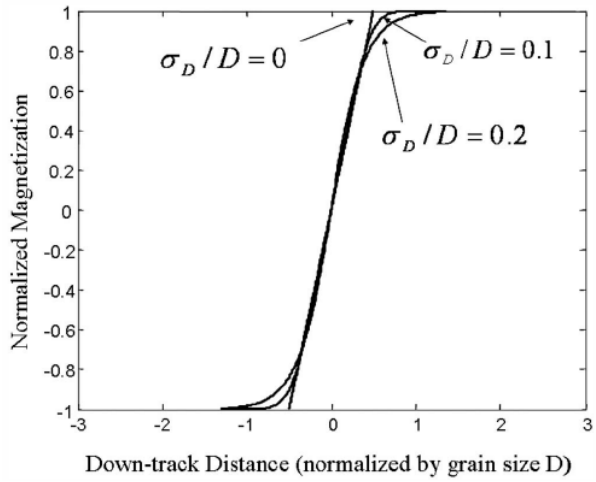

Figure 1.11: Magnetization transition profile for different grain size distribution. [Source: Ref. 29]

δT_c, δH_K and Thermal Writability

In HAMR, two of the major causes of medium noise are the variations of the

medium's Curie temperature T_c and H_K, denoted by σ_{T_c} and σ_{H_K}. The variations of H_K and T_c of $L1_0$ FePtX-Y (X=Ag, Cu; Y=C, …) media originate mainly from stoichiometry of FePt and the grain size distribution [25], [31], [32], [33]. As pointed out by Li and Zhu, the medium signal-to-noise ratio (SNR) and transition jitter are affected more by σ_{T_c} than by σ_{H_K} [34]. This is because that σ_{T_c} directly causes the variation of recording window, therefore resulting in transition jitter (σ_j). σ_{H_K}, on the other hand, influences both erasure-after-write and transition jitter. Erasure-after-write is more related to amplitude variation, or DC noise. The results are shown in Figure 1.12.

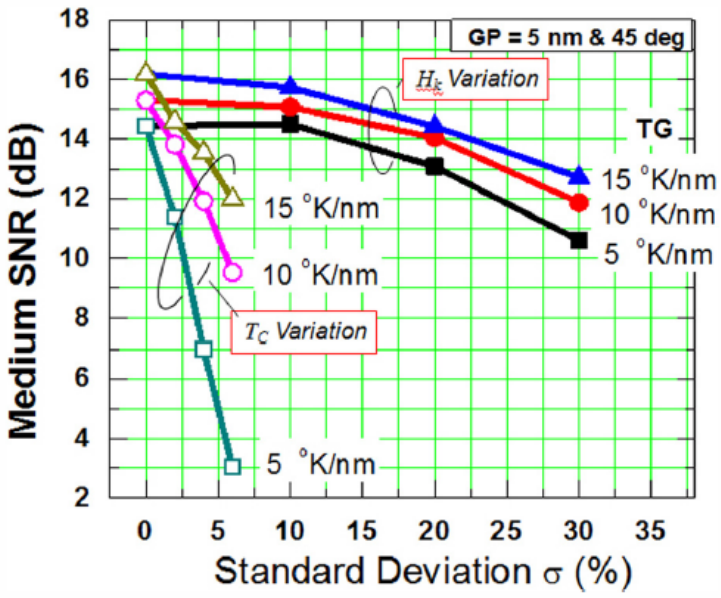

Figure 1.12: The medium SNR as a function of normalized standard deviation for $\boldsymbol{H_K}$ and $\boldsymbol{T_c}$ variation with various thermal gradients. [Source: Ref. 34]

The argument that σ_j is dominated by σ_{T_c} more than by σ_{H_K} can be seen in a simple analysis as follows. Consider the situation that the recording is taking place with one-bit-

per-grain scheme [35]. Eq. (1.6) is then written as

$$\sigma_{x,H_{\mathrm{K}}} = \frac{\partial x}{\partial H_{\mathrm{c}}}\sigma_{H_{\mathrm{K}}}$$

$$\sigma_{x,T_{\mathrm{c}}} = \frac{\partial x}{\partial T}\sigma_{T_{\mathrm{wr}}}$$

$$\sigma_x^2 = \sigma_{x,H_{\mathrm{K}}}^2 + \sigma_{x,T_{\mathrm{c}}}^2 ,$$

where

$$\frac{\partial H_{\mathrm{c}}}{\partial x} = \frac{\partial H_{\mathrm{c}}}{\partial T}\frac{\partial T}{\partial x}. \tag{1.7}$$

The subscripts H_{K} and T_{c} of σ_x indicate the position variation due to H_{K} and T_{c} variations. The write temperature T_{wr} is defined by the equation $H_{\mathrm{c}}(T_{\mathrm{wr}}) = H_{\mathrm{K}}(T_{\mathrm{wr}})$, so

$$\left.\frac{\partial H_{\mathrm{c}}}{\partial T}\right|_{T_{\mathrm{wr}}} = \left.\frac{\partial H_{\mathrm{K}}}{\partial T}\right|_{T_{\mathrm{wr}}}, \tag{1.8}$$

where $H_{\mathrm{K}}(T)$ can be roughly expressed by [36]

$$H_{\mathrm{K}}(T) = \frac{2K(T)}{M(T)} = 2\frac{K(0)\left[M(T)/M(0)\right]^2}{M(0)\sqrt{1-\left(T/T_{\mathrm{c}}\right)^{2.5}}} = \frac{2K(0)}{M(0)}\sqrt{1-\left(T/T_{\mathrm{c}}\right)^{2.5}}. \tag{1.9}$$

Assume that $K(0) = 7\times10^7$ erg/cm^3 and $\mathrm{M}(0) = 1100$ emu/cm^3, and the write head can generate a field up to 15 kOe, $\partial H_{\mathrm{K}}/\partial T = 1.89$ kOe/K at $T_{\mathrm{wr}} = 696$ K is obtained. According to the experimental data in the literature [6], [25], we use $\partial T/\partial x = 15$ K/nm, $\sigma_{H_{\mathrm{K}}} = 0.15\times H_{\mathrm{K}}$ and $\sigma_{T_{\mathrm{wr}}} \cong \sigma_{T_{\mathrm{c}}} = 0.03\times T_{\mathrm{c}}$ and therefore obtain $\sigma_{x,H_{\mathrm{K}}} = 0.08$ nm and $\sigma_{x,T_{\mathrm{c}}} = 1.4$ nm. The argument that σ_{j} is mainly dominated by $\sigma_{T_{\mathrm{c}}}$ is now verified.

If we were able to manufacture a perfect recording medium with zero $\sigma_{H_{\mathrm{K}}}$ and $\sigma_{T_{\mathrm{c}}}$ for HAMR, does that mean we could write transitions with the grain-size limited jitter? The

answer is unfortunately negative. According to Evans *et al.*, "thermal writability" will be the ultimate limiting factor to a HAMR system [37]. In Ref. 37, the ultimate recording system in which one magnetic grain is sufficient to store a binary "1" or "0" is studied. Suppose that there is an ensemble of grains representing a bit and pointing upward. Under the application of an external field pointing downward, the probability for the grains to reverse their magnetization direction (switch from upward to downward direction) can be defined as m_e. For a multi-bit-per-grain system, m_e can be interpreted as the normalized remnant magnetization in equilibrium, whereas for a one-bit-per-grain system, m_e can be interpreted as the probability that the grain switches to the direction of the external field. We also define the probability of obtaining a grain pointing downward as $P(\downarrow,+)$ *after* applying a downward external field, regardless of what direction it pointed to before the application of the field. The plus sign denotes "after." Similarly, $P(\downarrow,-)$ and $P(\uparrow,-)$are defined to represent the probabilities of the grain to point downward and upward respectively *before* the application of the field. In most cases, $P(\downarrow,-) = P(\uparrow,-) = 1/2$. Then we can write the following probability equation:

$$\begin{aligned} P_{\mathrm{sw}} \equiv P(\downarrow,+) &= P(\downarrow,+\left|\downarrow,-\right.)P(\downarrow,-) + P(\downarrow,+\left|\uparrow,-\right.)P(\uparrow,-) \\ &= 1\times\frac{1}{2} + m_e \times \frac{1}{2} = \frac{1+m_e}{2} \end{aligned} \quad . \tag{1.10}$$

Following Ref. 37, P_{sw} can be understood as the probability of the magnetization that is switched into the correct state by the field during the writing process. Since the bit error rate (*BER*) is the probability of wrongly recording the bit, we can simply write

$$BER = \frac{1-m_e}{2} = \frac{1}{2}\left[1-\tanh\left(\frac{MVH}{k_{\mathrm{B}}T}\right)\right], \tag{1.11}$$

where the normalized equilibrium magnetization m_e is expressed by a simple hyperbolic tangent function [38]. In Eq. (1.11), M and V are the magnetization and the volume of the grain, and H is the applied field. The ratio MVH/k_BT that determines the BER is named "thermal writability" by the authors of Ref. 37. Although right now we are considering the one-bit-per-grain recording system (or bit-patterned media), this BER will also be reflected in DC and transition noise in Voronoi-cell-based media. The above discussion then leads to the "quadrilemma" of magnetic recording, as shown in Figure 1.13 [37].

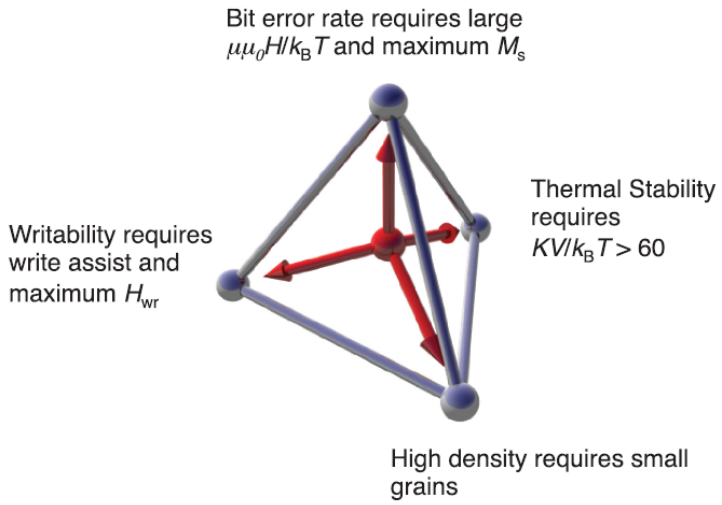

Figure 1.13: Schematic of the quadrilemma of magnetic recording. [Source: Ref. 37]

With the above consideration of the possible sources of medium noise in HAMR, an attempt to formulate and incorporate all these limiting factors into the jitter formula (6) would naturally follows. According to the work done by Wang *et al.*, the transition jitter σ_j can be formulated as [39]

$$\sigma_{\mathrm{j}} \approx \frac{\sqrt{\dfrac{\delta H_{\mathrm{K0}} f + \left(H_{\mathrm{K0}} \dfrac{\partial f}{\partial T} \delta T \right)^2 + \left(H_{\mathrm{K0}} \dfrac{\partial f}{\partial T_{\mathrm{c}}} \delta T_{\mathrm{c}} \right)^2 + \left(H_{\mathrm{K0}} \delta f \right)^2}{\left(H_{\mathrm{K0}} \dfrac{\partial f}{\partial T} \dfrac{\partial T}{\partial x} \pm \dfrac{dH_{\mathrm{c}}}{dx} \right)^2} + \gamma D^2}}{\sqrt{\dfrac{RW}{S}}}, \tag{1.12}$$

where γ is a constant determined by the distribution and geometry of irregular grains. δH_{K0} is the variation of media's zero-temperature intrinsic anisotropy field H_{K0}, δT and δT_{c} are the variations of write temperature and the Curie temperature. f is a symbolic function which depends on T, T_{c} and time (t) during the writing process. δf is used to denote the thermal-fluctuation-induced variation (also symbolic). The dynamic anisotropy field is written as $H_{\mathrm{K}} f(T, T_c, t)$. Note that the argument T of function f can have both in situ variation (δT) and spatial variation ($\frac{dT}{dx}\delta x$). In Eq. (1.12), the numerator in the square root sign is the *switching field variation* for HAMR.

1.6 Transducer and Thermal Profile in HAMR

In HAMR, the heat is delivered by light via a near-field transducer [40]. In conventional far-field optics, the light can only be focused down to $\sim 0.5\lambda/NA$, where λ is the wavelength and NA is the numerical aperture of the lens. Although in conventional near-field optics, the light spot is not limited by λ but by NA, the energy coupling efficiency is disappointingly in the order of 1×10^{-4} to 1×10^{-5}. After the discovery of extraordinary optical transmission in 1998 [41], surface plasmons (SPs) are found to be a magic carrier that can enhance the coupling efficiency by 3–4 orders of magnitude, and can

be applied to the light energy transducer for HAMR [40]. With careful designs, the transducers can deliver over 50 μW power into a spot with a diameter of 30 nm [42], although the real thermal spot size on the recording medium still depends on the fly height, medium thickness and thermal conductivity of the medium.

In HAMR, the major difference when compared to the conventional perpendicular magnetic recording is the introduction of the thermal energy. Instinctively the thermal modeling on the media and heads becomes necessary in order to study the thermal profile in the media. Several advanced treatments of the problem of heat transfer in the media, such as the Lattice-Boltzman method, have been developed [43]. The medium's thermal profile depends not only on the optical profile generated by the optical transducer, but also on the media's thermal conductivities and structures. As shown Figure 1.8, typical HAMR media are composed of multiple layers of different materials; therefore boundary thermal resistance (BTR) exists at all of the boundaries between any two layers. Due to the granular structure, the thermal conductivity of the FePt recording layer is generally expected to be smaller in the in-plane direction than in the out-of-plane direction. The measurement of the in-plane thermal conductivity $k_{\parallel}$ is much challenging than the out-of-plane thermal conductivity $k_{\perp}$ [44], [45]. For FePt media, the measured $k_{\perp}$ is around 35 W/mK [36], whereas the measured $k_{\parallel}$ for FePt granular media of 30% segregation of SiO_2 is found to be as low as 6 W/mK [44]. Figure 1.14 shows the thermal modeling results of in-plane and out-of-plane temperature distributions as functions of BTR and $k_{\parallel}$ [46].

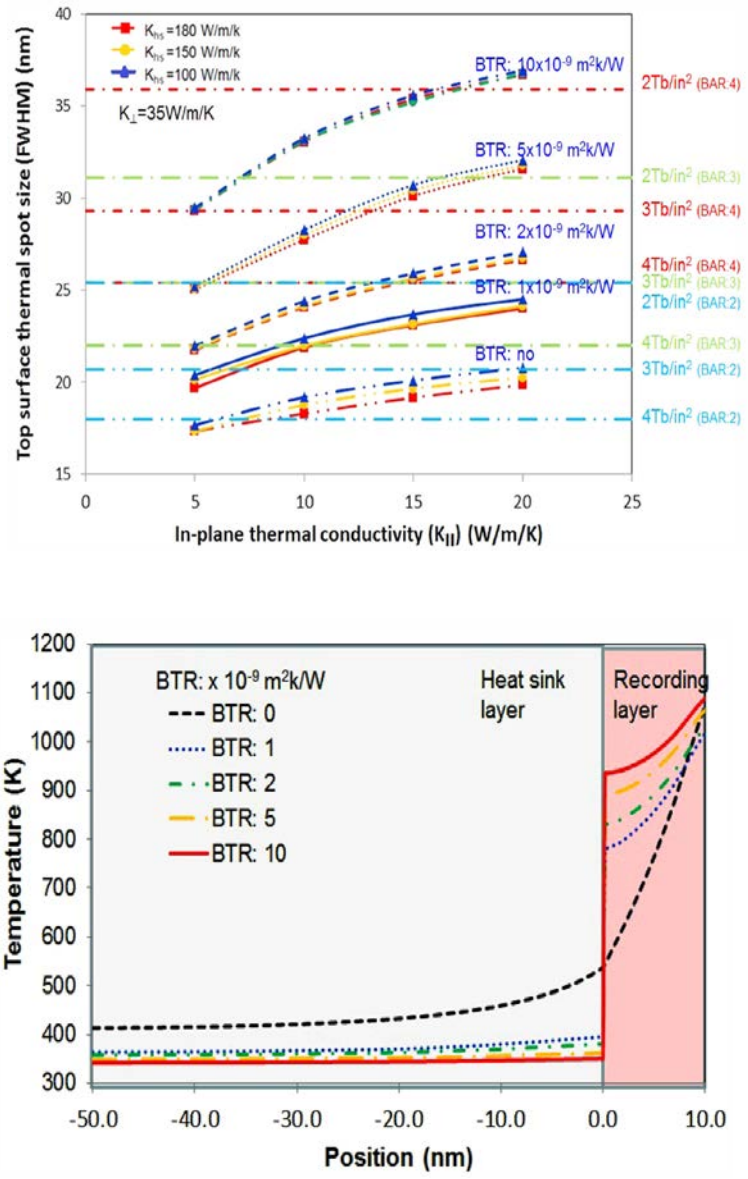

Figure 1.14: Thermal modeling for in-plane and out-of-plane thermal conductivities. [Source: Ref. 46]

1.7 Other Techniques: BPM+HAMR, SMR+HAMR, ECC+HAMR

In conventional media with a Voronoi configuration, the zig-zag transitions due to irregular grain boundaries are always a significant noise source of jitter (γD^2 in Eq. (1.12)). To reduce this zig-zag noise the reader is made 3–4 grain-diameter wide to average out the

noise. It is also known that the media SNR can be estimated to be proportional to $V_{\mathrm{bit}}/V_{\mathrm{grain}}$ [47], where V_{bit} is the bit volume and V_{grain} is the grain volume. In contrast with the conventional media for PMR where bits are composed of many tiny grains, magnetic cells (dots) can be lithographically patterned in ordered arrays, with each individual magnetic cell serving as a bit. Therefore each cell can be made larger than the normal grain in conventional media. For instance, a CoPtCr-based medium ($K_{\mathrm{u}}\sim 4\times 10^{6}$ erg/cm^3, $M_{\mathrm{u}}\sim 660$ emu/cm^3 [48]) with cells of 6×6 nm^2, 12 nm thick, and 12 nm cell-to-cell distance can give a density of 4.5 Tb/in^2. Challenges with BPM will be medium fabrication, write synchronization, and low bit-aspect ratio that imposes stringent conditions on the servo tracking system. To go beyond 4.5 Tb/in^2 one will have to use materials with ultrahigh anisotropy and will face the same problem that the coercivity of cells is higher than the maximum write field as found in continuous granular media again. Therefore it is conceptually straightforward to combine BPM with HAMR to obtain heat-assisted-bit-patterned media recording, and a certain amount of work has been done examining it [49], [50], [51], [52].

Shingled magnetic recording (SMR) is another promising technique which allows substantial increases in areal density without tremendous changes to the heads and media used in conventional hard disk drives [5]. In fact, it has been adopted in the current HDD products lately [53]. In SMR, tracks are heavily overlapped, i.e., the guard band in Figure 1.1 is shrunk to none and therefore tracks are arranged like roofing shingles. In this setup, the tracks have to be written sequentially. Therefore there is no need for a narrow pole-tip which is designed to match the track-pitch in conventional PMR. It means that a head with

larger area can be used in SMR. A simplified expression for the head fields in the medium reads $H_{\mathrm{head}} = M_{\mathrm{head}}\Omega/4\pi$, where M_{head} is the magnetization of the head and Ω is the solid angle subtended by the write pole and a certain point in the medium, indicating that much larger head fields can be achieved. Moreover, because that tracks are written sequentially, adjacent-track erasure (ATE) found in conventional recording scheme will be less an issue. In a conventional recording scheme, ATE occurs when a single track is written repetitively and ruins the immediately adjacent tracks. However, the requirement of "sequential writing" can also result in a significant disadvantage of SMR: "Update-in-place" is no longer possible [5]. Beside the shingled-writing scheme, the success of SMR requires a technique called two-dimensional readback. As can be inferred, two-dimensional readback technique is essentially a two-dimensional signal-processing. It implies that the read heads now need to resolve high-resolution information in both the cross-track and down-track directions. Singled-writing and two-dimensional readback comprise a new regime of magnetic recording, and are termed as "two-dimensional magnetic recording" or TDMR in short. SMR can be combined with HAMR to further increase the areal density. In 2014, Greaves *et al*. presented the idea of combining SMR with HAMR, and showed the possibility of achieving an ultimate areal density of 8 Tbit/in^2 [54].

1.8 Thesis Outline

The following is a general outline for the thesis. Chapter 1 summarizes the origins of magnetism and HAMR. The working principle of HAMR is also briefed. Issues of medium noise for HAMR, and transition jitter derivation are covered. Several future recording technologies related to HAMR are mentioned.

Chapter 2 will describe the modeling methods in detail, including dynamic micromagnetic simulation and relevant energy and field terms. Fast Fourier Transform (FFT) method for calculating demagnetization fields is also detailed.

Chapter 3 will present a simple method for calculating temperature- and time-dependent anisotropy field. This will be the foundation for the renormalization technique used in the chapters thereafter.

Chapter 4 is the main focus of this thesis, the "HAMR recording simulation using renormalized media cells." A new technique of implementing HAMR simulation will be shown.

Chapter 5 is basically a slight extension of Chapter 4. A more correct Gilbert damping constant and grain size dependence on recording performance will be discussed.

Chapter 6 will be focused on solving the issues and difficulties that face HAMR. With the help of FeRh as an assisting layer, we will be able to write transitions close to the grain-size limit.

The thesis will finally conclude with a summary, describing the important discoveries of the thesis, and how they can be relevant to the advance of magnetic recording industry.

CHAPTER 2. MODELING METHODS — MIRCROMAGNETIC SIMULATION

Micromagnetics started with a paper of Landau and Lifshitz on the structure of a wall between two anti-parallel domains in 1935 [55]. After 1935 Brown had published several follow-up papers around 1940, and a book with detailed treatment of micromagnetics in 1963 [56], where a continuous magnetization vector is used to describe the magnetization structure of the wall region between magnetic domains. Micromagnetics is a generic term for a wide variety of studies of magnetization structures, reversal mechanisms, and dyanmics in magnetic materials. In the early years, micromagnetics was limited to minimizing the total energy of systems with ideal geometry (sphere, ellipsoid, cylinder, etc.) to determine domain structures and nucleation fields for mechanisms of magnetization reversal. Since the mid-1980s the large-scale computer started to enable the study of more realistic problems which can be better compared with experimental data. Numerical micromagnetic modelling using the finite difference or finite element method is a quantitative way to understand the local arrangement of the magnetic moments and how it relates to hysteresis processes. One drawback of using energy minimization approaches is that it can only determine nucleation fields for the system, but does not correctly predict the state of the system after magnetization reversal. Consequently a lot of effort has gone into the development of dynamic approaches based on the Landau-Lifshitz (LL) equation of motion. In this chapter, I will describe the formulation of Landau-Lifshitz-Gilbert (LLG) equation, Landau-Lishitz-Bloch (LLB) equation, and the related energy and field terms.

All of the following can reference to any standard text book such as Ref. 57, or review articles such as Ref. 58 written by authors R. W. Chantrell, J. Fidler, and T. Schrefl and M. Wongsam.

2.1 Energy Terms

Minimizing the total Gibb's free energy with respect to the magnetization gives a stable equilibrium state of the magnetic system.

Zeeman Energy E_z

It has an alternative name, the external energy. E_z is the potential energy of a magnet in an external magnetic field, as shown in the following

$$E_z = -\int_V \vec{M}(\vec{r}) \cdot \vec{H}_{ext}(\vec{r}) d^3 r , \tag{2.1}$$

where $\vec{M}(\vec{r})$ is the magnetization of the magnet. In the CGS units, E, M, H, and r have the units of erg, emu/cm^3, Oe, and cm respectively. The negative sign in Eq. (2.1) indicates that the minimum energy occurs when the magnetization is aligned with the external field.

Anisotropy Energy

The term anisotropy refers to the phenomenon that the physical properties of a material depend on the directions in which they are measured. In magnetism, anisotropy means the preference for the magnetization to lie in a particular direction in a sample. There are several mainly origins as follow:

a) *Magnetocrystalline anisotropy*. This is the only intrinsic contribution from the material. The origin of the magnetocrystalline anisotropy is at the atomic level. The local neighborhood determines the preferential direction of the magnetic moment. In the

language of quantum mechanics, it is called spin-orbit coupling. In general, it is known that the larger the atomic number, the stronger the coupling between the spin and orbital momenta. Therefore the alloys such as FePt, FePd, and CoPt have much higer magnetoscrystalline anisotropy than other materials. Because the non-spherical shapes of electron orbits, the spin-orbit coupling results in preferred directions for the spin moment, and therefore the magnetization. These directions are called the *easy directions*. The energy required for the spin moment to deviate from these easy directions is called anisotropy energy.

i) Uniaxial anisotropy energy — occurs in hexagonal close-packed crystals, such as cobalt, or certain cobalt-alloys and iron-alloys.

$$E_{\text{ani}} = K_{\text{u}} V \sin^2 \theta + \text{h.o.t.}, \tag{2.2}$$

where θ is the polar angle between the easy axis and the magnetization.

ii) Cubic anisotropy energy — occurs in cubic crystals, such as body-centered cubic iron or face-centered cubic nickel.

$$E_{\text{ani}} = K_0 V + K_1 V(\alpha_1^2\alpha_2^2 + \alpha_2^2\alpha_3^2 + \alpha_1^2\alpha_3^2) + \text{h.o.t.}, \tag{2.3}$$

where α is the direction consine. The proportional consants K's are material- and temperature-dependent.

b) *Shape anisotropy*. This is the energy originates from magnetostatic interaction. According to two of Maxwell's equations, the universal $\nabla \cdot \vec{B} = 0$ and $\nabla \times \vec{H} = 0$ if there is no current source and varying electric field. $\vec{B}$ denotes the magnetic-flux density and $\vec{H}$ is the derived macroscopic magnetic field. Helmholtz's theorem ensures

that the vanishing curl gives $\vec{H} = -\nabla\phi_{\mathrm{m}}$, where ϕ_{m} is a magnetic scalar potential. With the constitutive relation $\vec{B} = \vec{H} + 4\pi\vec{M}$, we have a Poisson's equation

$$\nabla^2\phi_{\mathrm{m}} = \nabla\cdot\vec{M}\,. \tag{2.4}$$

An integral solution to Eq. (2.4) can be derived

$$\vec{H}(\vec{r}) = -\frac{1}{4\pi}\iiint d^3r'\left[\nabla'\cdot\vec{M}(r')\right]\frac{\vec{r}-\vec{r}'}{\left|\vec{r}-\vec{r}'\right|^3} + \frac{1}{4\pi}\iint d^2r'\left[\hat{n}'\cdot\vec{M}(r')\right]\frac{\vec{r}-\vec{r}'}{\left|\vec{r}-\vec{r}'\right|^3}, \tag{2.5}$$

where the bracketed terms can be interpreted as magnetic surface poles and volume charges. Shape anisotropy is therefore the consequence of the combining effect of $\vec{H}$ and $\vec{M}$ in Eq. (2.5). Now consider a uniform magnetized sample. The shape of the sample determines the distribution of the surface poles, which generate a "demagnetization field" that opposes $\vec{M}$. Instead of Eq. (2.5), the demagnetization field $\vec{H}_{\mathrm{d}}$ is usually written as $\vec{H}_{\mathrm{d}}(\vec{r}) = -\overleftrightarrow{N}_{\mathrm{d}}(\vec{r})\cdot\vec{M}$, where $\overleftrightarrow{N}_{\mathrm{d}}(\vec{r})$ is a second-rank tensor and depends on the observation point. The tensor has the form as follows

$$\begin{bmatrix} N_{\vec{r}}^{xx} & N_{\vec{r}}^{xy} & N_{\vec{r}}^{xz} \\ N_{\vec{r}}^{yx} & N_{\vec{r}}^{yy} & N_{\vec{r}}^{yz} \\ N_{\vec{r}}^{zx} & N_{\vec{r}}^{zy} & N_{\vec{r}}^{zz} \end{bmatrix}, \tag{2.6}$$

with

$$N_{\vec{r}}^{xx} + N_{\vec{r}}^{yy} + N_{\vec{r}}^{zz} = 4\pi \quad (\text{in CGS})\,. \tag{2.7}$$

Taking an ellipsoid for clarification purposes, the shape anisotropy energy can be shown as

$$E_{\mathrm{d}} = -\frac{1}{2}\int_V \vec{H}_{\mathrm{d}}\cdot\vec{M}d^3r = -K_{\mathrm{shape}}V\sin^2\theta\,, \tag{2.8}$$

where

$$K_{\text{shape}} = \frac{1}{2}(N^{zz} - N^{xx})M^2. \tag{2.9}$$

Note that N^{zz} and N^{xx} depend on the long and short axes of the ellipsoid, and are independent of $\vec{r}$. For a sphere, $K_{\text{shape}} = 0$. The ½ factor in Eq. (2.8) is introduced to avoid double counting the energy between two magnetized elements.

Exchange Energy

The exchange energy originates from short-range couplings among spins neighboring to each other, which can be described by the classical Heisenberg spin model. The classical Heisenberg spin Hamiltoian takes the form

$$E_{\text{exch}} = -\sum_{i \neq j} J_{ij} \vec{S}_i \cdot \vec{S}_j, \tag{2.10}$$

where $\vec{S}_i$ is the magnetic spin moment of spin i, and J_{ij} is the exchange coupling constant which depends on material species. If we set the energy of the state with all spins aligned to be zero, and assume isotropic nearest neighbor couplings, the exchange energy can be written

$$\begin{aligned} E_{\text{exch}} &= -J \sum_{i,j;i\neq j}^{N.N.} S^2 - \vec{S}_i \cdot \vec{S}_j = -J \sum_{i,j;i\neq j}^{N.N.} S^2 - \vec{S}_i \cdot (\vec{S}_i + \Delta\vec{S}_{ij}) \\ &= J \sum_{i,j;i\neq j}^{N.N.} \frac{(\Delta\vec{S}_{ij})^2}{2}, \end{aligned} \tag{2.11}$$

after the following mathematical treatment

$$
\begin{aligned}
&(\vec{S}_i + \Delta\vec{S}_{ij})^2 = \vec{S}_i^2 + 2\Delta\vec{S}_{ij}\cdot\vec{S}_i + \Delta\vec{S}_{ij}^2 = \vec{S}_j^2, \\
&\Delta\vec{S}_{ij}\cdot\vec{S}_i = -\frac{\Delta\vec{S}_{ij}^2}{2}.
\end{aligned}
\tag{2.12}
$$

If the magnetization is spatially slowly varying and the lattice structure is simple cubic with lattice constant a, we can write

$$
\Delta\vec{S}_{ij} = \frac{\Delta\vec{S}_{ij}}{\Delta x_{ij}}\cdot a\,. \tag{2.13}
$$

In the continuum approximation,

$$
\begin{aligned}
E_{\text{exch}} &= \frac{JS^2}{a}\iiint_V \left(\left|\frac{\partial\vec{s}}{\partial x}\right|^2 + \left|\frac{\partial\vec{s}}{\partial y}\right|^2 + \left|\frac{\partial\vec{s}}{\partial z}\right|^2 \right) dxdydz \\
&= A'M^2 \iiint_V \left(\left|\nabla\vec{m}\right|^2 \right) dxdydz \\
&= A'M^2 \iiint_V \left(\left|\nabla m_x\right|^2 + \left|\nabla m_y\right|^2 + \left|\nabla m_z\right|^2 \right) dxdydz \\
&= A \iiint_V \left(\left|\nabla m_x\right|^2 + \left|\nabla m_y\right|^2 + \left|\nabla m_z\right|^2 \right) dxdydz,
\end{aligned}
\tag{2.14}
$$

where the small letter vectors $\vec{s}$ and $\vec{m}$ are the unit vectors. M is the magnitude of saturation magnetization. Now the exchange energy has been formulated from discrete atomic scale to continuum approximation. This lays the foundation of the formulation of micromagnetism. The exchange constant J which contains atomic properties is essentially a phenomenological constant in micromagnetic viewpoint, and can be determined experimentally.

2.2 Landau-Lifshitz-Gilbert Equation

As summarized in Ref. 58, the development of numerically micromagnetic calculations started with energy minimization approach in 1985, and has entered the era of dynamic approach since Victora's seminal paper in 1987 [59]. In Ref. 59, the dynamic approach is based on the Landau-Lifshitz-Gilbert (LLG) equation as shown below

$$\frac{d\vec{M}}{dt} = -\gamma \vec{M} \times \vec{H} + \alpha\gamma \vec{M} \times \frac{d\vec{M}}{dt}. \tag{2.15}$$

Note that in Eq. (2.15) $\vec{M}$ is assumed to be of constant magnitude and satisfies $\vec{M} \cdot \frac{d\vec{M}}{dt} = 0$. On substituting the expression again for $d\vec{M}/dt$ in the third term of Eq. (2.15), Eq. (2.15) can be written as

$$\frac{d\vec{M}}{dt} = -\frac{\gamma}{1+\alpha^2} \vec{M} \times \vec{H}_{\text{eff}} - \frac{\alpha\gamma}{1+\alpha^2} \vec{M} \times \vec{M} \times \vec{H}_{\text{eff}}, \tag{2.16}$$

where γ is the gyromagnetic ratio and α is the damping constant. $\vec{H}_{\text{eff}}$ is the effective field that governs the motion of $\vec{M}$.

In Sec. 2.1, the possible energy terms involved in a magnetic system are described. The total energy density is (assumed uniaxial anisotropy)

$$\begin{aligned} E_{\text{tot}} &= E_{\text{z}} + E_{\text{ani}} + E_{\text{d}} + E_{\text{exch}} \\ &= -\vec{M} \cdot \vec{H}_{\text{ext}} + \frac{K_{\text{u}}}{M_{\text{s}}}(M_x^2 + M_y^2) - \frac{1}{2}\vec{M} \cdot \vec{H}_{\text{d}} + \frac{A}{M_{\text{s}}^2}\left[\left|\nabla M_x\right|^2 + \left|\nabla M_y\right|^2 + \left|\nabla M_z\right|^2 \right]. \end{aligned} \tag{2.17}$$

The effective field in Eq. (2.18) can be derived from the functional derivative of the total energy density with respect to $\vec{M}$

$$\vec{H}_{\text{eff}} = -\frac{\delta E_{\text{tot}}}{\delta \vec{M}} = \vec{H}_{\text{ext}} + \vec{H}_{\text{ani}} + \vec{H}_{\text{d}} + \vec{H}_{\text{exch}}. \tag{2.18}$$

It is straightforward to show that $\vec{H}_{\text{ext}}$ is exactly the same as the externally applied field, and

$$\begin{aligned}\vec{H}_{\text{ani}} &= \frac{2K}{M_{\text{s}}}\cos\theta \\ \vec{H}_{\text{exch}} &= \frac{2A}{M_{\text{s}}^2}\left(\nabla^2 M_x\hat{x} + \nabla^2 M_y\hat{y} + \nabla^2 M_z\hat{z}\right).\end{aligned} \tag{2.19}$$

The second-order derivative in the expression of $\vec{H}_{\text{exch}}$ can be discretized into

$$\begin{aligned}\vec{H}_{\text{exch}}(i,j,k) = \frac{2A}{M_{\text{s}}^2}\{&\frac{\vec{M}(i+1,j,k)+\vec{M}(i-1,j,k)}{(\Delta x)^2} + \\ &\frac{\vec{M}(i,j+1,k)+\vec{M}(i,j-1,k)}{(\Delta y)^2} + \\ &\frac{\vec{M}(i,j,k+1)+\vec{M}(i,j,k-1)}{(\Delta z)^2}\},\end{aligned} \tag{2.20}$$

where i, j, and k are the position indices of a cubic finite difference space. For $\vec{H}_{\text{d}}$, since it is itself a function of $\vec{M}$, a different approach is adopted and will be shown in the next section. To solve Eq. (2.15), it is convenient to express $\vec{M}$ in spherical coordinates, and Eq. (2.15) will be decomposed into two differential equations with respect to zenith and azimuth angles, θ, and φ respectively. The time integration can be realized with the multi-variable Runge-Kutta numerical algorithm, where in this thesis we will use the typical 4$^{\text{th}}$-order Runge-Kutta method. At finite temperatures, there should be a thermal field term $\vec{H}_{\text{th}}$ added to the effective field term, as first proposed by Brown [60]. The form and property of $\vec{H}_{\text{th}}$ will be described in Ch. 3.

2.3 FFT-based Calculation of Magnetostatic Fields

Although Eq. (2.5) shows a closed form solution for calculating the magnetostatic field $\vec{H}_{\mathrm{ms}}$, it is usually not a good way for numerical computation. A better way of calculating the magnetostatic fields is to divide the sample into many small cells and represent each cell by a magnetic dipole placed at the center of the cell. $\vec{H}_{\mathrm{ms}}$ at a certain point in space can be calculate by summing all the dipole fields. The expression for the dipole field is

$$\begin{aligned} \vec{H}_{\mathrm{dipole}}(\vec{r}_i) &= \sum_{j\neq i} \frac{3(\vec{M}(\vec{r}_j)\cdot\hat{n})\cdot\hat{n} - \vec{M}(\vec{r}_j)}{\left|\vec{r}_i - \vec{r}_j\right|^3}, \\ \hat{n} &= \frac{\vec{r}_i - \vec{r}_j}{\left|\vec{r}_i - \vec{r}_j\right|}. \end{aligned} \tag{2.21}$$

If the sample under study is uniformly discretized, it is convenient to use the Fast-Fourier Transform (FFT) algorithm to compute $\vec{H}_{\mathrm{ms}}$. In Sec. 2.1, it is known that the demagnetization field can be written as $\vec{H}_{\mathrm{d}}(\vec{r}) = -\sum_{\vec{r}'} \overleftrightarrow{N}_{\mathrm{d}}(\vec{r},\vec{r}')\cdot\vec{M}(\vec{r}')$. For computing the more general field, $\vec{H}_{\mathrm{ms}}$, we can similarly rewrite Eq. (2.5) into the form

$$\vec{H}_{\mathrm{ms}}(\vec{r}) = \sum_{\vec{r}';\,\vec{r}'\neq\vec{r}} \overleftrightarrow{G}(\vec{r}-\vec{r}')\cdot\vec{M}(\vec{r}'), \tag{2.22}$$

where

$$\overleftrightarrow{G}(\vec{r}-\vec{r}') \equiv \begin{bmatrix} G^{xx}_{\vec{r}\vec{r}'} & G^{xy}_{\vec{r}\vec{r}'} & G^{xz}_{\vec{r}\vec{r}'} \\ G^{yx}_{\vec{r}\vec{r}'} & G^{yy}_{\vec{r}\vec{r}'} & G^{yz}_{\vec{r}\vec{r}'} \\ G^{zx}_{\vec{r}\vec{r}'} & G^{zy}_{\vec{r}\vec{r}'} & G^{zz}_{\vec{r}\vec{r}'} \end{bmatrix}. \tag{2.23}$$

The goal is to transform Eq. (2.22) into Fourier space, in which the discrete convolution of G and M will turn into a direct product, as shown in the following

$$\vec{H}_{\mathrm{ms}}(\vec{r}) = \sum_{\vec{r}';\, \vec{r}' \neq \vec{r}} \overleftrightarrow{G}(\vec{r} - \vec{r}') \cdot \vec{M}(\vec{r}') \xrightarrow{FFT} \vec{H}_{\mathrm{ms}}(\vec{k}) = \overleftrightarrow{G}(\vec{k}) \cdot \vec{M}(\vec{k}), \tag{2.24}$$

where $\vec{H}_{\mathrm{ms}}(\vec{k})$ will later be inverse Fourier transformed into $\vec{H}_{\mathrm{ms}}(\vec{r})$. Next I will show the explicit form of $\overleftrightarrow{G}(\vec{r} - \vec{r}')$. Assume a sample with dimensions $0 < x < L_x$, $0 < y < L_y$, and $-h/2 < z < h/2$, divided into $d \times d \times d$ cubic cells, as shown in Figure 2.1. Also we assume that the magnetization $\vec{M}$ is uniform within each cell. For each cell there are 6 surfaces with surface charges $\sigma_l(\vec{r}_l)$, $l = 1, 2, \ldots, 6$. Therefore Eq. (2.22) can be written as

$$\vec{H}_{\mathrm{ms}}(\vec{r}) = \sum_{l=1}^{6} \iint_{S_l} \frac{\vec{r} - \vec{r}_l'}{\left|\vec{r} - \vec{r}_l'\right|^3} \sigma_l\left(\vec{r}_l'\right)\, d^2 r_l', \tag{2.25}$$

where $\vec{r}_l'$ is the position vector for the surface l.

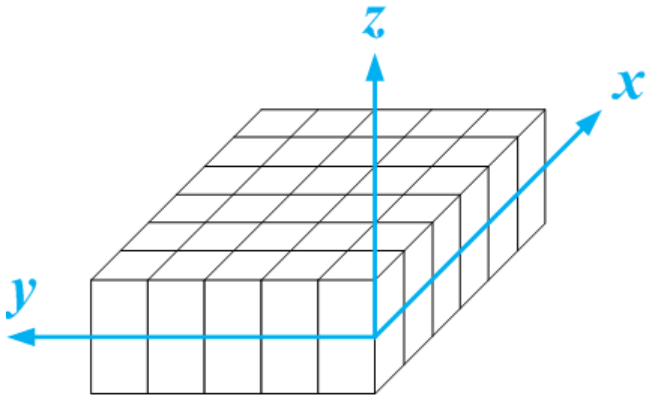

Figure 2.1: Schematic of the magnetic sample of rectangular shape for demagnetization field calculation.

Define $\vec{r} - \vec{r}' \equiv \vec{r} = (x, y, z)$ as the coordinates of the center of each cube. So the 9 entries in Eq. (2.23) are (see Appendix I for the detailed derivation)

$$\frac{G_{xx}(x,y,z)}{d^2 M_s} =$$

$$\left(\begin{array}{l}\left\{\tan^{-1}\left[\dfrac{\left(y-\frac{d}{2}\right)\left(z-\frac{d}{2}\right)}{\left(x-\frac{d}{2}\right)\sqrt{\left(x-\frac{d}{2}\right)^2+\left(y-\frac{d}{2}\right)^2+\left(z-\frac{d}{2}\right)^2}}\right]+\tan^{-1}\left[\dfrac{\left(y+\frac{d}{2}\right)\left(z+\frac{d}{2}\right)}{\left(x-\frac{d}{2}\right)\sqrt{\left(x-\frac{d}{2}\right)^2+\left(y+\frac{d}{2}\right)^2+\left(z+\frac{d}{2}\right)^2}}\right]\right\}- \\ \left\{\tan^{-1}\left[\dfrac{\left(y-\frac{d}{2}\right)\left(z+\frac{d}{2}\right)}{\left(x-\frac{d}{2}\right)\sqrt{\left(x-\frac{d}{2}\right)^2+\left(y-\frac{d}{2}\right)^2+\left(z+\frac{d}{2}\right)^2}}\right]+\tan^{-1}\left[\dfrac{\left(y+\frac{d}{2}\right)\left(z-\frac{d}{2}\right)}{\left(x-\frac{d}{2}\right)\sqrt{\left(x-\frac{d}{2}\right)^2+\left(y+\frac{d}{2}\right)^2+\left(z-\frac{d}{2}\right)^2}}\right]\right\}-\end{array}\right)$$

$$\left(\begin{array}{l}\left\{\tan^{-1}\left[\dfrac{\left(y-\frac{d}{2}\right)\left(z-\frac{d}{2}\right)}{\left(x+\frac{d}{2}\right)\sqrt{\left(x+\frac{d}{2}\right)^2+\left(y-\frac{d}{2}\right)^2+\left(z-\frac{d}{2}\right)^2}}\right]+\tan^{-1}\left[\dfrac{\left(y+\frac{d}{2}\right)\left(z+\frac{d}{2}\right)}{\left(x+\frac{d}{2}\right)\sqrt{\left(x+\frac{d}{2}\right)^2+\left(y+\frac{d}{2}\right)^2+\left(z+\frac{d}{2}\right)^2}}\right]\right\}- \\ \left\{\tan^{-1}\left[\dfrac{\left(y-\frac{d}{2}\right)\left(z+\frac{d}{2}\right)}{\left(x+\frac{d}{2}\right)\sqrt{\left(x+\frac{d}{2}\right)^2+\left(y-\frac{d}{2}\right)^2+\left(z+\frac{d}{2}\right)^2}}\right]+\tan^{-1}\left[\dfrac{\left(y+\frac{d}{2}\right)\left(z-\frac{d}{2}\right)}{\left(x+\frac{d}{2}\right)\sqrt{\left(x+\frac{d}{2}\right)^2+\left(y+\frac{d}{2}\right)^2+\left(z-\frac{d}{2}\right)^2}}\right]\right\}\end{array}\right)$$

(2.26)

$$\frac{G_{xy}(x,y,z)}{d^2 M_s} =$$

$$\left\{\ln\left\{\frac{4\left[-\left(z-\frac{d}{2}\right)+\sqrt{\left(x-\frac{d}{2}\right)^2+\left(y-\frac{d}{2}\right)^2+\left(z-\frac{d}{2}\right)^2}\right]}{\left[-\left(z+\frac{d}{2}\right)+\sqrt{\left(x+\frac{d}{2}\right)^2+\left(y-\frac{d}{2}\right)^2+\left(z+\frac{d}{2}\right)^2}\right]}\right\}-\ln\left\{\frac{4\left[-\left(z-\frac{d}{2}\right)+\sqrt{\left(x+\frac{d}{2}\right)^2+\left(y-\frac{d}{2}\right)^2+\left(z-\frac{d}{2}\right)^2}\right]}{\left[-\left(z+\frac{d}{2}\right)+\sqrt{\left(x-\frac{d}{2}\right)^2+\left(y-\frac{d}{2}\right)^2+\left(z+\frac{d}{2}\right)^2}\right]}\right\}\right\}-$$

$$\left\{\ln\left\{\frac{4\left[-\left(z-\frac{d}{2}\right)+\sqrt{\left(x-\frac{d}{2}\right)^2+\left(y+\frac{d}{2}\right)^2+\left(z-\frac{d}{2}\right)^2}\right]}{\left[-\left(z+\frac{d}{2}\right)+\sqrt{\left(x+\frac{d}{2}\right)^2+\left(y+\frac{d}{2}\right)^2+\left(z+\frac{d}{2}\right)^2}\right]}\right\}-\ln\left\{\frac{4\left[-\left(z-\frac{d}{2}\right)+\sqrt{\left(x+\frac{d}{2}\right)^2+\left(y+\frac{d}{2}\right)^2+\left(z-\frac{d}{2}\right)^2}\right]}{\left[-\left(z+\frac{d}{2}\right)+\sqrt{\left(x-\frac{d}{2}\right)^2+\left(y+\frac{d}{2}\right)^2+\left(z+\frac{d}{2}\right)^2}\right]}\right\}\right\}$$

(2.27)

$$\frac{G_{xz}(x,y,z)}{d^2 M_s} =$$

$$\left\{\ln\left\{\frac{4\left[-\left(y-\frac{d}{2}\right)+\sqrt{\left(x-\frac{d}{2}\right)^2+\left(y-\frac{d}{2}\right)^2+\left(z-\frac{d}{2}\right)^2}\right]}{\left[-\left(y+\frac{d}{2}\right)+\sqrt{\left(x+\frac{d}{2}\right)^2+\left(y+\frac{d}{2}\right)^2+\left(z-\frac{d}{2}\right)^2}\right]}\right\}-\ln\left\{\frac{4\left[-\left(y-\frac{d}{2}\right)+\sqrt{\left(x+\frac{d}{2}\right)^2+\left(y-\frac{d}{2}\right)^2+\left(z-\frac{d}{2}\right)^2}\right]}{\left[-\left(y+\frac{d}{2}\right)+\sqrt{\left(x-\frac{d}{2}\right)^2+\left(y+\frac{d}{2}\right)^2+\left(z-\frac{d}{2}\right)^2}\right]}\right\}\right\}-$$

$$\left\{\ln\left\{\frac{4\left[-\left(y-\frac{d}{2}\right)+\sqrt{\left(x-\frac{d}{2}\right)^2+\left(y-\frac{d}{2}\right)^2+\left(z+\frac{d}{2}\right)^2}\right]}{\left[-\left(y+\frac{d}{2}\right)+\sqrt{\left(x+\frac{d}{2}\right)^2+\left(y+\frac{d}{2}\right)^2+\left(z+\frac{d}{2}\right)^2}\right]}\right\}-\ln\left\{\frac{4\left[-\left(y-\frac{d}{2}\right)+\sqrt{\left(x+\frac{d}{2}\right)^2+\left(y-\frac{d}{2}\right)^2+\left(z+\frac{d}{2}\right)^2}\right]}{\left[-\left(y+\frac{d}{2}\right)+\sqrt{\left(x-\frac{d}{2}\right)^2+\left(y+\frac{d}{2}\right)^2+\left(z+\frac{d}{2}\right)^2}\right]}\right\}\right\}$$

(2.28)

$$\frac{G_{yx}(x,y,z)}{d^2 M_s} =$$

$$\left\{\ln\left\{\frac{4\left[-\left(z-\frac{d}{2}\right)+\sqrt{\left(x-\frac{d}{2}\right)^2+\left(y-\frac{d}{2}\right)^2+\left(z-\frac{d}{2}\right)^2}\right]}{\left[-\left(z+\frac{d}{2}\right)+\sqrt{\left(x-\frac{d}{2}\right)^2+\left(y+\frac{d}{2}\right)^2+\left(z+\frac{d}{2}\right)^2}\right]}\right\}-\ln\left\{\frac{4\left[-\left(z-\frac{d}{2}\right)+\sqrt{\left(x-\frac{d}{2}\right)^2+\left(y+\frac{d}{2}\right)^2+\left(z-\frac{d}{2}\right)^2}\right]}{\left[-\left(z+\frac{d}{2}\right)+\sqrt{\left(x-\frac{d}{2}\right)^2+\left(y-\frac{d}{2}\right)^2+\left(z+\frac{d}{2}\right)^2}\right]}\right\}-\right.$$

$$\left.\left\{\ln\left\{\frac{4\left[-\left(z-\frac{d}{2}\right)+\sqrt{\left(x+\frac{d}{2}\right)^2+\left(y-\frac{d}{2}\right)^2+\left(z-\frac{d}{2}\right)^2}\right]}{\left[-\left(z+\frac{d}{2}\right)+\sqrt{\left(x+\frac{d}{2}\right)^2+\left(y+\frac{d}{2}\right)^2+\left(z+\frac{d}{2}\right)^2}\right]}\right\}-\ln\left\{\frac{4\left[-\left(z-\frac{d}{2}\right)+\sqrt{\left(x+\frac{d}{2}\right)^2+\left(y+\frac{d}{2}\right)^2+\left(z-\frac{d}{2}\right)^2}\right]}{\left[-\left(z+\frac{d}{2}\right)+\sqrt{\left(x+\frac{d}{2}\right)^2+\left(y-\frac{d}{2}\right)^2+\left(z+\frac{d}{2}\right)^2}\right]}\right\}\right\}$$

(2.29)

$$\frac{G_{yy}(x,y,z)}{d^2 M_s} =$$

$$\left(\left\{\tan^{-1}\left[\frac{\left(x-\frac{d}{2}\right)\left(z-\frac{d}{2}\right)}{\left(y-\frac{d}{2}\right)\sqrt{\left(x-\frac{d}{2}\right)^2+\left(y-\frac{d}{2}\right)^2+\left(z-\frac{d}{2}\right)^2}}\right]+\tan^{-1}\left[\frac{\left(x+\frac{d}{2}\right)\left(z+\frac{d}{2}\right)}{\left(y-\frac{d}{2}\right)\sqrt{\left(x+\frac{d}{2}\right)^2+\left(y-\frac{d}{2}\right)^2+\left(z+\frac{d}{2}\right)^2}}\right]\right\}-\right.$$
$$\left.\left\{\tan^{-1}\left[\frac{\left(x-\frac{d}{2}\right)\left(z+\frac{d}{2}\right)}{\left(y-\frac{d}{2}\right)\sqrt{\left(x-\frac{d}{2}\right)^2+\left(y-\frac{d}{2}\right)^2+\left(z+\frac{d}{2}\right)^2}}\right]+\tan^{-1}\left[\frac{\left(x+\frac{d}{2}\right)\left(z-\frac{d}{2}\right)}{\left(y-\frac{d}{2}\right)\sqrt{\alpha\left(x+\frac{d}{2}\right)^2+\left(y-\frac{d}{2}\right)^2+\left(z-\frac{d}{2}\right)^2}}\right]\right\}\right)-$$
$$\left(\left\{\tan^{-1}\left[\frac{\left(x-\frac{d}{2}\right)\left(z-\frac{d}{2}\right)}{\left(y+\frac{d}{2}\right)\sqrt{\left(x-\frac{d}{2}\right)^2+\left(y+\frac{d}{2}\right)^2+\left(z-\frac{d}{2}\right)^2}}\right]+\tan^{-1}\left[\frac{\left(x+\frac{d}{2}\right)\left(z+\frac{d}{2}\right)}{\left(y+\frac{d}{2}\right)\sqrt{\left(x+\frac{d}{2}\right)^2+\left(y+\frac{d}{2}\right)^2+\left(z+\frac{d}{2}\right)^2}}\right]\right\}-\right.$$
$$\left.\left\{\tan^{-1}\left[\frac{\left(x-\frac{d}{2}\right)\left(z+\frac{d}{2}\right)}{\left(y+\frac{d}{2}\right)\sqrt{\left(x-\frac{d}{2}\right)^2+\left(y+\frac{d}{2}\right)^2+\left(z+\frac{d}{2}\right)^2}}\right]+\tan^{-1}\left[\frac{\left(x+\frac{d}{2}\right)\left(z-\frac{d}{2}\right)}{\left(y+\frac{d}{2}\right)\sqrt{\left(x+\frac{d}{2}\right)^2+\left(y+\frac{d}{2}\right)^2+\left(z-\frac{d}{2}\right)^2}}\right]\right\}\right) \tag{2.30}$$

$$\frac{G_{yz}(x,y,z)}{d^2 M_s} =$$

$$\left\{\ln\left\{\frac{4\left[-\left(x-\frac{d}{2}\right)+\sqrt{\left(x-\frac{d}{2}\right)^2+\left(y-\frac{d}{2}\right)^2+\left(z-\frac{d}{2}\right)^2}\right]}{\left[-\left(x+\frac{d}{2}\right)+\sqrt{\left(x+\frac{d}{2}\right)^2+\left(y+\frac{d}{2}\right)^2+\left(z-\frac{d}{2}\right)^2}\right]}\right\}-\ln\left\{\frac{4\left[-\left(x-\frac{d}{2}\right)+\sqrt{\left(x-\frac{d}{2}\right)^2+\left(y+\frac{d}{2}\right)^2+\left(z-\frac{d}{2}\right)^2}\right]}{\left[-\left(x+\frac{d}{2}\right)+\sqrt{\left(x+\frac{d}{2}\right)^2+\left(y-\frac{d}{2}\right)^2+\left(z-\frac{d}{2}\right)^2}\right]}\right\}\right\}-$$
$$\left\{\ln\left\{\frac{4\left[-\left(x-\frac{d}{2}\right)+\sqrt{\left(x-\frac{d}{2}\right)^2+\left(y-\frac{d}{2}\right)^2+\left(z+\frac{d}{2}\right)^2}\right]}{\left[-\left(x+\frac{d}{2}\right)+\sqrt{\left(x+\frac{d}{2}\right)^2+\left(y+\frac{d}{2}\right)^2+\left(z+\frac{d}{2}\right)^2}\right]}\right\}-\ln\left\{\frac{4\left[-\left(x-\frac{d}{2}\right)+\sqrt{\left(x-\frac{d}{2}\right)^2+\left(y+\frac{d}{2}\right)^2+\left(z+\frac{d}{2}\right)^2}\right]}{\left[-\left(x+\frac{d}{2}\right)+\sqrt{\left(x+\frac{d}{2}\right)^2+\left(y-\frac{d}{2}\right)^2+\left(z+\frac{d}{2}\right)^2}\right]}\right\}\right\} \tag{2.31}$$

$$\frac{G_{zx}(x,y,z)}{d^2 M_s} =$$

$$\left\{\ln\left\{\frac{4\left[-\left(y-\frac{d}{2}\right)+\sqrt{\left(x-\frac{d}{2}\right)^2+\left(y-\frac{d}{2}\right)^2+\left(z-\frac{d}{2}\right)^2}\right]}{\left[-\left(y+\frac{d}{2}\right)+\sqrt{\left(x-\frac{d}{2}\right)^2+\left(y+\frac{d}{2}\right)^2+\left(z+\frac{d}{2}\right)^2}\right]}\right\}-\ln\left\{\frac{4\left[-\left(y-\frac{d}{2}\right)+\sqrt{\left(x-\frac{d}{2}\right)^2+\left(y-\frac{d}{2}\right)^2+\left(z+\frac{d}{2}\right)^2}\right]}{\left[-\left(y+\frac{d}{2}\right)+\sqrt{\left(x-\frac{d}{2}\right)^2+\left(y+\frac{d}{2}\right)^2+\left(z-\frac{d}{2}\right)^2}\right]}\right\}\right\}-$$

$$\left\{\ln\left\{\frac{4\left[-\left(y-\frac{d}{2}\right)+\sqrt{\left(x+\frac{d}{2}\right)^2+\left(y-\frac{d}{2}\right)^2+\left(z-\frac{d}{2}\right)^2}\right]}{\left[-\left(y+\frac{d}{2}\right)+\sqrt{\left(x+\frac{d}{2}\right)^2+\left(y+\frac{d}{2}\right)^2+\left(z+\frac{d}{2}\right)^2}\right]}\right\}-\ln\left\{\frac{4\left[-\left(y-\frac{d}{2}\right)+\sqrt{\left(x+\frac{d}{2}\right)^2+\left(y-\frac{d}{2}\right)^2+\left(z+\frac{d}{2}\right)^2}\right]}{\left[-\left(y+\frac{d}{2}\right)+\sqrt{\left(x+\frac{d}{2}\right)^2+\left(y+\frac{d}{2}\right)^2+\left(z-\frac{d}{2}\right)^2}\right]}\right\}\right\}$$

(2.32)

$$\frac{G_{zy}(x,y,z)}{d^2 M_s} =$$

$$\left\{\ln\left\{\frac{4\left[-\left(x-\frac{d}{2}\right)+\sqrt{\left(x-\frac{d}{2}\right)^2+\left(y-\frac{d}{2}\right)^2+\left(z-\frac{d}{2}\right)^2}\right]}{\left[-\left(x+\frac{d}{2}\right)+\sqrt{\left(x+\frac{d}{2}\right)^2+\left(y-\frac{d}{2}\right)^2+\left(z+\frac{d}{2}\right)^2}\right]}\right\}-\ln\left\{\frac{4\left[-\left(x-\frac{d}{2}\right)+\sqrt{\left(x-\frac{d}{2}\right)^2+\left(y-\frac{d}{2}\right)^2+\left(z+\frac{d}{2}\right)^2}\right]}{\left[-\left(x+\frac{d}{2}\right)+\sqrt{\left(x+\frac{d}{2}\right)^2+\left(y-\frac{d}{2}\right)^2+\left(z-\frac{d}{2}\right)^2}\right]}\right\}\right\}-$$

$$\left\{\ln\left\{\frac{4\left[-\left(x-\frac{d}{2}\right)+\sqrt{\left(x-\frac{d}{2}\right)^2+\left(y+\frac{d}{2}\right)^2+\left(z-\frac{d}{2}\right)^2}\right]}{\left[-\left(x+\frac{d}{2}\right)+\sqrt{\left(x+\frac{d}{2}\right)^2+\left(y+\frac{d}{2}\right)^2+\left(z+\frac{d}{2}\right)^2}\right]}\right\}-\ln\left\{\frac{4\left[-\left(x-\frac{d}{2}\right)+\sqrt{\left(x-\frac{d}{2}\right)^2+\left(y+\frac{d}{2}\right)^2+\left(z+\frac{d}{2}\right)^2}\right]}{\left[-\left(x+\frac{d}{2}\right)+\sqrt{\left(x+\frac{d}{2}\right)^2+\left(y+\frac{d}{2}\right)^2+\left(z-\frac{d}{2}\right)^2}\right]}\right\}\right\}$$

(2.33)

$$\frac{G_{zz}(x,y,z)}{d^2 M_s} =$$

$$\left(\left\{\tan^{-1}\left[\frac{\left(x-\frac{d}{2}\right)\left(y-\frac{d}{2}\right)}{\left(z-\frac{d}{2}\right)\sqrt{\left(x-\frac{d}{2}\right)^2+\left(y-\frac{d}{2}\right)^2+\left(z-\frac{d}{2}\right)^2}}\right]+\tan^{-1}\left[\frac{\left(x+\frac{d}{2}\right)\left(y+\frac{d}{2}\right)}{\left(z-\frac{d}{2}\right)\sqrt{\left(x+\frac{d}{2}\right)^2+\left(y+\frac{d}{2}\right)^2+\left(z-\frac{d}{2}\right)^2}}\right]\right\}-\right.$$
$$\left.\left\{\tan^{-1}\left[\frac{\left(x-\frac{d}{2}\right)\left(y+\frac{d}{2}\right)}{\left(z-\frac{d}{2}\right)\sqrt{\left(x-\frac{d}{2}\right)^2+\left(y+\frac{d}{2}\right)^2+\left(z-\frac{d}{2}\right)^2}}\right]+\tan^{-1}\left[\frac{\left(x+\frac{d}{2}\right)\left(y-\frac{d}{2}\right)}{\left(z-\frac{d}{2}\right)\sqrt{\left(x+\frac{d}{2}\right)^2+\left(y-\frac{d}{2}\right)^2+\left(z-\frac{d}{2}\right)^2}}\right]\right\}\right)-$$
$$\left(\left\{\tan^{-1}\left[\frac{\left(x-\frac{d}{2}\right)\left(y-\frac{d}{2}\right)}{\left(z+\frac{d}{2}\right)\sqrt{\left(x-\frac{d}{2}\right)^2+\left(y-\frac{d}{2}\right)^2+\left(z+\frac{d}{2}\right)^2}}\right]+\tan^{-1}\left[\frac{\left(x+\frac{d}{2}\right)\left(y+\frac{d}{2}\right)}{\left(z+\frac{d}{2}\right)\sqrt{\left(x+\frac{d}{2}\right)^2+\left(y+\frac{d}{2}\right)^2+\left(z+\frac{d}{2}\right)^2}}\right]\right\}-\right.$$
$$\left.\left\{\tan^{-1}\left[\frac{\left(x-\frac{d}{2}\right)\left(y+\frac{d}{2}\right)}{\left(z+\frac{d}{2}\right)\sqrt{\left(x-\frac{d}{2}\right)^2+\left(y+\frac{d}{2}\right)^2+\left(z+\frac{d}{2}\right)^2}}\right]+\tan^{-1}\left[\frac{\left(x+\frac{d}{2}\right)\left(y-\frac{d}{2}\right)}{\left(z+\frac{d}{2}\right)\sqrt{\left(x+\frac{d}{2}\right)^2+\left(y-\frac{d}{2}\right)^2+\left(z+\frac{d}{2}\right)^2}}\right]\right\}\right) \quad (2.34)$$

CHAPTER 3. MAGNETIC ANISOTROPY AT FINITE TEMPERATURE

Magnetocrystalline anisotropy is one of the most important intrinsic properties of ferromagnets. Technologically, it is crucial for maintaining the stability of magnetically recorded grains. In recent years, ultrahigh density that means smaller grain volumes has increased interest in the binary alloy FePt with $L1_0$ phase that exhibits ultrahigh magnetocrystalline anisotropy (up to 7×10^7 erg/cm^3) with a relatively low Curie temperature T_c [61], [22]. It can be written using heat-assisted magnetic recording (HAMR) as described in Ch. 1, where the medium is usually heated to near T_c during the writing process [6]. In such a situation, the anisotropy will fluctuate strongly with time, which can have significant impacts on the writing process known as transition jitter [62]. Since the recording in HAMR happens on a sub-ns scale, the knowledge of the transient behavior of the anisotropy at high temperatures is therefore important. In 2010, P. Asseline *et al*. [63] proposed a general method based on torques exerted on magnetic moments for calculating the temperature-dependent anisotropy at thermal equilibrium. However, the anisotropy calculated through their method gives no information about the standard deviation of the anisotropy with time that is needed in an estimation of transition jitter. Here, a simple way is demonstrated to calculate the transient anisotropy at finite temperature.

3.1 Modeling Method

We used the coupled stochastic Landau-Lifshitz-Gilbert (LLG) equations [60], [64] where each sub-cell corresponds to a single atom. The coupled equations are solved numerically using the fourth-order Runge-Kutta method with a time step of 1 femtosecond. A grain of uniaxial anisotropy with its easy axis coinciding with the z-axis in Cartesian coordinates is assumed. The grain is placed in a bulk medium with periodic boundary conditions, so that there is no demagnetization field, i.e., no shape anisotropy.

Under the application of external field $\vec{H}^{appl}$, the total Hamiltonian ε which consists of the exchange, anisotropy, and Zeeman energy can be expressed as

$$\begin{aligned}\varepsilon &= \varepsilon^{exch} + \varepsilon^{ani} + \varepsilon^{Zeeman} \\ &= -\frac{A_{ex}}{d^2}\sum_{i\neq j}\hat{S}_i \cdot \hat{S}_j - K_u\sum_i\left(\hat{S}_i \cdot \hat{z}\right)^2 - M_s\sum_i \hat{S}_i \cdot \vec{H}^{appl}\end{aligned} \tag{3.1}$$

where $\vec{S}_i$ is the unit vector of the magnetic moment at atomic site i, A_{ex} is the atomistic exchange stiffness constant, M_s is the zero-temperature saturation magnetization, and K_u is the zero-temperature uniaxial anisotropy constant. The distance between atoms is d: it can also be viewed as the length of spatial discretization. The effective field for the stochastic LLG equation can be calculated by

$$\vec{H}_i^{eff} = -\frac{1}{M_s}\frac{\partial \varepsilon}{\partial \hat{S}_i} + \vec{H}_i^{th} \tag{3.2}$$

where $\vec{H}_i^{th}$ is the stochastic thermal field with $\langle H_{i,k}^{th}(t)\rangle = 0$ and $\langle H_{i,k}^{th}(t)H_{i',k'}^{th}(t')\rangle = \frac{2\alpha_i k_B T_i}{[(1+\alpha^2)\gamma M_s \Delta t \Delta x^3]} \times \delta_{kk'}\delta(i-i')\delta(t-t')$ following Brown's paper [60]. Δt and Δx are

the discretizations in time and space respectively. k indicates the Cartesian component along the x, y or z directions.

Microscopically, the total anisotropy torque, i.e., the torque resulting from the anisotropy energy, can be written as the sum of cross products of spin magnetizations and anisotropy fields over all spins

$$\left\|\vec{T}^{ani}\right\| = \left\|\sum_i \vec{T}_i^{ani}\right\| = \left\|M_s \sum_i \hat{S}_i \times \vec{H}_i^{ani}\right\| \tag{3.3}$$

where $\vec{H}_i^{ani}$ is the anisotropy field which can be extracted from Eq. (3.2). Furthermore, we can write the total anisotropy torque as sum of the two components that are parallel to and perpendicular to the hard plane. Macroscopically, the parallel anisotropy torque can be represented by the derivative of the Helmholtz free energy F with respect to the polar angle θ [63]

$$\left\|\vec{T}_{//}^{ani}\right\| = \frac{\partial F}{\partial \theta} \equiv \frac{\partial\left(K^{eff} \sin^2\theta\right)}{\partial \theta} = K^{eff} \sin 2\theta, \qquad 0 \le \theta < \frac{\pi}{2}. \tag{3.4}$$

Here it should be pointed out that the system is assumed to be at thermal equilibrium (viewed macroscopically), and, for computational ease, we restrict our grain magnetization to fluctuate "stably" in the upper hemisphere, i.e., no macroscopic switching occurs during the simulation (at least for 4 nS time period). This is the case when temperatures are not too close to T_c (< 700 K) without external field. In particular, the procedure is effective at the write temperature of about 675 K. Incidentally, the lower hemisphere yields the same results provided the absolute value of $\sin 2\theta$. We want to emphasize that θ is the

"macroscopic" polar angle which is analogous to the angle measured in torque-curve experiments. At first glance, the time-dependent $K^{eff}(t)$ can be obtained by directly taking the ratio of parallel torque to $\sin 2\theta(t)$. However, numerical instability may occur because here we apply no external field to the grain and thus θ will fluctuate around the z-axis, implying that $\sin 2\theta(t)$ will occasionally vanish. Instead, we make a scatter plot of torque versus $\sin 2\theta$, and fit the data with a least-squares regression line. The slope of the line is the desired proportionality constant $\langle K^{eff} \rangle$. Figure 3.1 shows, for instance, the scatter plots at 300 K and 650 K. The standard deviation of the effective anisotropy, δK^{eff}, can be defined as the standard deviation of the residuals divided by time-averaged $\sin 2\theta(t)$. Another important quantity, the anisotropy field H_K^{eff}, being directly related to the recording field, is also of considerable interest. Although there are multiple ways to define it [65], [66], the most meaningful definition of the anisotropy field for use in LLG-based micromagnetic simulations is

$$H_K^{eff}(t) = \frac{\left\| \frac{2K_u(T=0)}{M_S(T=0)} \sum_i \hat{S}_i \times \hat{S}_i \times \cos\theta_i \hat{z} \right\|}{\left\| \sum_i \hat{S}_i \times \hat{S}_i \times \hat{z} \right\| \left| \cos\theta \right|} . \tag{3.5}$$

In our simulation, a 6^3 nm^3 grain is divided into 8000 finite difference sub-cells of volume 0.3^3 nm^3 per cell to account for the inhomogeneity of the magnetizations at finite temperature. We take 0.005 to be the Gilbert damping constant on the atomic scale. The exchange stiffness constant A_{ex} of 1.1×10^{-6} erg/cm is used to produce the experimentally obtained T_c (~ 710 K). The atomic (also zero-temperature) saturated magnetization M_s and magnetic uniaxial anisotropy K_u are set to be 1100 emu/cm^3 and 7×10^7 erg/cm^3

respectively. Nearest-neighbor exchange and single-ion anisotropy are also assumed [67], [68]. All time-averaged quantities are calculated for 4 nS.

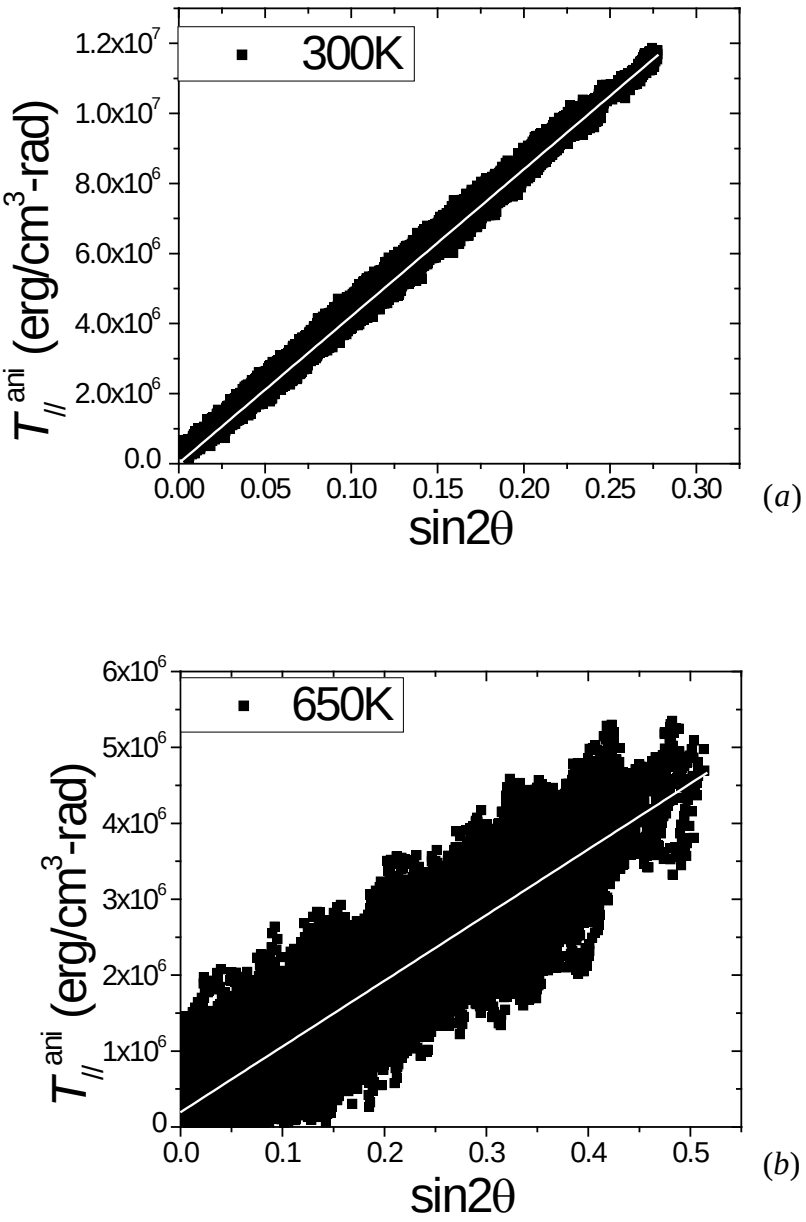

Figure 3.1: Scatter plot of in-plane anisotropy torque vs. sin2θ. The white straight line is the linear regression line.

3.2 Results

In Figure 3.2, we show the calculated time-averaged effective anisotropy versus temperatures. The almost linear relation with temperature agrees with previous theoretical results [63], [68], [69]. In Figure 3.3, we reproduce the Callen-Callen $M^3(T)$-dependence for coupled spins [68]. The deviation from this power-of-three dependence in the high-temperature range agrees with previous work and has been explained in the literature [63], [69].

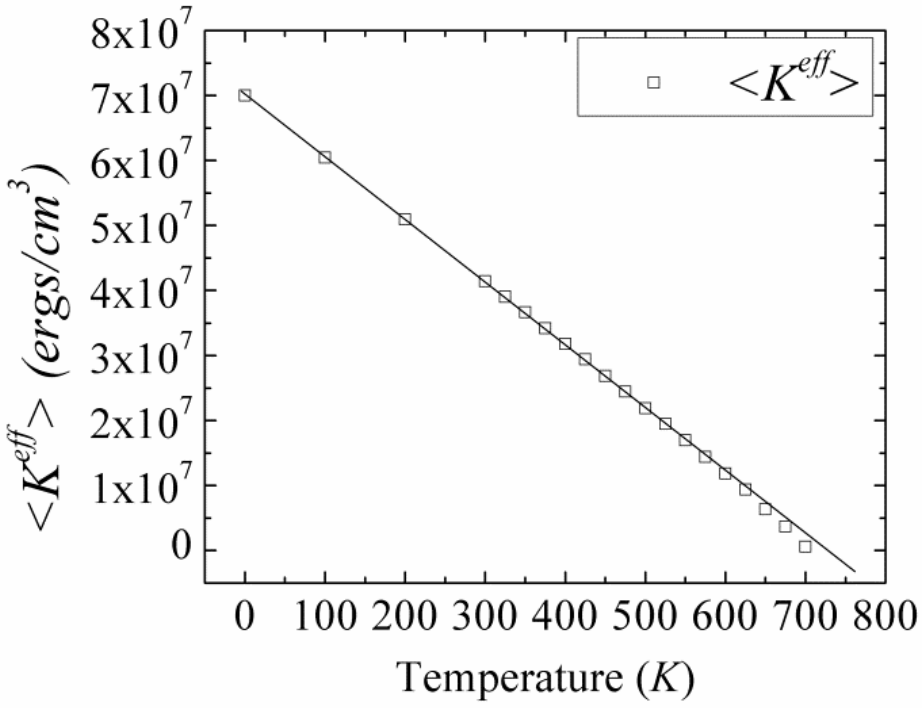

Figure 3.2: Simulation results for the temperature dependence of uniaxial anisotropy. The solid line is for eye guidance.

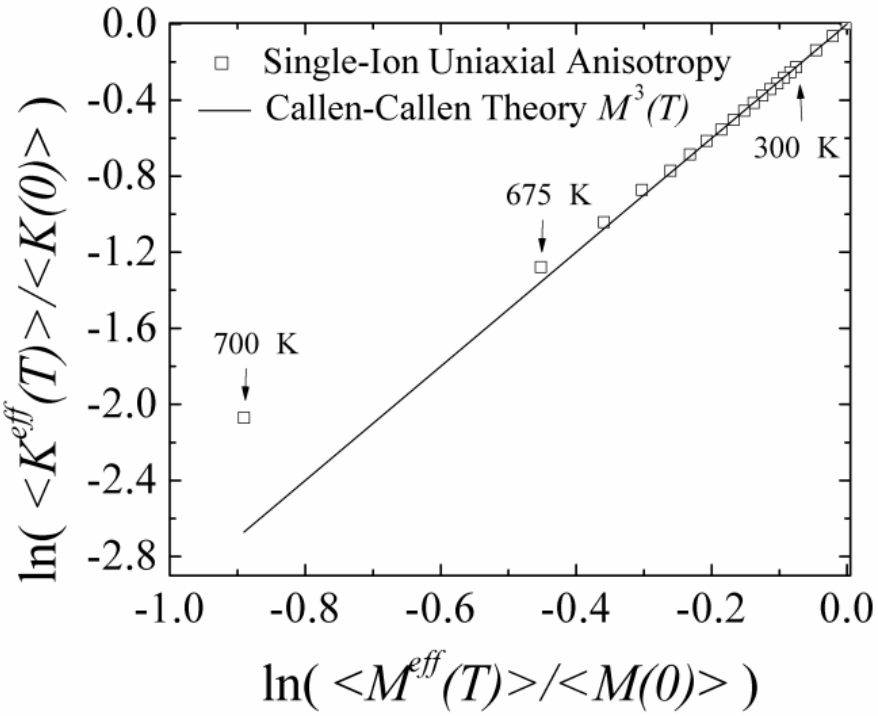

Figure 3.3: Comparison of predicted $\boldsymbol{K(T)}$-$\boldsymbol{M^{\rho}}$ between simulated results and Callen-Callen theory with $\boldsymbol{\rho = 3}$.

Figure 3.4 shows the anisotropy field up to 700 K, while fluctuations in anisotropy field and their ratio are only calculated up to 675 K because they diverge at 700 K. This latter quantity could be viewed as a switching field distribution and an indication of jitter. The large values at normal writing temperatures seem quite troubling. Concerns are partially alleviated by Figure 3.5 that shows the frequency dependence of the anisotropy at 650 K. Here $K^{eff}(t)$ is taken to be $\left\|\vec{T}_{\parallel}^{ani}(t)\right\|/\langle \sin 2\theta \rangle$, where the bracket in the denominator denotes time-averaging. It indicates that the envelope of the anisotropy amplitude decreases in an approximate $1/f$ trend starting from around 10 GHz. It suggests that about 60% of the fluctuation power occurs at frequencies too large to affect HAMR

recording. Nevertheless, the anisotropy fluctuations near T_c remain large when anisotropy fields are below about 25 kOe.

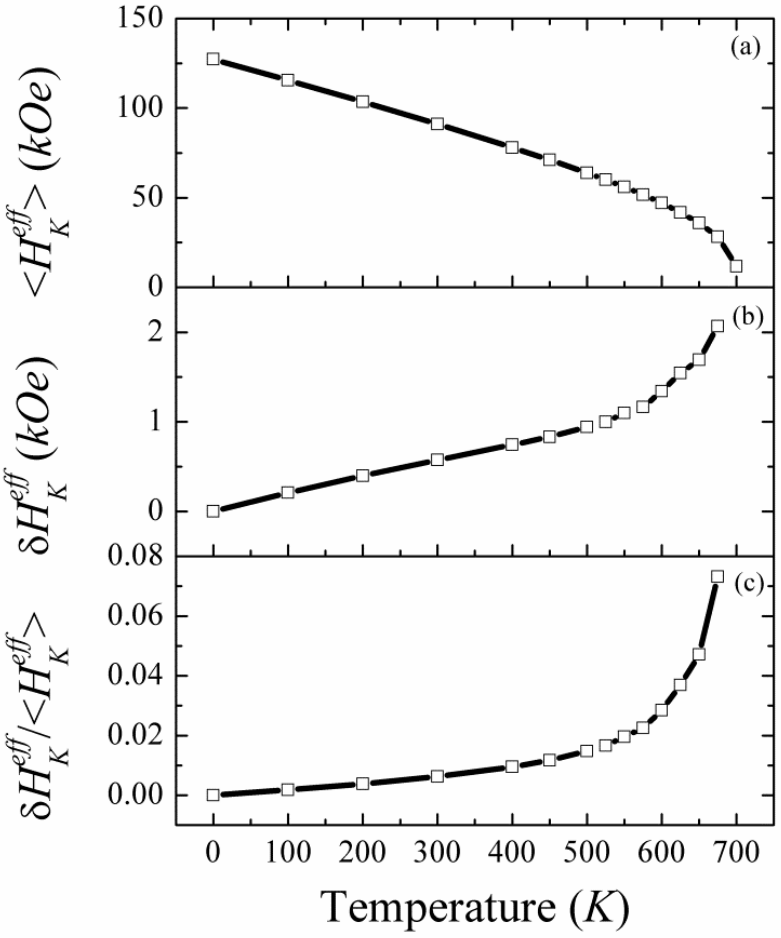

Figure 3.4: Temperature dependence of (a) anisotropy field, (b) field fluctuations and (c) their ratio.

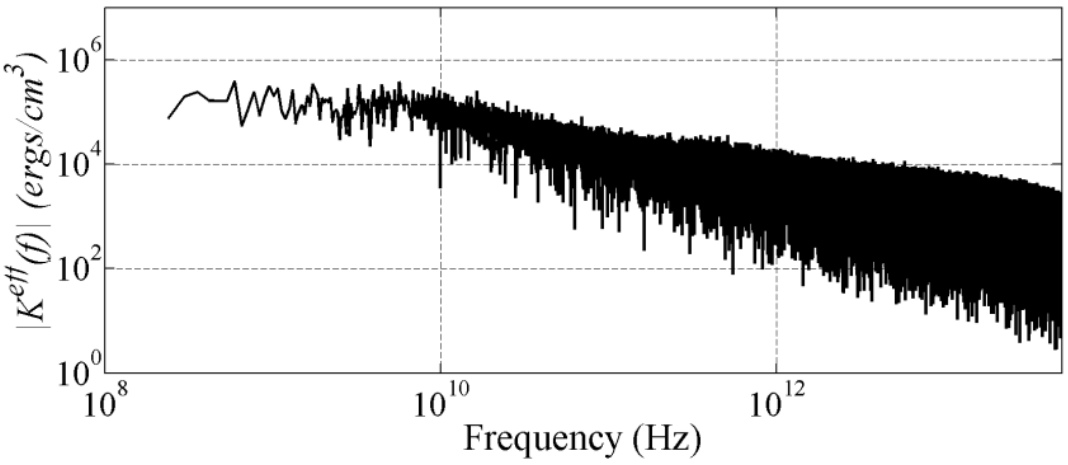

Figure 3.5: Single-sided amplitude spectrum of a time-domain anisotropy at T = 650 K.

The finite size effect of the anisotropy and its fluctuation at 650 K are shown in Figure 3.6. It can be seen that the magnitude of anisotropy is quite independent of grain size at constant temperature, while fluctuations decrease with increasing grain size. The fitting curve differs from $L^{-1.5}$ (not shown in the figure) because of the strong correlation between spins even at high temperatures, where L is the length scale of the grain. It can be seen that the effect of fluctuating anisotropy will worsen at the small grain sizes likely for HAMR.

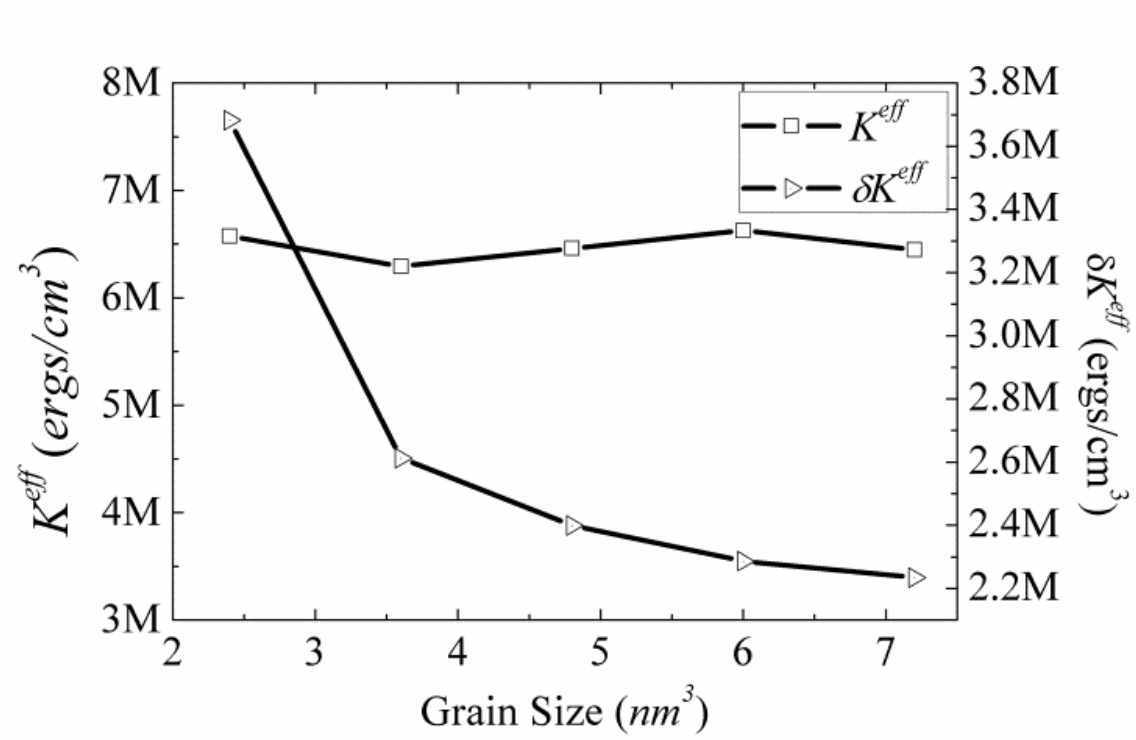

Figure 3.6: Finite size effect of the anisotropy and its fluctuations at T = 650 K.

Figure 3.5 suggests that thermally induced fluctuations of the anisotropy field would result in a large transition jitter for information written at temperature T_{write} close to T_{c}. It suggests that a larger difference between T_{write} and T_{c} will reduce fluctuations. Here, we propose the use of a composite structure, consisting of a hard layer and a high T_{c} soft layer, to accomplish this goal.

The composite grain under study consists of an FePt hard layer and a soft layer loosely modeled on Fe as shown in Figure 3.7. We assume a 3 nm thickness for each layer and 6^2 nm^2 for the lateral dimensions. The magnetic parameters of FePt are the same as those used in the previous discussion. For the soft layer, the anisotropy is taken to be zero, the magnetization M_s is 1700 emu/cm^3, and an exchange parameter of 1.6×10^{-6} ergs/cm is

used to produce a T_c of about 1000 K. Perfect interface exchange coupling is assumed with the stiffness constant being the geometric mean of the bulk values of bottom and top layers. For comparative purposes, we generate a homogeneous grain having the same physical dimensions as the composite one. Average magnetization $M_s^{\mathrm{Homo}} = (M_s^{\mathrm{FePt}} \times t^{\mathrm{FePt}} + M_s^{\mathrm{Soft}} \times t^{\mathrm{Soft}})/(t^{\mathrm{FePt}} + t^{\mathrm{Soft}})$ and anisotropy constant $K_u^{\mathrm{Homo}} = (K_u^{\mathrm{FePt}} \times t^{\mathrm{FePt}} + K_u^{\mathrm{Soft}} \times t^{\mathrm{Soft}})/(t^{\mathrm{FePt}} + t^{\mathrm{Soft}})$ are used as the magnetic parameters of the homogeneous grain so that it has the same energy barrier and therefore thermal stability as the composite counterpart. The exchange stiffness constant of the homogeneous grain is required to be 1.05×10^{-6} erg/cm so that both materials write at the same temperature.

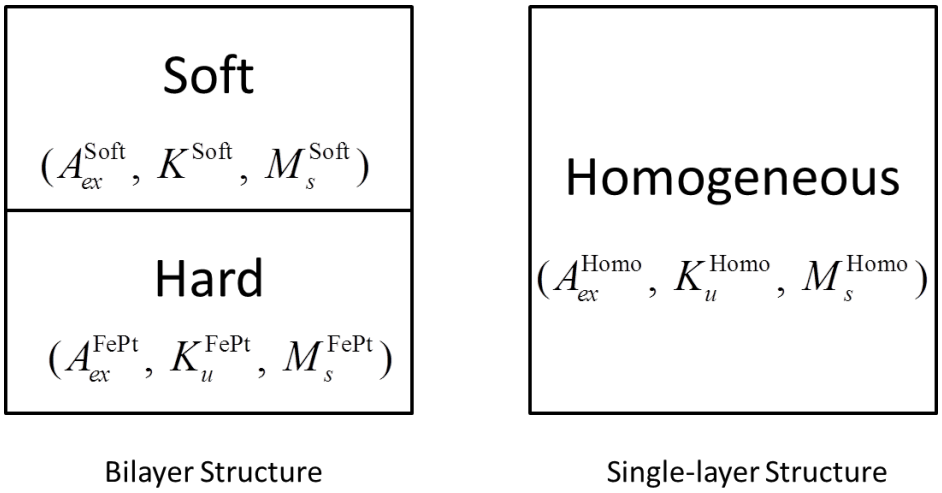

Figure 3.7: Schematic diagrams of composite and homogeneous materials.

We find that the normalized standard deviation of anisotropy constants $\delta K_u^{eff}/\langle K_u^{eff}\rangle$ of the composite grain is lower than that of the homogeneous grain by 13% at the write temperature of 600 K. This appears to be a direct consequence of the increased distance

between T_{write} and T_c^{hard} for the composite grain (110 K) versus the homogeneous grain distance (80 K). We expect that the anisotropy fluctuations could be further decreased with more judicious choice of materials and volume ratios. This optimization should be performed under realistic cooling conditions, rather than the thermal equilibrium assumed throughout this paper. It is also worth noting that the composite structure has the further advantage of reducing the write temperature (relative to pure FePt) without doping the FePt. This may alleviate lubricant degradation and thermal stress.

3.3 Conclusion

In this chapter, a simple method is proposed to calculate the temperature-dependent anisotropy and its transient behavior. Under the assumption of single-ion material, the standard deviation and frequency response of uniaxial bulk anisotropy is obtained, and therefore the transition jitter can be estimated. Use of a composite structure reduces the variance of anisotropy in time and thus may reduce jitter.

CHAPTER 4. SIMULATION OF HAMR USING RENROMALIZED CELLS

In Ch. 1, it is mentioned that commercial perpendicular magnetic recording using Co-based media currently reaches an areal density of about 750 Gb/in^2, and is predicted to reach a maximum density of 1 Tb/in^2 in the future. Beyond that, Heat-Assisted Magnetic Recording (HAMR) is believed to offer the best potential. Although HAMR has already been demonstrated [70], there remains much interest in its ultimate limits. Several previous studies have shown potential limits on HAMR [37], [71], [72], especially indetermination of switching times and thermal instability (superparamagnetic effect) as temperature increases to the Curie temperature T_c, in addition to other issues [6]. These could be clarified by reliable recording simulations. Previously, several Landau-Lifshitz-Gilbert (LLG)-based micromagnetic models have been proposed to model the HAMR process [71], [73]. However, most of these models are based on assumptions that are too simplified to accurately mimic the dynamics of grains with diameters of several nanometers, especially at temperatures close to T_c. This leads to the need for atomic scale (several angstroms) modeling to resolve domain walls or high frequency spin waves within a grain. However, with limited computational resources, it is impractical to perform recording simulations on the atomic scale that include magnetostatic interactions. Fortunately, from renormalization group theory we know that an atomistic multi-spin system, with exchange interactions among spins, can be replaced by larger spin blocks, meaning that each block contains multiple atomic spins (coarse-graining) [74]. This is enabled by the knowledge

that the correlation length of spin fluctuations becomes quite long near T_c, eventually reaching infinity at T_c. Since the recording process in HAMR occurs at high temperatures close to T_c, coarse-graining in HAMR should be helpful.

4.1 Modeling Method

Figure 4.1 illustrates our strategy for realizing HAMR simulations that include magnetostatic interactions together with fluctuations of properties such as energy and magnetization. As shown, we calculate the magnetic properties of a large number, typically a 6^3 nm^3 cube, of atomic spins with periodic boundary conditions. The atomic spins are described by material parameters that represent atomic properties in the absence of thermal fluctuations. These atomic spins are then aggregated into blocks of spins. Each block spin is described by renormalized material parameters that produce the same macroscopic magnetic properties as the atomistic description. These block spins are then used to form the irregular-shaped grains of recording media.

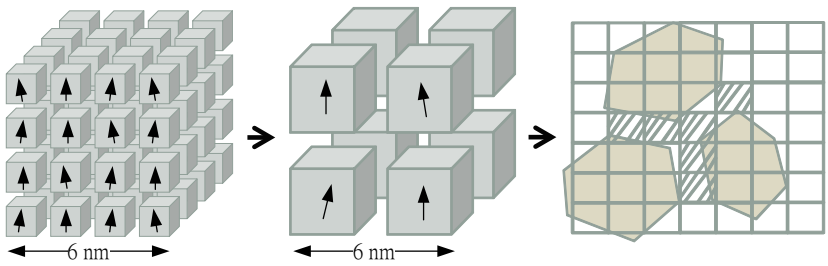

Figure 4.1: Schematic for the simulation of HAMR. The atomic spins are coarse-grained into renormalized block spins that are used for the elements of a 3-D grid mapped into Voronoi medium grains.

A. Finding the Renormalized Material Parameters

We use the stochastic coupled LLG equations to describe the motions of spins (either individually or in their aggregated form) as shown in the following

$$\frac{d\vec{M}_i}{dt} = \frac{-\gamma}{1+\alpha_i^2}\vec{M}_i \times \vec{H}_i^{\text{eff}} - \frac{\gamma\alpha_i}{(1+\alpha_i^2)M_i}\vec{M}_i \times \vec{M}_i \times \vec{H}_i^{\text{eff}} \ . \tag{4.1}$$

In Eq. (4.1), we write all parameters and variables in the most general fashion: they are all location-dependent, denoted by a subscript i, since in HAMR the temperature T is not spatially constant. Therefore, $\vec{M}_i$ is the magnetization vector of spin i with conservation of magnitude and $\vec{H}_i^{\text{eff}}$ is the effective field exerted on that spin. γ is the gyromagnetic ratio 1.76×10^7 ($\text{Oe}^{-1}\text{s}^{-1}$) and α_i is the dimensionless Gilbert damping parameter. The effective field can be calculated by taking a functional derivative of the Hamiltonian ε of the magnetic system with respect to $\vec{M}_i$ as in Eq. (3.2).

Using the 3-dimensional Heisenberg spin model, ε is of the form

$$\frac{\varepsilon}{\Delta x^3} = -\frac{A_{ij}}{\Delta x^2}\sum_i^N \sum_{j\in\text{n.n.}} \frac{\vec{M}_i \cdot \vec{M}_j}{M_i M_j} - K_i \sum_i^N \left(\frac{\vec{M}_i}{M_i}\cdot \hat{z}\right)^2 - \sum_i^N \vec{M}_i \cdot \vec{H}_i^{\text{Zeeman}} \tag{4.2}$$

which includes exchange interaction, uniaxial anisotropy, and Zeeman energy. A_{ij} (> 0) is the ferromagnetic exchange stiffness between spins i and j, and K_i the anisotropy at spin i. Δx denotes the length scale of the discretized cell and N is the total number of cells (spins). $\vec{H}_i^{\text{Zeeman}}$ is the Zeeman field on spin i, which can be combination of applied fields and magnetostatic fields. A nearest-neighbor approximation for exchange interaction is assumed. In Eq. (4.1) and (4.2), the input material parameters, M_i, K_i, A_i and α_i, are functions of Δx and T_i. We add one more subscript to these parameters to denote the

parameters on different length scales. For example, $M_{i,\mathrm{atom}}$ indicates the saturation magnetization on atomic scale ($\Delta x = a$), and $M_{i,\mathrm{block}}$ on renormalized scale ($\Delta x = na$), where a is set to be 0.3 nm denoting the interatomic spacing and n can be any integer larger than 1.

For an atomistic LLG simulation ($\Delta x = a$) of a 6^3 nm^3 cubic grain of FePt in the $L1_0$ phase, the cube is discretized into 20×20×20 cells and modeled at different temperatures. The input material parameters used here are intrinsic and independent of T_i. Using our previously developed method [75], we can calculate the spontaneous magnetization $\langle M \rangle_0$, anisotropy field $\langle H_\mathrm{K} \rangle_0$ and its standard deviation δH_K in thermal equilibrium (denoted by $\langle \dots \rangle_0$). The input material parameters, Δt and integration time are the same as in [75], which are $M_\mathrm{s} = 1100$ emu/cm^3, $K_\mathrm{u} = 7 \times 10^7$ ergs/cm^3, $A_\mathrm{ex} = 1.1 \times 10^{-6}$ ergs/cm, $\Delta t = 1$ fS, and 4 nS. The plot of anisotropy field versus magnetization is shown in Figure 4.2, in which we can see a linear dependence near T_c. In this atomistic system, the magnetization is resolved down to microscopic scale, and therefore all high frequency spin waves can exist and explain essentially any dynamics of the system. If we use the larger block spins to describe the system, then we have effectively integrated over the highest frequency spin waves. Therefore, a block spin should have average magnetic properties coming from the averages of encompassed atomic spins. The “average” here means taking statistical average over space and time.

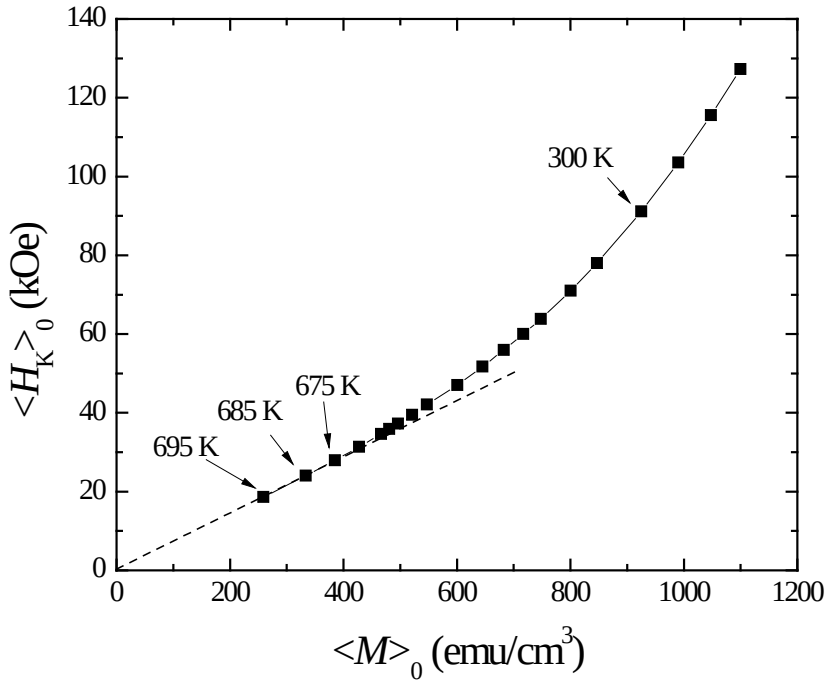

Figure 4.2: Linear relationship between $\langle \boldsymbol{H_K} \rangle_{\boldsymbol{0}}$ and $\langle \boldsymbol{M} \rangle_{\boldsymbol{0}}$ near $\boldsymbol{T_c}$ of a 6^3 nm^3 FePt cubic grain.

We start with finding the renormalized damping constant. Following Feng and Visscher's method [76], α_{block} can be calculated as shown in Eq. (4.3)

$$\frac{\alpha_{\text{block}}}{1+\alpha_{\text{block}}{}^2} = \frac{-M_{i,\text{atom}} \left\langle \sum_i^{\text{agg}} \frac{d\vec{M}_{i,\text{atom}}}{dt} \cdot \vec{M}_{i,\text{atom}} \times \vec{M}_{i,\text{atom}} \times \vec{H}_i^{\text{eff}} \right\rangle_t}{\gamma \left\langle \sum_i^{\text{agg}} \left(\vec{M}_{i,\text{atom}} \times \vec{M}_{i,\text{atom}} \times \vec{H}_i^{\text{eff}} \right)^2 \right\rangle_t} \tag{4.3}$$

where "agg" specifies aggregation of multiple atomic spins into one block spin, and $\langle \ldots \rangle_t$ denotes the time-average. Figure 4.3a shows the calculated results of renormalized damping constant at different temperatures and block sizes. The dashed line in Figure 4.3a indicates the atomic damping constant which is in general small and chosen to be 0.005 in

this paper. “d” in the legend of Figure 4.3a denotes the edge length of the block spin, which is the multiple of atomistic length (0.3 nm) described by the labeled “agg.”

With α_{block} determined, we proceed to find M_{block}, K_{block}, and A_{block}. Arguing that macroscopic magnetic properties calculated on the renormalized scale should be maximally equivalent to those on the atomic scale, we construct a system of three simultaneous equations with three unknown variables by equating $\langle M \rangle_0$, $\langle H_{\text{K}} \rangle_0$ and δH_{K} on both scales:

$$\left\langle M^{\text{atom}} \right\rangle_0 = \left\langle M^{\text{block}} \left(M_{\text{block}}, K_{\text{block}}, A_{\text{block}} \right) \right\rangle_0 \tag{4.4}$$

$$\left\langle H_K^{\text{atom}} \right\rangle_0 = \left\langle H_K^{\text{block}} \left(M_{\text{block}}, K_{\text{block}}, A_{\text{block}} \right) \right\rangle_0 \tag{4.5}$$

$$\delta H_K^{\text{atom}} = \delta H_K^{\text{block}} \left(M_{\text{block}}, K_{\text{block}}, A_{\text{block}} \right) \tag{4.6}$$

Eq. (4.4)-(4.6) are, in general, nonlinear, and can be solved by a trial-and-error numerical procedure: they are required to reach equality to within 5%. We constrain the system to renormalized magnetization, anisotropy and exchange between the atomic and bulk values. Within this constraint, the solution appears to be unique. The obtained renormalized parameters are shown in Figure 4b-4d. The bulk values in Figure 4b and 4c are the predicted macroscopic spontaneous magnetization and anisotropy from atomistic LLG simulation.

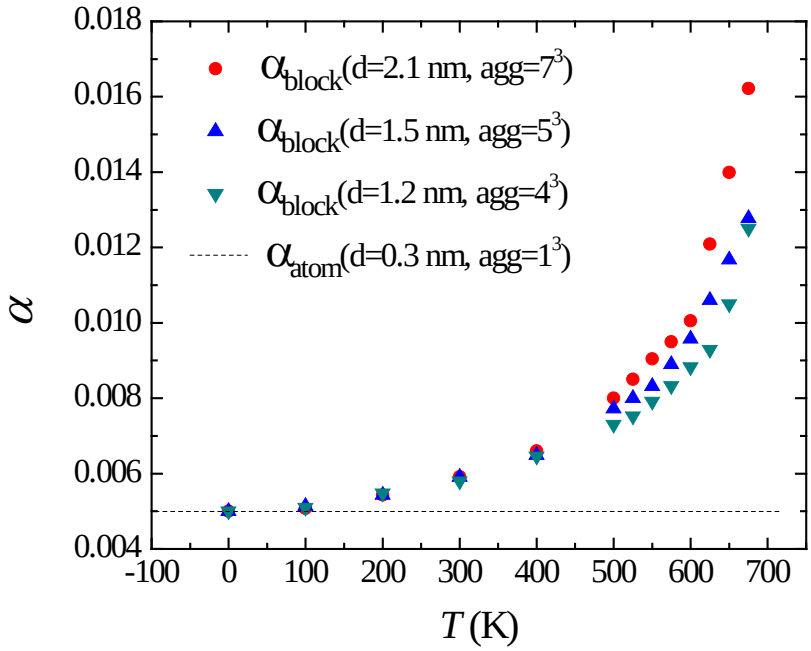

(*a*)

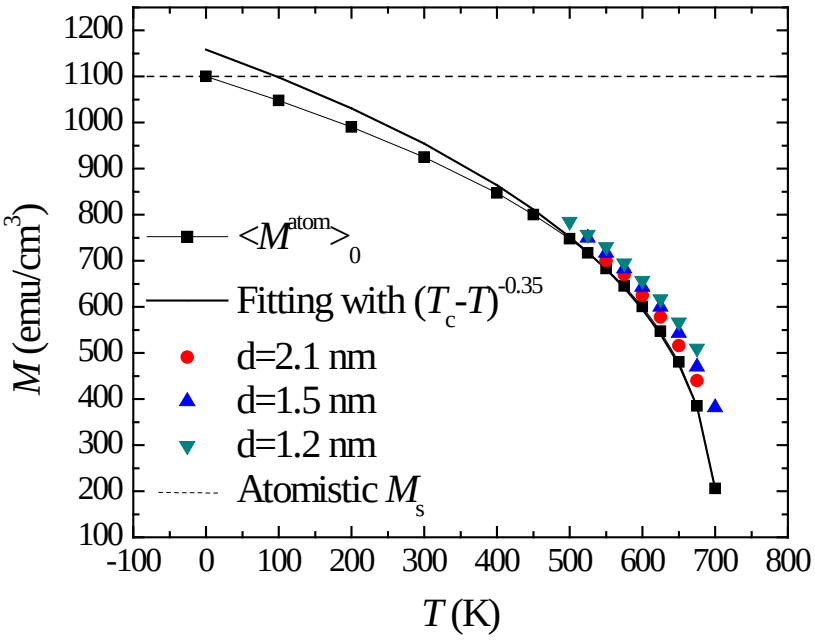

(*b*)

Figure 4.3: Renormalized Parameters as functions of temperature and length scale. (a) Gilbert damping parameter; d represents different length scales; "agg" is equal to the number of atomic spins in aggregation. (b) Saturation magnetization.

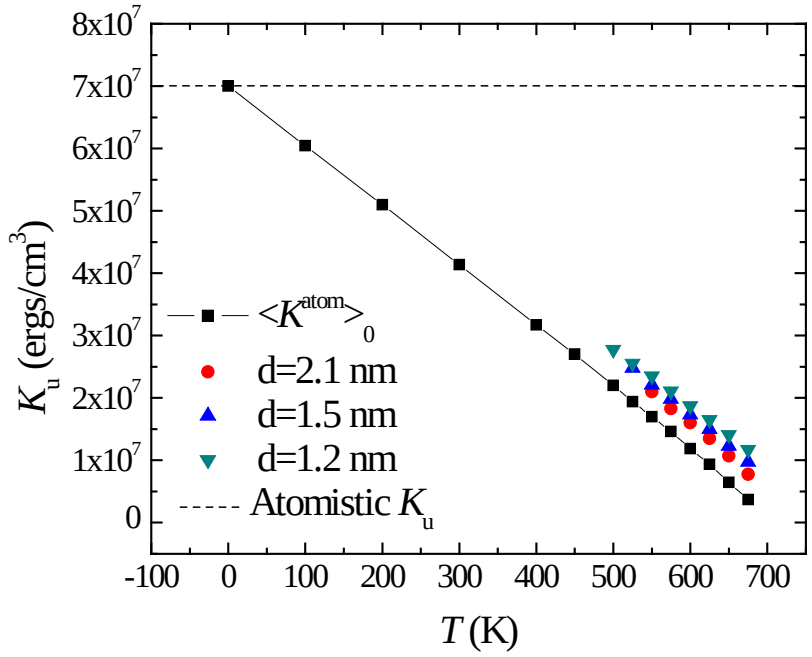

(*c*)

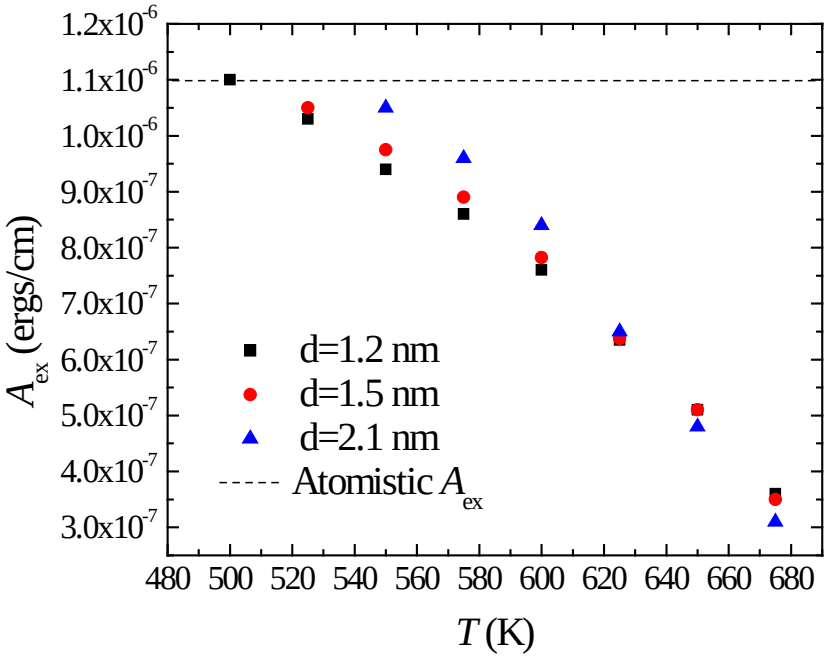

(*d*)

Figure 4.3: Renormalized Parameters as functions of temperature and length scale. (c) Anisotropy constant. (d) Exchange stiffness parameter.

B. Discussion of Renormalization Parameters

1) Gilbert Damping Parameter: In the LLG equation the phenomenological damping parameter represents all the relaxation mechanisms of magnetization, and is responsible for the rate at which spins come to equilibrium. It can be seen that damping increases with block size: this occurs because progressively more spin waves contribute to the parameter α consisting of both intrinsic, extrinsic, and magnon scattering contributions [77], [78]. The number of magnons available for scattering increases with temperature: this makes the damping parameter α more sensitive to length scale at the higher temperatures. This effect can be seen in Figure 3a, where the renormalized damping parameters on different scales converge to the atomic damping constant as T goes to zero.

2) Magnetization and Anisotropy: In Figure 3b, the macroscopic spontaneous magnetization at temperatures close to T_c can be fitted by a power law $M \sim (T_c - T)^{\beta}$ with $\beta = 0.35(\pm 0.02)$ and $T_c = 705$ K. The exponent β here is near the well-known critical exponent beta (~1/3 in literature). The renormalized saturation magnetizations and anisotropies on different scales are also shown in Figure 4.3b and 4.3c. We can see that the renormalized input parameters (M_{block} and K_{block}) get asymptotically closer to the macroscopic values with increasing length scales. This can be understood by considering the limiting case, in which a single block spin represents the entire grain and therefore possesses intrinsic magnetization and anisotropy equal to macroscopic values.

3) Exchange Stiffness: The naive expectation is that the exchange parameter should be proportional to the square of the magnetization, implying that larger spin blocks should have less exchange than smaller spin blocks that should in turn be less than atomic values.

Figure 4.3d shows this result at high temperatures. This argument should only be valid if the spin correlation length remains constant with temperature. The theory of critical phenomena predicts that correlation length peaks sharply at the Curie temperature and rapidly declines for lower temperatures. We speculate that this decline accounts for the crossover observed in Figure 4.3d at about 635 K, i.e. 70 K below T_c.

C. Switching Behavior

In order to justify the renormalized parameters that have been found, we compare the switching times of a 6^3 nm^3 grain at 675 K on three length scales: 2.1 nm, 1.5 nm and 0.3 nm. To calculate the switching times, the spins of a grain are initially aligned near the direction of the easy axis ($\theta = 0.5°$) with an applied field pointing in the opposite direction ($\theta = 180°$). The magnetostatic interaction fields are ignored. Every time the grain magnetization switches ($\theta > 135°$), the system is reset. The mean switching time t_{sw} is then obtained by repeating this simulation 1000 times for each renormalized data point and 100 times for each atomistic point. However, the atomistic values at 20 and 22 kOe had excessive standard deviations: apparently, 100 simulations are insufficient. For these two cases, we instead fitted the t_{sw} with the expected log normal function $lnN(\mu, \sigma^2)$ and obtain estimated μ and standard deviation σ. The results for all fields are shown in Figure 4.4. We can see that switching times calculated for all three length scales have a very similar trend with increased applied field.

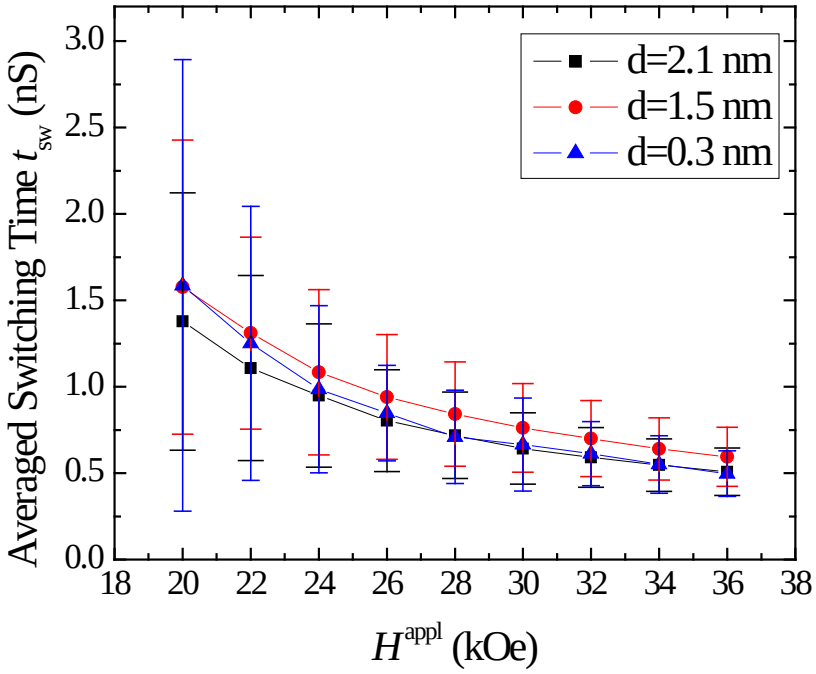

Figure 4.4: Average switching times of a 6^3 nm^3 FePt cubic grain as functions of applied field at different length scales.

4.2 Magnetic Recording

In this section, we describe the HAMR simulations based on the parameters found in the previous section. A 6-nm thick recording medium with in-plane (*x*-*y*) dimensions of 384×48 nm^2 is modeled by 600 Voronoi grains packed in the plane with cut-off boundary conditions, as illustrated in Figure 4.5a. An isolated track is then written along the long *x*-direction (down track). The grains are assumed to be uniform in shape from top to bottom, and have their easy axes all coinciding with the *z*-axis. The average and standard deviation of the grain diameters (excluding grain boundaries) are 5.47 nm and 1.57 nm respectively. The nonmagnetic grain boundaries are assumed to be constant with 1 nm thickness. To

make use of the block spins obtained from the previous section, the Voronoi-cell-based layer is mapped onto a 3-dimensional grid where each cubic grid-cell represents one block spin. Here we choose the block size of 1.5^3 nm^3 as a good compromise between computational time and spatial resolution.

In HAMR, a laser source is incorporated in and moves together with the write head, and heat energy is delivered to the recording layer through a near-field transducer [6]. We assume that the in-plane thermal conductivity of the recording layer is much less than the cross-plane and that there is a perfect heat sink at the bottom of the layer. Therefore the thermal profile on the recording layer can be modeled by a 2-dimensional Gaussian distribution in the *xy*-plane with Full-width Half-Maximum (*FWHM*) as small as 40 nm. We assume uniformity in the *z*-direction. Since the regions distant to the thermal spot are at room temperature of 300 K, the overall in-plane temperature distribution on the layer can be written as $T(x,y,t) = 300 + (T_{\max} - 300)\exp[(-(x-vt)^2 - (y-W_0)^2)/2\sigma^2]$, where $\sigma = FWHM/\left(2\sqrt{2ln2}\right)$, W_0 denotes the track center, $T_{\max}$ is the maximum temperature at the spot center, v is the head velocity (m/s) and t is the elapsed time (s). Assuming that the recording is dominated by the thermal gradient [79], we model the worst case where the head field is uniform throughout the recording layer when writing transitions. The head field reverses its direction instantaneously when writing a transition. Using the above specifications, we vary the following conditions to compare HAMR performance: $T_{\max}$ (K), v (m/s), canting angle θ of the head field with respect to z-axis, and head field strength H^{appl} (kOe).

During the writing process, each block spin i in the medium is governed by the LLG equation with renormalized parameters M_{block}, K_{block}, A_{block} and α_{block}. A_{block} describing the exchange interaction between block spin i and j is obtained by taking the average of $A_{i,\text{block}}$ and $A_{j,\text{block}}$. For 1.5^3 nm^3 block spins, except for α_{block}, the three other renormalized parameters are only found in the temperature range of [525 K, 695 K], and fitted in [525 K, 700 K] (Figure 4.3). For an average-sized grain of volume 6.0×5.5^2 nm^3 at 525 K, $2\langle K_u\rangle/\langle M\rangle$ and $\langle K_u\rangle V/k_BT$ from our atomistic simulation are about 55 kOe and 49 respectively. This implies that the cold grain will never switch by write head field or random thermal field (superparamagnetic effect) during our simulation time. The grains at temperatures above 700 K have no importance in our simulation because both their magnetizations and anisotropies largely vanish. Therefore, we have good reason to establish a rule for separating the renormalized parameters into three categories, at temperatures below 525 K, in between 525 K and 700 K, and above 700 K. As shown in Table 4.1, the parameters below 525 K are assigned a constant value 0.0075 for α_{block}, $A_{\text{ex}}(\langle M\rangle/M_{\text{s}})^2$ for A_{block}, and values from bulk atomistic predictions for the others. $\langle M\rangle$ stands for the bulk atomistic prediction of magnetization of a 6^3 nm^3 grain. In between 525 K and 700 K, the parameters are obtained by fitting the data in Figure 4.2. Above 700 K, α_{block} is set to be 0.1, M_{block} is 30 emu/cm^3, K_{block} and A_{block} are 0. The nonzero value of M_{block} is for numerical stability. For the case where neighboring blocks belong to different grains, we employ an intergranular exchange coupling A_{block}(inter) of either zero or 15% of bulk exchange, a value that we find to be optimal.

T (K)	α_{block}	M_{block} (emu/cm^3)	K_{block} (erg/cm^3)	A_{block} (erg/cm)
$T < 525$	0.0075	Atomistic prediction	Atomistic prediction	$A_{\text{ex}}(\langle M\rangle/M_{\text{s}})^2$
$525 \le T < 700$	Fitted	Fitted	Fitted	Fitted
$T \ge 700$	0.1	30	0	0

Table 4.1: Temperature categories and corresponding fitting rules of the renormalized material parameters.

In the simulation, the calculation of magnetostatic fields $\vec{H}^{\text{ms}}$ costs the most computing time. To increase computational efficiency, we use an FFT-based approach where the fields in real space are expressed using the following relation,

$$\vec{H}_i^{\text{ms}} = \sum_{j\neq i}^{N}\sum_{l=1}^{6}\iint_S \frac{\vec{r}_i - \vec{r}_{j,l}}{\left|\vec{r}_i - \vec{r}_{j,l}\right|^3}\vec{M}_j \cdot \hat{n}_l d^2 r_{j,l} \tag{4.7}$$

In Eq. (4.7), $\vec{r}_i$ and $\vec{r}_{j,l}$ are the coordinate vectors of the center of cell i and surfaces of cell j. $\hat{n}_l$ represents the six normal vectors of the surfaces on the cubic block. Eq. (4.7) is then evaluated in Fourier space, and the results are inversely transformed to real space. More details can be referred to Ch. 2 of the thesis. The scheme (Eq. 4.7) avoids the error introduced when taking the derivative of a potential [80].

The read back signals are calculated based on the reciprocity principle [27]. We use the 3-dimensional finite difference method to obtain the magnetic scalar potential in the recorded medium space [81]. The read head consists of a magnetoresistive (MR) element and two shields. The width and thickness of the MR element are 24 nm and 4 nm respectively. Shield-to-shield spacing is set to 11 nm. The magnetic fly height of the head

is assumed to be 5 nm. A schematic of the read head is shown in Figure 4.5a. Figure 4.5b shows the sample track recorded with square-wave magnetization patterns, under the conditions $T_{\max} = 850$ K, $v = 10$ m/s, $\theta = 22.5°$, head field strength $H^{\text{appl}} = 20$ kOe, bit length $B = 19.5$ nm (1316 kfci), and an initialized AC-erased medium. Our performance comparisons are varied about this reference point except that we reduce H^{appl} to 10 kOe to better represent physically accessible conditions. Figure 4.5c shows the read back signal from the magnetization pattern in Figure 4.5b.

The performance of HAMR can be characterized by measuring transition jitter, which can be defined as $\sigma_{\text{jitter}} = \sqrt{N^{-1}\sum_i (d_i - d_m)^2}$ [82], where d_i is the zero-crossing position of the read back signal, d_m is the average position, and N is the total number of transitions, which is at least 128 in this paper for good statistics. In general σ_{jitter} can be decomposed into two components: jitter due to temporal thermal randomness σ_{thermal} and jitter due to grain irregularity σ_{grain}. Here the grain irregularity has a general meaning that includes not only shapes, sizes, and arrangement of grains, but also the distribution of their magnetic properties. In short, σ_{grain} is caused by time independent factors and σ_{thermal} is caused by temporal factors.

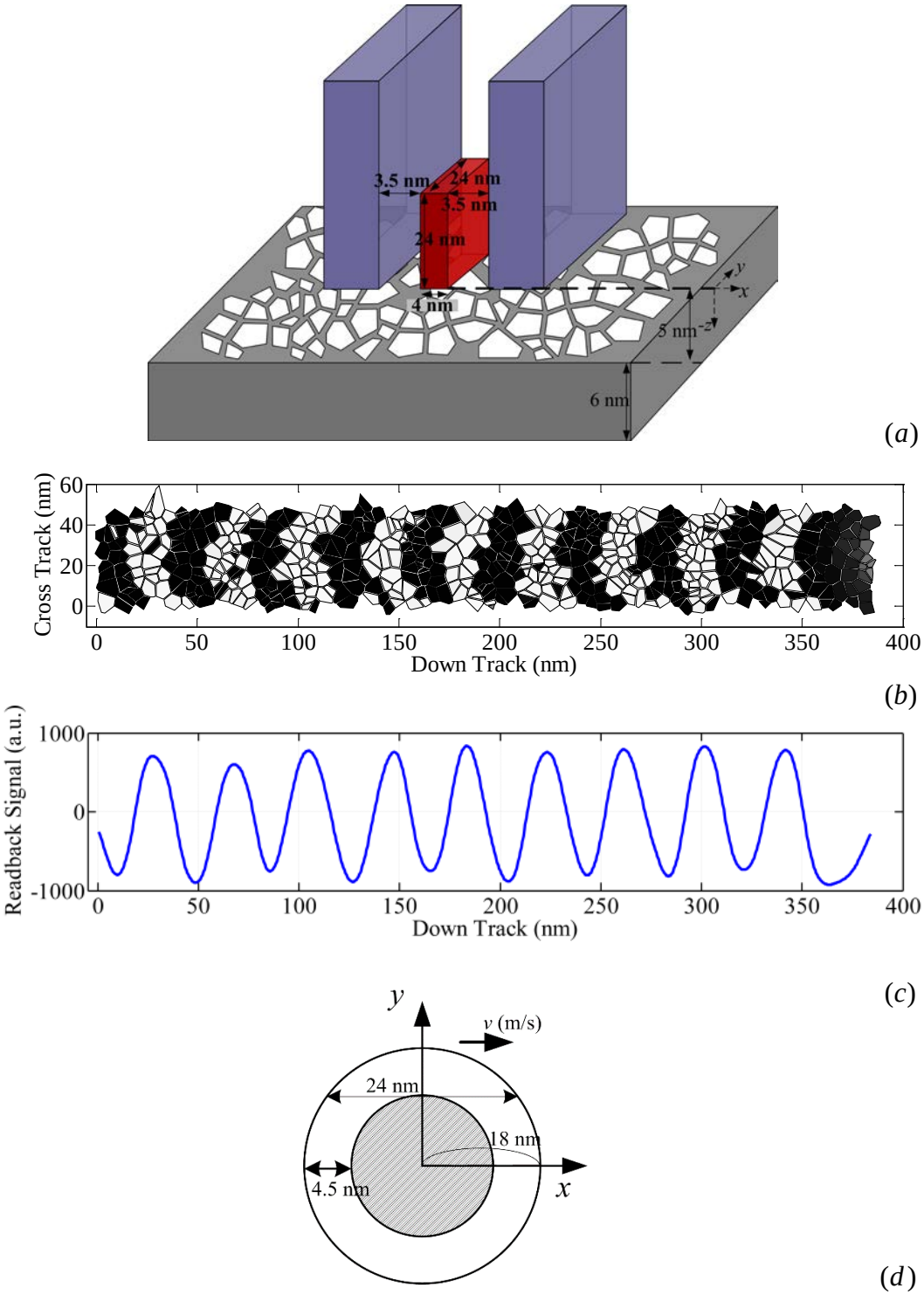

Figure 4.5: (a) Layout of MR read head and the recording medium. The downtrack direction is along the x-axis. (b) Recorded magnetization (M_z) pattern with base conditions as described in the text. (c) The readback signal of (b) with the readhead specified in (a). (d) The heat spot with T_{max} = 850 K and FWHM = 40 nm.. The graded area is of the range [700K, 850K].

A. Varying Temperature T_{max}

In HAMR, owing to the FePt's high anisotropy field at low temperature, the switching process occurs mainly at temperatures within 100 K of T_c, and occurs more quickly as T increases assuming unchanged head field strength [83], [84]. At $T > T_c$, the magnetization of grains remain near zero and are hardly controlled by the head field. Therefore, the most effective temperature region for writing is between 700 K and 600 K. Figure 4.5d shows a typical diagram of the heat spot ($T_{\max} = 850$ K). The gray area indicates $T > 700$ K, and the annulus region is for 600 K $< T <$ 700 K. As the head sweeps over the medium, the grains within the annulus experience a temperature change in a short time period τ. A small rate of temperature change dT/dt is important for successful switching (reduce σ_{thermal}). Usually, in HAMR, we also desire to have large temperature gradient dT/dx for sharp transitions (reduce σ_{grain}). If we decompose dT/dt into

$$\frac{dT}{dt} = \frac{dT}{dx}\frac{dx}{dt} \tag{4.8}$$

where the second factor is the head velocity v, we can see that dT/dt and dT/dx compete to reduce the total transition jitter σ_{jitter}.

For recording with $T_{\max} = 850$ K, the width of the annulus is 4.5 nm, and thus the shortest and longest τ will be 0.45 nS and 1.2 nS respectively (if $v = 10$ m/s). This implies that the grains near the middle of the track should switch correctly in 0.45 nS, and that the grains near the edge of the track can have more time (1.2 nS) to switch. Thus, switching accuracy can depend on cross-track position. With higher $T_{\max}$ (900 K), the heat spot has greater dT/dx, but larger dT/dt (smaller τ) as well. In contrast, a heat spot with lower

$T_{\max}$ (800 K) has smaller dT/dx but smaller dT/dt (larger τ). Figure 6a shows the simulation results for σ_{jitter}, from which we can see that the transition jitter (in the absence of intergranular exchange) does not monotonically increase or decrease with temperature, but appears to have an optimal temperature (850 K). The above argument implies that the two end data points in Figure 4.6 suffer from more σ_{thermal} and more σ_{grain}, respectively. It can also be seen that intergranular exchange coupling reduces these effects and generally produces better recording.

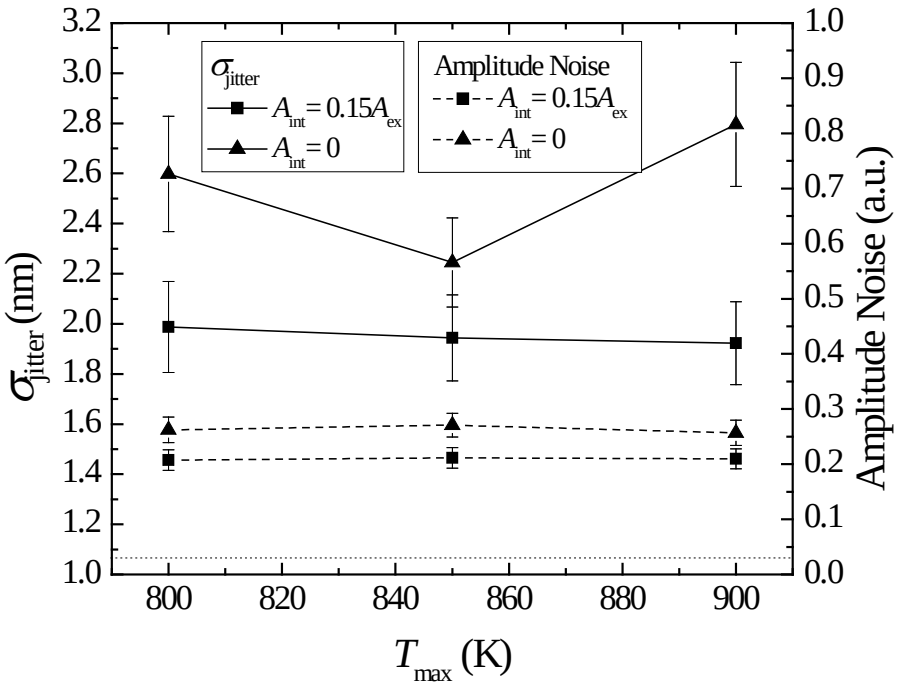

Figure 4.6: Effect on $T_{\max}$ on transition jitter and the amplitude noise of readback signal. The dotted horizontal line indicates σ_{grain} casued by the Voronoi structure only, which is 1.07 nm. A_{int} denotes the intergranular exchange coupling.

B. Write Head Velocity v

In magnetic recording, high write head velocity is always desired for achieving high data transfer rate. In (9), head velocity appears in the second factor on the right hand side of the equation, and is one of the factors on which σ_{thermal} depends. The simulation results for $\sigma_{\text{jitter}}(v)$ are shown in Figure 4.7. It can be easily seen that σ_{jitter} increases monotonically with v for both values of intergranular exchange. Also shown in Figure 4.7 are the results for a thicker (12 nm) medium. For the thicker medium, we find that the jitter goes down and the dependence on intergranular exchange also decreases. Moreover, the jitter of the thicker medium becomes less dependent on v. These results imply that both conditions (thicker medium and intergranular exchange) make grains more resistant to thermal fluctuations.

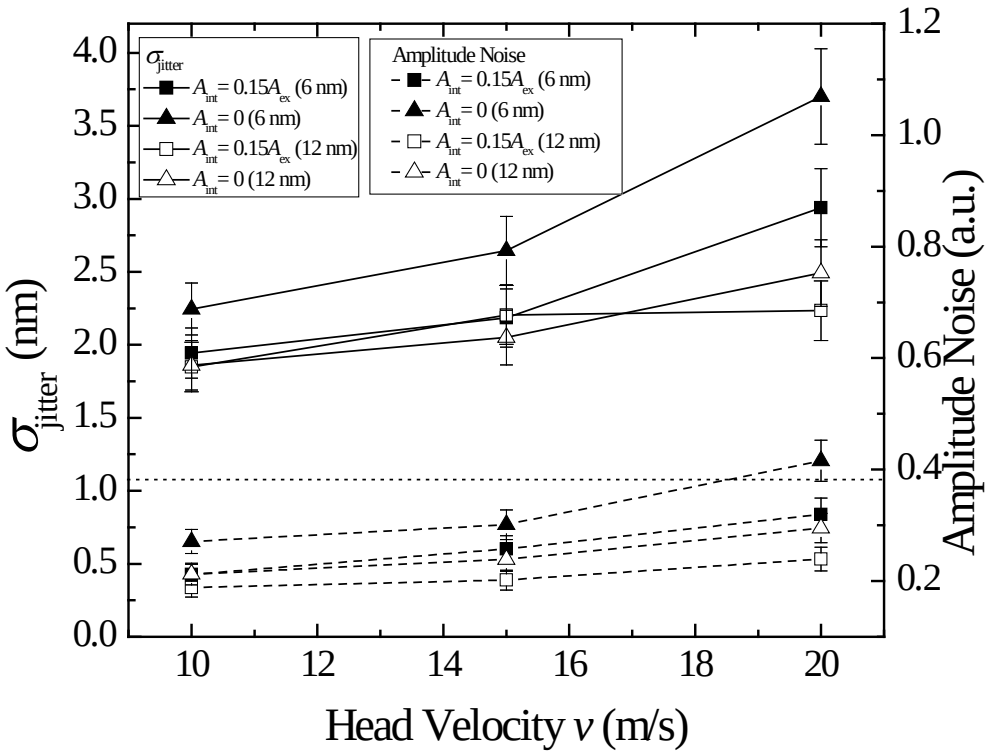

Figure 4.7: Effect of *v* on transition jitter and the amplitude noise of readback signal. The hollowed symbols represent the thicker (12 nm) medium, while solid ones represent the 6 nm medium.

C. Variation with Applied Field Angle θ

From the study of conventional perpendicular magnetic recording, it is known that a grain switches faster under a field directed at an angle to the easy axis [85]. Our atomistic simulations on a 6^3 nm^3 grain at 675 K also show that the average switching time under 20 kOe head field with $\theta = 0°$ (1.59 ns) is about 6 times slower than that with angle $\theta = 22.5°$ (0.26 ns). Therefore, it is expected that HAMR with a tilted head field has better performance, which is confirmed in previous work [86] and in our simulation results (Figure 4.8).

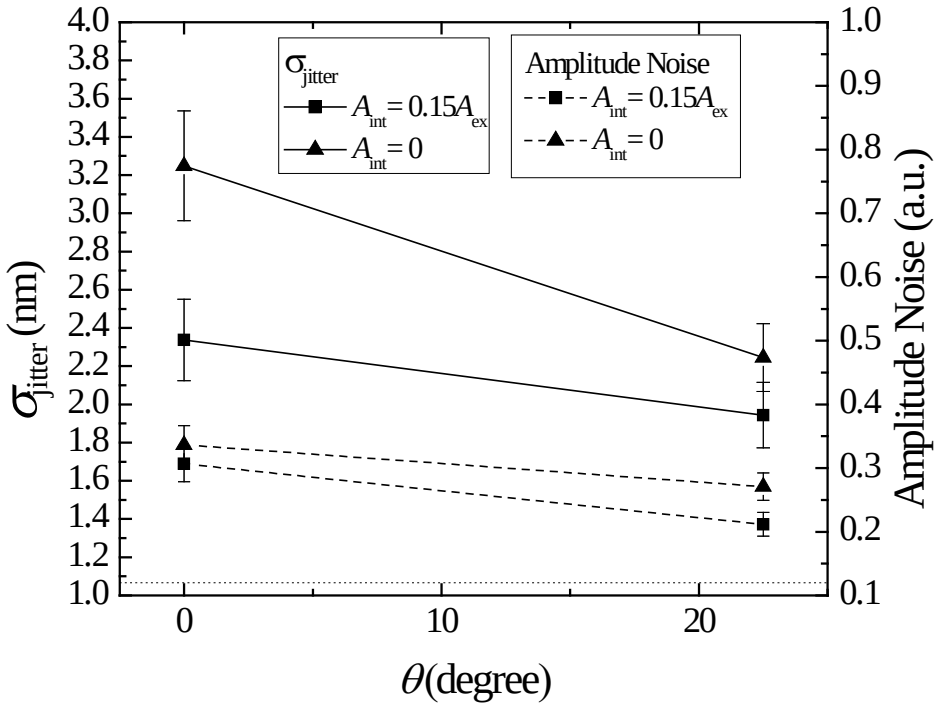

Figure 4.8: Effect of $\boldsymbol{\theta}$ on transition jitter and the amplitude noise of readback signal.

D. Variation with Applied Field Strength H^{appl}

Grains under larger head field strength are expected to switch at a higher rate and have greater thermal stability while cooling. We calculate σ_{jitter} with H^{appl} of 5 kOe, 10 kOe and 20 kOe. For $H^{\text{appl}} = 5$ kOe, the transitions are blurred and not easily distinguished. Figure 4.9 shows the cases of H^{appl} being 10 kOe and 20 kOe. The transition jitter decreases with increasing head field, although there is only about 15% improvement for 20 kOe head field. The lack of further improvement can be attributed to the reduction of recording temperature T_{R} with larger applied field. Therefore $H_{\text{K}}(T_{\text{R}})$ has a smaller thermal gradient, which implies a smaller effective write gradient and more jitter σ_{grain}. This partly cancels the

reduction of $\sigma_{thermal}$ caused by the larger applied field. The dependence on field is expected to decline with increased thickness and/or reduced velocity.

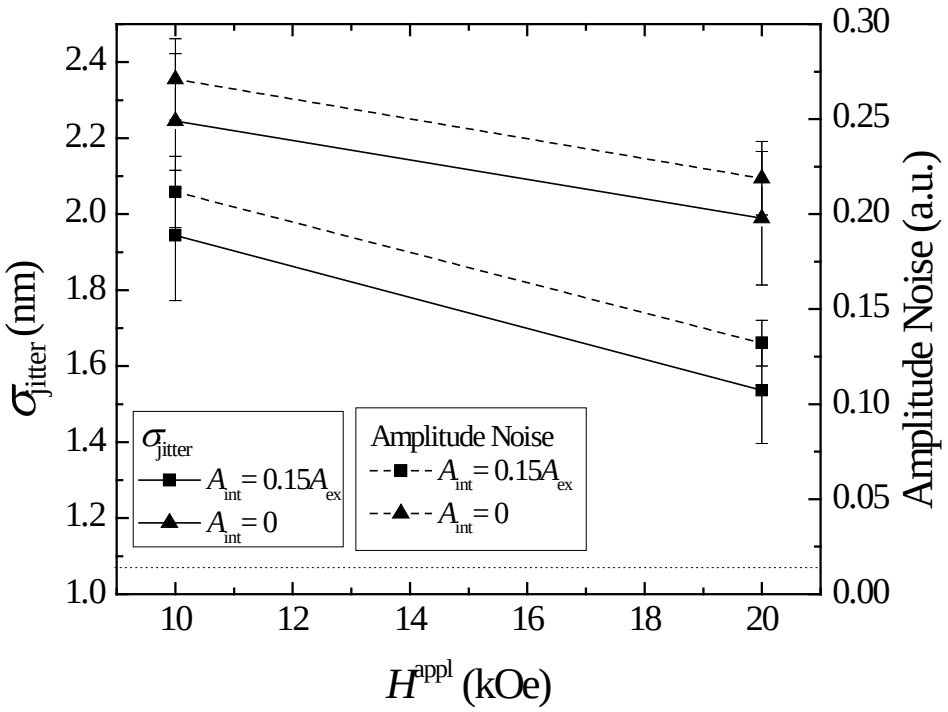

Figure 4.9: Effect on H^{appl} on transition jitter and the amplitude noise of readback signal.

4.3 Conclusion

In this chapter, large correlation lengths of spin fluctuations at temperatures near T_c enable coarse-graining of atomic spins. Renormalized material parameters for block spins are found through matching the macroscopic magnetic properties obtained on atomic and renormalized scales. Grains composed of these block spins are expected to capture similar physical dynamics near T_c to those composed of atomic spins. Quantitative agreement between renormalized and atomic scales, for predicted switching times versus applied field, helps verify the legitimacy of this approach. Using these block spins as discretized cells in

recording simulations dramatically reduces the computational time and provides a systematic approach for including variable amounts of dynamic detail.

Performance of HAMR is characterized by measuring the transition jitter. The total jitter can be separated into two components: jitter due to thermal randomness and jitter due to grains' irregularity. The simulation results suggest that jitter is reduced by intergranular exchange, nonzero canting angle of applied field, relatively large head field strength, maximum temperature of the heat spot about 150 K above the Curie temperature, and relatively low head velocity. These latter two results appear to stem directly from the physical inability to minimize both types of jitter simultaneously. These results can be used for future optimizations in HAMR.

4.4 Appendix

All the recording simulations are implemented on GPUs using NVIDIA CUDA programming. Conceptually, magnetizations of individual block spins are calculated in parallel. The FFT for magnetostatic calculations is done using CUFFT library. With the GPU, computational time is reduced by a factor 20 relative to a CPU-only implementation.

CHAPTER 5. GRAIN SIZE DEPENDENCY, ENHANCED DAMPING, AND A SIMULATION/EXPERIMENT COMPARISON

A recent technology demonstration has shown that HAMR is a workable technology for magnetic recording beyond 1 Tb/in^2 [87]. However, the question of how to push the transition width down to the grain-size limit remains open. Much work on recording simulation has been done to understand and overcome the factors limiting reduction of transition width [39], [88], [89]. In addition to the noise from grains' irregularity, other factors such as Gilbert damping, grain size, field strength, thermal profile etc., are also expected to be important. For example, the Gilbert damping determines how fast we can record information on the medium, the grain size and field strength are related to the thermal stability during writing process, and the field strength and thermal profile determine the effective anisotropy field gradient dH_{K}/dx. To achieve an optimal design for a recording system based on these factors, simulations that can mimic the realistic recording system with little loss of fidelity are needed. In this chapter, I will first discuss the renormalized damping that needs to take into account the non-equilibrium nature of HAMR. Then we will see how the recording performance depends on the size of grains. In the final part of this chapter, I will compare our simulation results with an experimental technology demonstration.

5.1 Enhanced Damping and Residual Magnons

Our previous work used $\alpha_0 = 0.005$ as the zero-temperature atomistic damping constant to predict the renormalized damping at equilibrium for different temperatures and length scales [88]. The recent electronic structure calculations by Qu and Victora suggest that α_0 should be 0.02 for $L1_0$-FePt instead of 0.005 [90]. The corresponding renormalized damping α_{renorm} is shown in Figure 5.1: the figure shows that the higher value of α_{renorm} persists to high temperatures and the ratio between high and low values remains approximately constant, independent of temperature. In Figure 5.2 we see that the transition jitters (calculated as in Ch. 4 or Ref. 88) at different grain sizes are decreased by a noticeable amount with larger α_0.

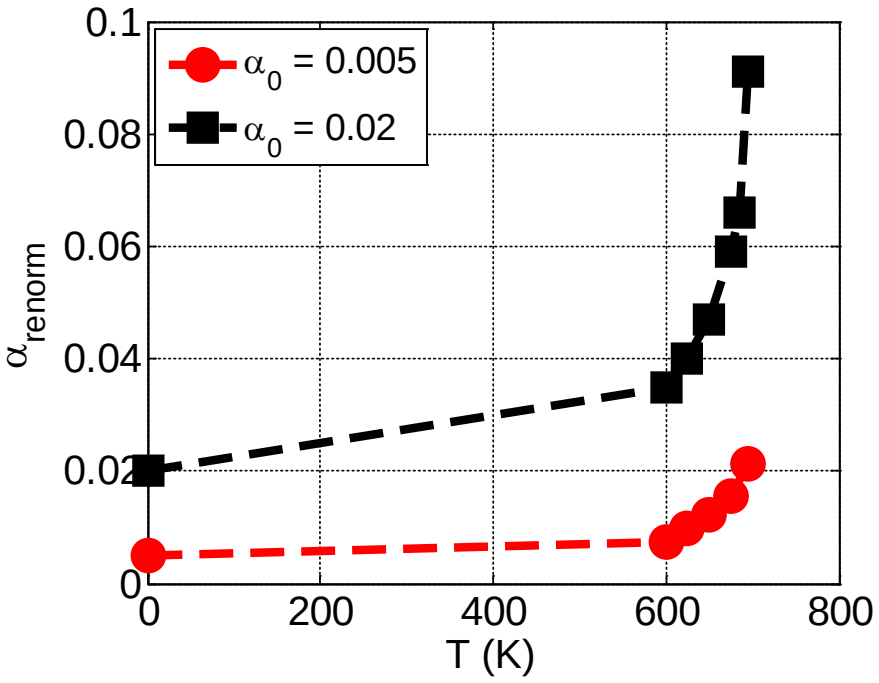

Figure 5.1: Renormalized damping constant, starting with 0.005 and 0.02, as a function of temperature. The renormalized length scale is 1.5 nm.

In HAMR, the grains, in fact, undergo non-equilibrium processes. The temperature of grains keeps changing and the switching process of grains is also non-equilibrium. When the temperature is cooling at a not-too-low rate, magnons from higher temperatures will survive for a certain amount of time and can be found at lower temperatures. These residual magnons decrease transient magnetizations and anisotropy fields of grains, and increase the damping. A more formal way of expressing this phenomenon is that the spin temperature lags behind the lattice temperature by a couple of degrees [91]. At the cooling rate of 185 K/ns, we can observe in an atomistic LLG simulation that this temperature lag is about 20 K, whereas less than 3 K lag is observed in the renormalized simulation. Although this temperature offset (17 K) is needed for a renormalized system to mimic its atomistic counterpart, we find that the practical influence on transition jitter in recording simulation is insignificant due to a very slight difference between thermal gradients at any two temperatures (600 K$<T_1$, $T_2<$700 K) separated by 17 K.

Another aspect to be considered is the enhanced damping during switching. From the previous study by Dobin and Victora [77], dynamics involving larger deviations from equilibrium leads to a much faster relaxation, from which we infer that the effective renormalized damping constant during switching should be larger than that calculated at equilibrium. From the renormalized LLG simulation, we find that requiring the same average switching probabilities of a 6^3 nm^3 grain as those obtained from atomistic simulation implies that the damping constant should be multiplied by a common prefactor of 2 at temperatures for which switching is non-negligible. We will use the newly obtained

α_{renorm} (calculated from $\alpha_0 = 0.02$) and the non-equilibrium corrections described above for all of the following calculations.

5.2 Grain Size Dependency

Recording simulations are done on media with four different average grain sizes: 3.8, 4.5, 5.6 and 6.7 nm with 1 nm grain boundaries. The media thicknesses are always set to 12 nm. We assume zero easy axis and anisotropy field distributions in the media. The recording head fields are 10 kOe with canting angle 25 degrees measured from the media easy axis, uniformly distributed throughout the media. The field reserves its direction instantaneously when writing transitions, and the head velocity is 20 m/s. The lateral distribution of the thermal profile is defined as a 2-D Gaussian with peak temperature of 850 K and tails at room temperature, with a full width at half maximum (FWHM) of 40 nm. In the vertical direction, the variation of temperature is assumed negligible. As shown in Figure 5.2, a trend of monotonic reduction in transition jitter with decreasing grain sizes can be seen. Intergranular exchange of 0 and 15% of the bulk exchange are used for separate simulations, and we find that the jitter can be further reduced with 0 exchange. However we notice that the decrease in jitter levels off towards smaller grains for the case of $\alpha_0 = 0.02$. This derives from the degradation of thermal stability during the writing process for smaller grains. The work reported by Zhu and Li. has shown that the jitter can increase with decreasing grain pitch due to the significant thermal agitation for smaller grains [89]; however in our simulation we see no jitter increase as we decrease the grain

size. This discrepancy is likely caused by our use of constant read width, relatively high thermal gradient and grain pitch no smaller than 4.8 nm.

Although using smaller grains can result in smaller jitter, it also induces an undesirable side effect: broadening of the write width. In Figure 5.3a, we plot the recorded patterns for four media that are initially DC-erased before being recorded, and then roughly measure the write widths by drawing lines at the edges of the patterns. As shown on the plots, the write widths gradually increase with decreasing grain sizes. This is caused by smaller grains being susceptible to thermal agitation. The effective write temperature is lower for smaller grains and therefore write area defined by the thermal spot enlarges. To maintain the same size of write area, lower temperature or smaller FWHM could be desired.

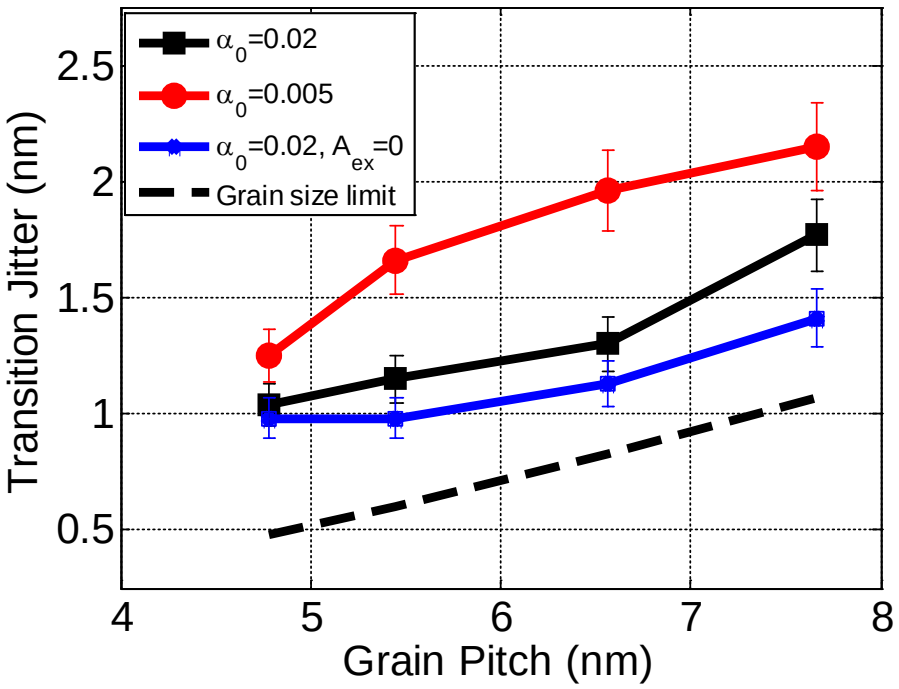

Figure 5.2: Transition jitter versus grain pitch with two different sets of modified renormalized damping constants.

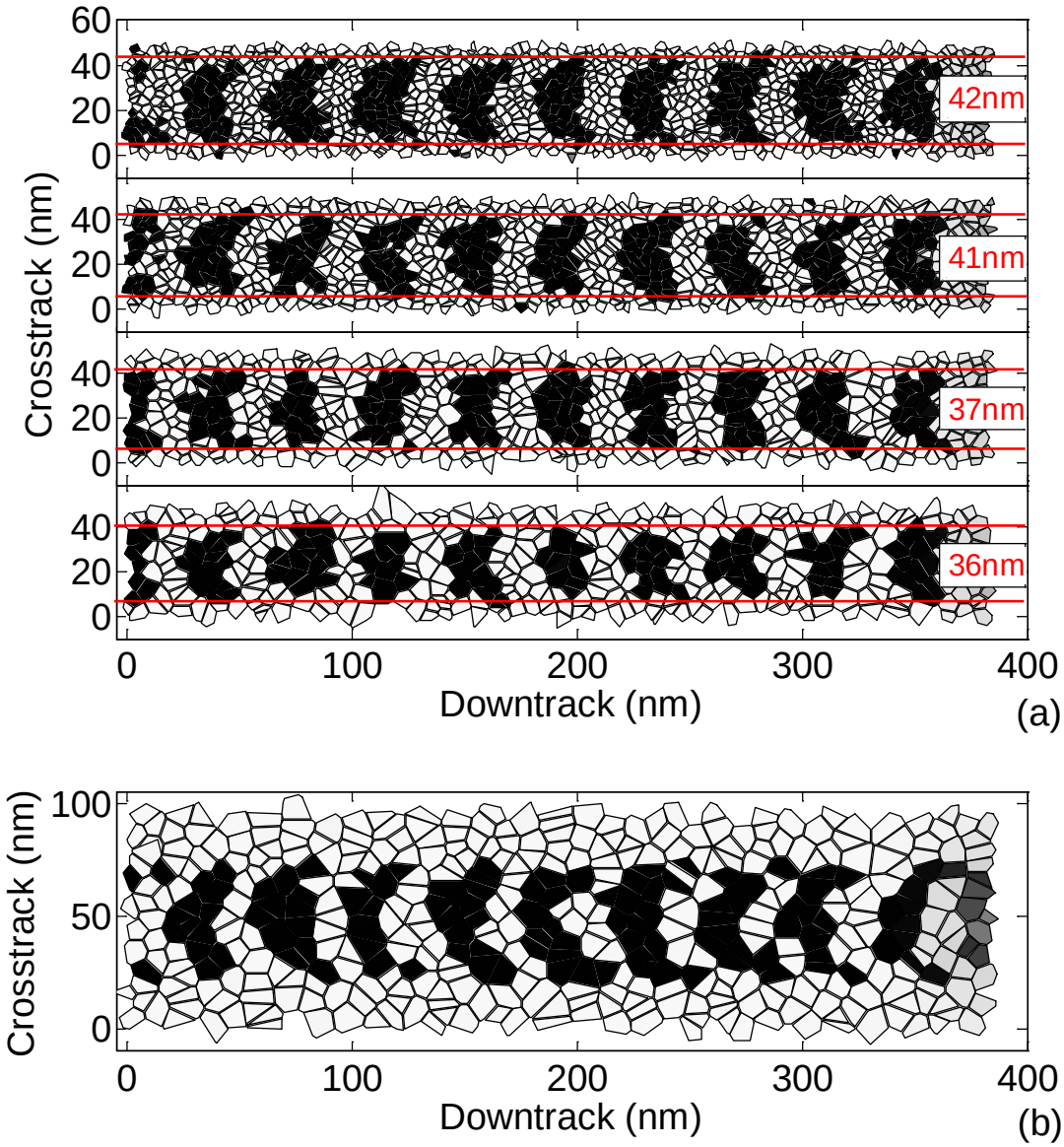

Figure 5.3: (a) Square-wave recorded patterns at different grain sizes. The red lines at the edges of the patterns are drawn to roughly measure the resultant write widths (red words). (b) Square-wave recorded pattern with average grain pitch of 10.6 nm.

5.3 Simulation/Experiment Comparison

In the last part of this letter, we present simulation results of HAMR using 1.5 nm renormalized media cells[2] with the modified non-equilibrium damping suggested in the

previous section. For realism, we try to mimic the head and media parameters as described in Ref. 86. For recording parameters, we use grains with mean diameter and standard deviation over mean being 9.6 nm (plus 1 nm grain boundaries) and 13% respectively. The anisotropy field distribution of grains at room temperature is assumed to be 15%. The medium thickness is 6 nm. The write head generates the same thermal profile as described in the previous section except that here the thermal profile's FWHM is now 57.5 nm. Head velocity is assumed to be 15 m/s. The average bit length is 19.5 nm. All read head parameters are the same as that used in our earlier work.[2], except the read width is now 36 nm. In Figure 5.3b, we show the square-wave recorded pattern on the medium that is initially DC-erased. A track width of around 55 nm can be readily seen, so that the 36 nm read width is a typical value (66% of track width) to avoid noise near the edge of the bits.

Our base recording condition uses a write field of 8 kOe tilted at 22.5 degrees; this gives a DC SNR similar to experimental demonstration [87]. As shown in Figure 5.4, we find that the DC noise is very sensitive to the write field. For a sufficiently large write field (10 kOe), no erroneously switched grain can be observed, and we attribute all the noise power to the grain boundaries. This value will, of course, be sensitive to the saturation magnetization of the thin film. The SNR is calculated by taking the power ratio of the low frequency signal to the integrated AC power in Fourier space. The transition jitter can be estimated by measuring the deviations of 192 zero-crossings of the read back signal: we obtain a jitter value of 2.00 ± 0.14 nm, which is very close to the reported values in the literature for this system [87]. For the grains of 9.6 nm mean diameter and read width of

36 nm, the jitter at the grain size limit is 1.5 nm, showing that inexact recording e.g. thermally induced jitter or inadequate gradient, increase total jitter by 33%.

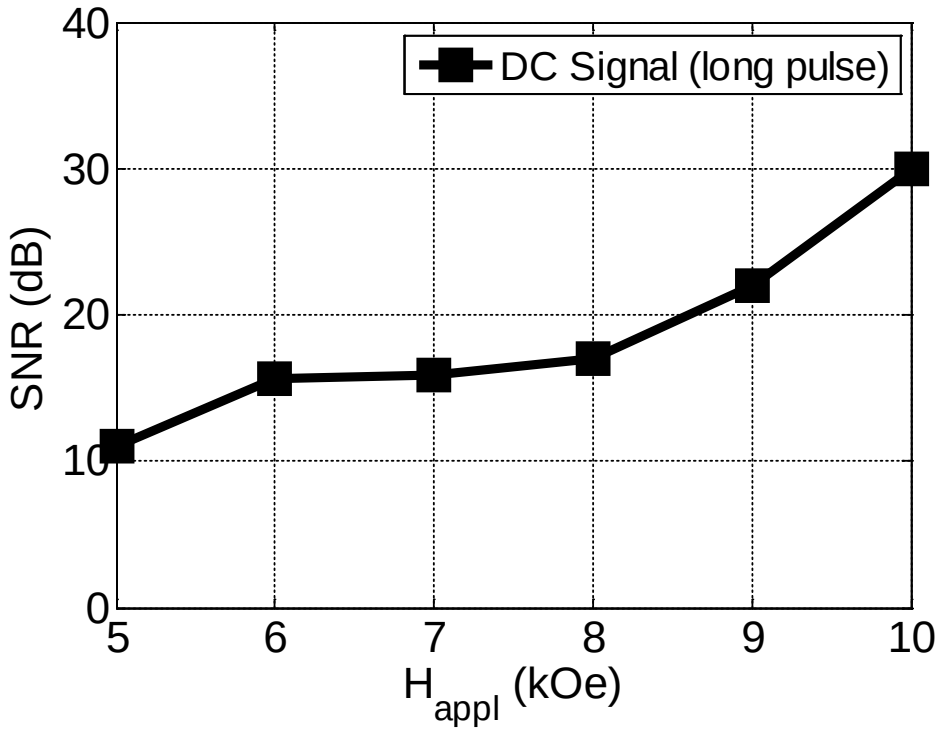

Figure 5.4: DC SNR rolls off with decreasing write field.

5.4 Conclusion

In this chapter, recording simulations are carried out to study how the grain size affects the transition jitter. The damping is modified under non-equilibrium consideration. Comparison between simulation and experiment shows good agreement. We also find that DC noise rolls off quickly with the write field below 10 kOe.

CHAPTER 6. APPROACHING THE GRAIN-SIZE LIMIT FOR JITTER USING FeRh/FePt IN HAMR

It is recognized that the high T_c of FePt imposes stringent conditions on HAMR operation from a system-level perspective [6], [92], [93]. In addition, writing at temperatures close to T_c means large thermal fluctuations. Recently a recording quadrilemma was proposed by Richter *et al*. [94] showing that thermally induced recording errors will be the limiting factor to the ultimate recording system that combines HAMR with a one-grain-per-bit recording scheme. Utilizing soft/hard ECC (Exchange Coupled Composite) media for reducing thermally induced errors of HAMR has been discussed in previous publications [75], [95]. However, we notice that the coupling of a relatively soft layer to $L1_0$-FePt always dilutes effective anisotropy. The effective anisotropy field gradient dH_K/dx will deteriorate, as can be seen in Table 1 of Ref. 95 and Figure 6.1 of this paper. Moreover, ultimately such anisotropy dilution will raise the lower limit of $L1_0$-FePt particle size that satisfies the thermal stability requirement at room temperature. Therefore an ideal design of ECC media should be that the soft assisting layer vanishes sharply at a temperature beyond room temperature but well below T_c of FePt. In 2003, Thiele *et al*. proposed the magnetic bilayer structure FeRh/FePt as a potential medium for heat-assisted magnetic recording [96]. FeRh is known to exhibit a sharp AFM-FM transition at a critical temperature T_{tr}, which can be tuned from 400 K to 500 K by doping [96]. This exotic property would be a perfect solution to all the emerging issues above. However, fabrication of the ordered FeRh alloy thin films is generally difficult because the lattice structure and

magnetic properties are very sensitive to the stoichiometry. Moreover, it is difficult to maintain a sharp AFM-FM transition in ultrathin FeRh films due to the stress present in the films [97]. To the best of our knowledge, the thinnest FeRh with a temperature range of 50 K across the phase transition temperatures is 14 nm [98]. In this chapter, we will further examine the possibility of using a double-phase FeRh/FePt structure for HAMR media, and compare it with a single-phase FePt medium. To be a true representation of currently achievable FeRh thickness, the thickness on which we focus in this paper is 15 nm.

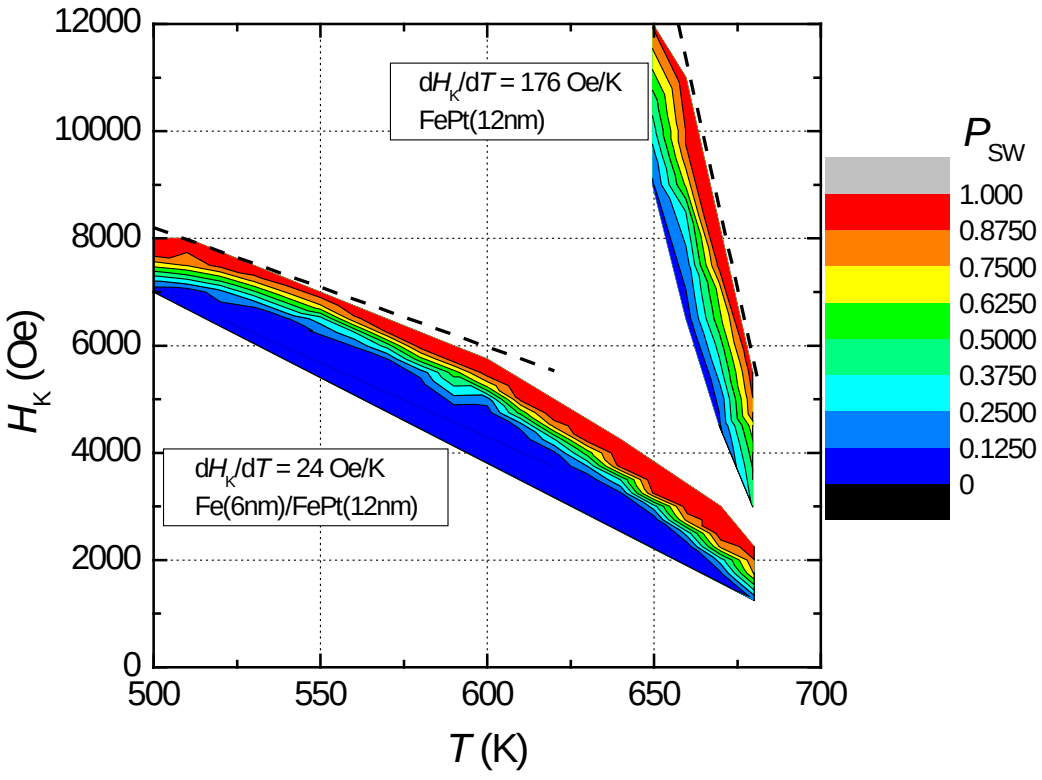

Figure 6.1: Switching probabilities at various anisotropy fields and temperatures. Although the distribution of P_{sw} is narrower for Fe/FePt grain, the H_K gradient with temperature is much smaller than FePt.

6.1 Modeling Method

The zero-temperature magnetic properties of the FePt layer are as follows: The saturation magnetization $M_s(T=0) = 1100$ emu/cm^3 (1.1×10^6 A/m), the uniaxial anisotropy constant $K_u(T=0) = 7\times10^7$ erg/cm^3 (7×10^6 J/m^3), the exchange stiffness constant $A(T=0)$ = 1.1×10^{-6} erg/cm (1.1×10^{-11} J/m), the Kambersky damping constant $\alpha(T=0)$ = 0.02, and the Curie temperature T_c = 700 K. For the FeRh layer, we extract the data points from Figure 2 in Ref. 96. The temperature range of the phase transition is assumed to be 450–470 K when cooling, within which $M_s(T)$ decreases linearly from 1200 emu/cm^3 to 100 emu/cm^3. The Curie temperature T_c of FeRh is read as 760 K. We ignore the crystalline anisotropy of FeRh. Using the approximately proportional relationship between $A(T=0)$ and T_c [57], the constant $A(T=0)$ for FeRh is assumed 1.2×10^{-6} erg/cm. The interface exchange between FeRh and FePt is assumed to be $\sqrt{A^{FePt}A^{FeRh}}$. All the simulations are done at the length scale of 1.5 nm using cubic elements. The temperature-dependent renormalized magnetic parameters are calculated using our previously developed technique [88], [99], except that we use 0.002 for FeRh's zero-temperature Kambersky damping α [100].We also assume that the FeRh layer is deposited in the (001) direction, with AF3 spin configuration [101]. In AF3 configuration, the alternating spin directions result in, on average, no exchange effect on FePt at the interface (i.e., no exchange bias effect). Therefore in simulations we simply set the saturation magnetization of FeRh to a small value (100 emu/cm^3) when the temperature T < 450 K.

6.2 Transition Width Estimates

To approximate the HAMR process, the switching probability P_{sw} as a function of T_{rev} is calculated by simulating 256 grains, packed in a 96×96 nm^2 film, with temperatures cooling from 700 K to 300 K at various constant cooling rates. T_{rev} is defined as the temperature at which the static external field (12 kOe, canting angle 45°) is reversed. The lateral dimensions of each grain are 6×6 nm^2. We calculate $P_{\mathrm{sw}}(T_{\mathrm{rev}})$ for three cases: Two FePt media with thicknesses of 6 and 12 nm, denoted as FePt(6nm) and FePt(12nm) respectively, and one composite FeRh(15nm)/FePt(6nm) medium. For FePt grains, we assume the grains are isolated, i.e., there are no intergranular exchange and magnetostatic fields among the grains. Demagnetization fields within individual grains are also ignored. For FeRh/FePt, no exchange and magnetostatic fields are assumed, except that the FeRh layer is assumed continuous in order to best approximate the experimental situation. Thus there would be some coupling effects between grains of the FePt layer via the FeRh layer. The results are plotted in Figure 6.2a and 6.2b. In plots of P_{sw} versus T_{rev}, the temperature difference (TD), between high, e.g. P_{90}, and low switching probabilities, e.g. P_{10}, can be regarded as a qualitative measure of transition width, and therefore transition jitter. TD's as a function of cooling rate for the three cases are shown in Figure 6.3. We can see that TD's for single-phase FePt grains are less dependent on cooling rate than for composite FeRh/FePt grains. The magnitude of TD is affected by dH_{K}/dT, thermal stability at writing $(M_{\mathrm{s}}H_{\mathrm{appl}} + K_{\mathrm{u}})V/k_{\mathrm{B}}T$, and switching times of the grains. H_{appl} denotes the applied field and V the grain volume. Therefore in Figure 6.3 we can see that TD is smaller for thicker grains and decreases with cooling rate. The advantage of using FeRh/FePt is

manifest at the cooling rate of 150 K/ns, where TD is about ¼ of that of single-phase FePt. Also shown in Figure 6.3 is the detriment of using composite Fe/FePt grain, where TD is three times larger than that of FePt. The magnetic parameters for the Fe layer are assumed to be $M_s(T = 0) = 1600$ emu/cm^3, $A(T = 0) = 1.6\times10^{-6}$ erg/cm, $\alpha(T = 0) = 0.002$ and negligible anisotropy.

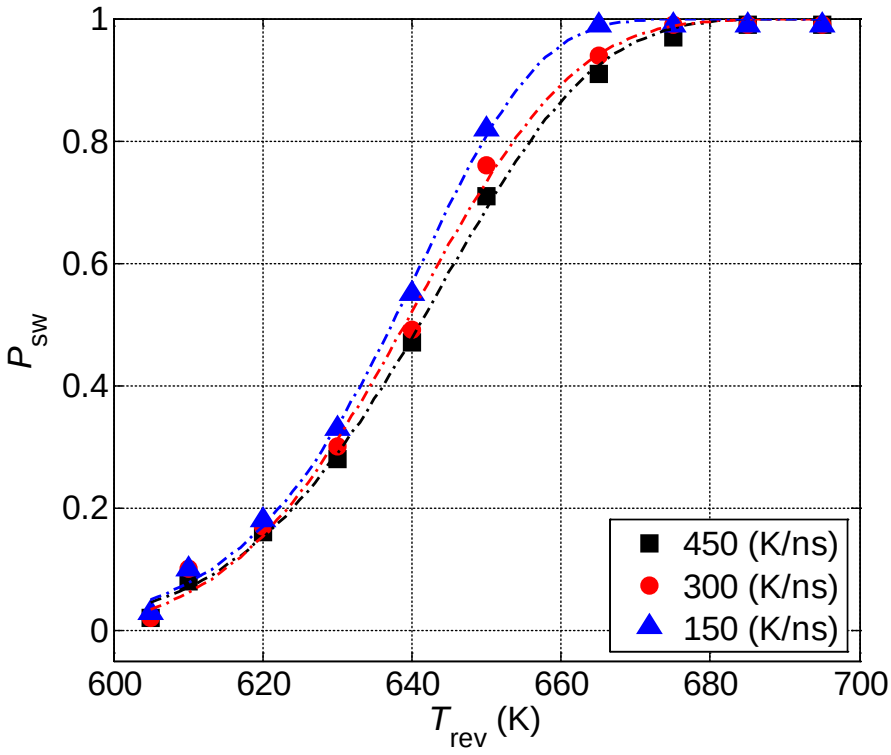

Figure 6.2a: Switching probabilities as a function of temperature (T_{rev}) at which fields reverse directions with different cooling rates. H_{appl} is 12 kOe at a 45° angle. (a) 256 6×6×6 nm^3 FePt grains

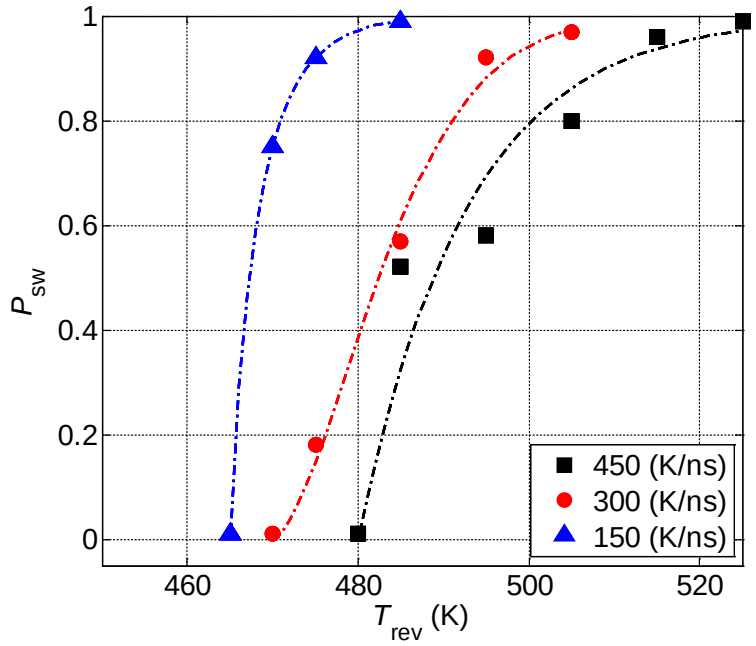

Figure 6.2b: Switching probabilities as a function of T_{rev}. H_{appl} is 12 kOe at a 45° angle. (b) 256 6×6×21 nm^3 FeRh(15nm)/FePt(6nm) grains

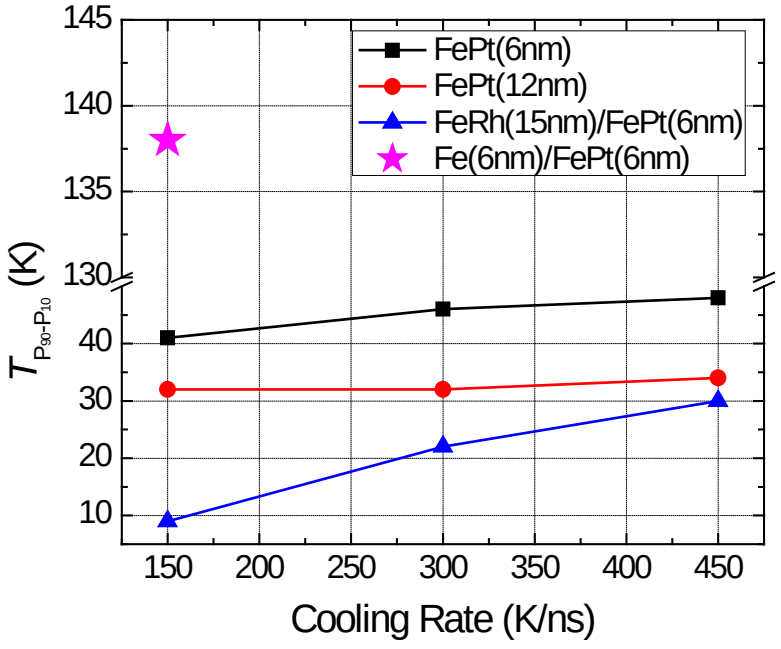

Figure 6.3: The temperature differences between high (P_{90}) and low (P_{10}) switching probabilities at various cooling rates for FePt and composite FeRh/FePt grains.

6.3 Switching Times

In FeRh(t_{soft})/FePt(t_{hard}) media (with the thickness of the FePt layer t_{hard} = 6 nm) the thickness of the FeRh layer t_{soft} can affect the switching behavior significantly. Following the analytic formula used to estimate the domain wall thickness l_{DW} in the soft (FeRh) layer [105->102], we obtain $l_{\mathrm{DW}} \approx 4.5$ nm at H_{appl} = 12 kOe. As we vary t_{soft} from 6 nm to 18 nm, the grain will gradually change behavior from single-domain to multi-domai. As t_{soft} increases, the switching behavior becomes less predictable due to more complicated domain structures occurring in the FeRh layer. Using the same FeRh/FePt test sample as described in Sec. 6.2, we calculate the average switching time t_{sw} dependence on t_{soft} and H_{appl}. t_{sw} is defined as the time that the average magnetization $\langle M \rangle$ of the FePt layer of grains takes from the maximum (all pointing upward) to 0 without subsequently swinging back to positive values. We also define the lower (upper) bounds of the switching times as the times that 10% (90%), respectively, of the grains switch. The results are shown in Figure 6.4a. We can see that t_{sw} varies non-monotonically with t_{soft}. For t_{soft} from 6 nm to 10.5 nm, $H_{\mathrm{appl}} = 8$ kOe favors switching more than $H_{\mathrm{appl}} = 12$ kOe. For t_{soft} larger than 12 nm, $H_{\mathrm{appl}} = 12$ kOe produces quicker switches. To understand this, we calculate the switching time of two hard/soft ECC grains at T = 0 K as a function of H_{appl} with 45° canting angle. The overall dimensions of the two ECC grains are 6×6×13.5 nm^3 and 6×6×21 nm^3. One of them has t_{soft} = 7.5 nm and t_{hard} = 6 nm, denoted as Grain #1, and the other one has t_{soft} = 15 nm and t_{hard} = 6 nm, denoted as Grain #2. The magnetic properties of the two phases of each grain are equal to those of FeRh and FePt at T = 470 K respectively. As shown in Figure 6.4b, Grain #1, for example,

can switch in a very short time (< 50 pS) with fields ranging from 8–12 kOe. With fields larger than 12 kOe, the switching time increases and then decreases with increasing fields. This counterintuitive switching behavior is due to the wide plateau in the energy contour with H_{appl} larger than the effective H_{K} of the system. If the field is comparable with the effective H_{K}, the energy contour becomes more complex (or distorted) and the wide plateau vanishes, resulting in fast switching. This phenomenon has been observed and partially explained both in ECC and single-phase structures [103], [104], [105]. For the grain with thicker soft layer (Grain #2), the curve shifts to a smaller field range with a smaller peak switching time. Since the 15-nm-thick soft layer can accommodate more than one domain wall within the studied field range, the energy contour will be much more complex than that of Grain #1. However we can qualitatively think that a thicker soft layer requires less field to switch [102], and therefore results in the shift of the curve of Grain #2 relative to that of Grain #1. Next, for the given thickness of FeRh (15 nm), we optimize the magnitude of H_{appl} and its canting angle against the easy axis of the grain. We calculate the average switching times t_{sw}'s (as defined before) of an ensemble of 100 individual grains of Grain #2 at different magnitudes and canting angles of H_{appl}. As shown in Figure 6.5, to achieve a shorter switching time, H_{appl} should either be >10 kOe (canting angle 40°–45°) or very near 5.5 kOe (canting angle 45°). If tracing along the white dashed line in the figure, we can obtain a similar curve as in Figure 6.4b.

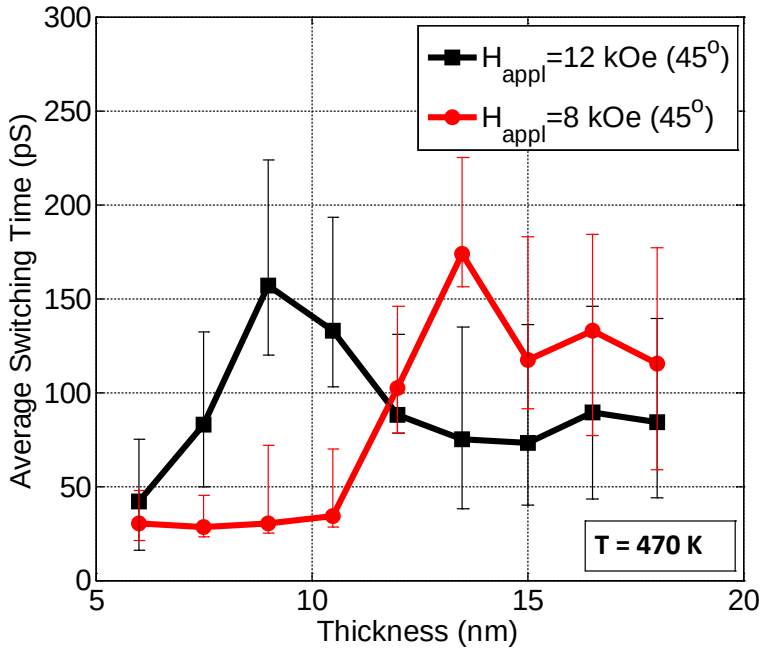

(*a*)

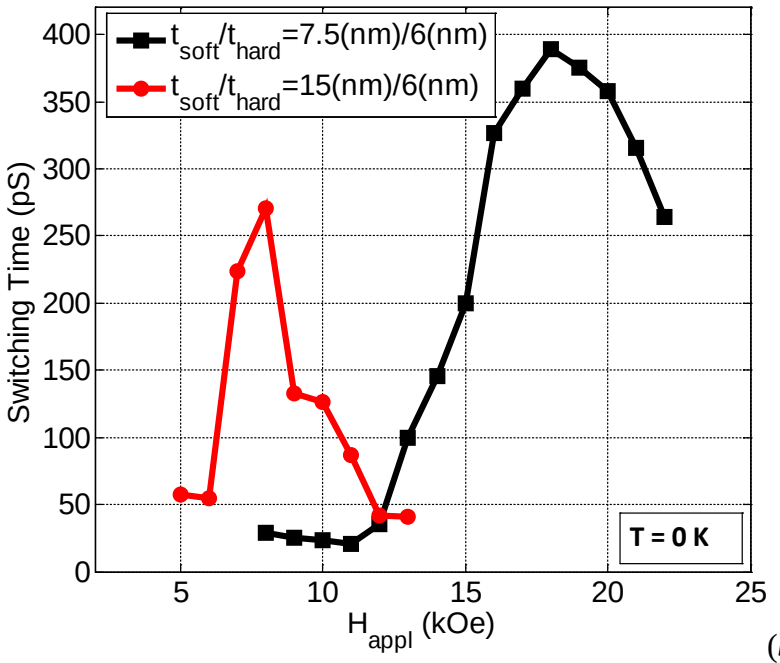

(*b*)

Figure 6.4: Applied-field-dependent (a) average switching times of a 96×96×21 nm^3 thin film composed of composite FeRh(15nm-thick, continuous)/FePt(6^3 nm^3, granular), and (b) switching times of 6×6×21 and 6×6×13.5 nm^3 soft/hard ECC grains. Applied field angle is 45°.

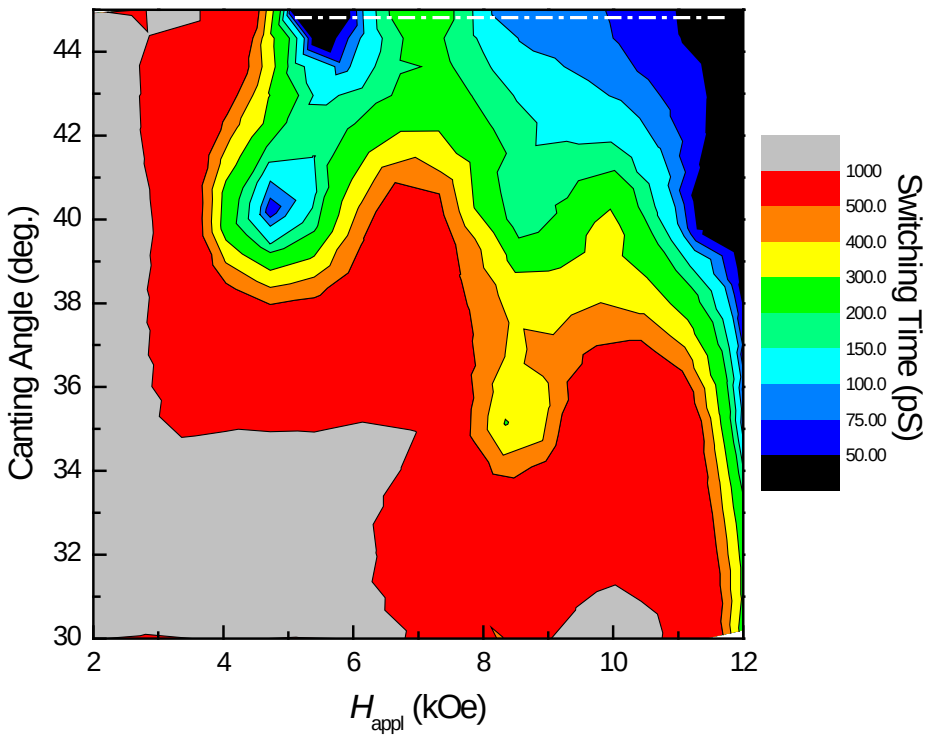

Figure 6.5: Switching time distribution on the coordinates of field magnitude and canting angle.

6.4 Recording Simulations

In the last section, we implement HAMR recording simulations on FePt- and FeRh/FePt-based media and compare their transition jitters. Both of the two media are composed of 600 Voronoi grains packed in a 384×48 nm^2 film with mean diameter and standard deviation over mean being 5.6 nm (plus 1 nm grain boundaries) and 20 % respectively. The crystalline anisotropy field distribution of grains is assumed 0, although shape anisotropy increases this value. All magnetostatic interactions are included. We model the HAMR recording processes on FePt-based media for two thicknesses, 6 and 12

nm, and on FeRh(15nm)/FePt(6nm)-based media. For the thermal profile, we assume a 2-D Gaussian in the lateral directions and uniform distribution in the perpendicular direction. The Gaussian has peak temperature $T_{\max}$ and tails at 300 K, with a full width at half maximum (FWHM) of 40 nm, moving in the downtrack direction (long side) at 20 m/s. In order to make fair comparisons, the write width for the two media should be approximately equal to avoid possible curvature effect on jitter. Therefore we use $T_{\max} = 850$ K for FePt-based media and $T_{\max} = 590$ K for FeRh/FePt-based media. An immediate advantage is that recording with FeRh/FePt-based media greatly reduces the heat experienced by the near-field transducer. The applied field H_{appl} is 12 kOe with canting angle 45°, uniformly distributed in the media. The field reverses direction immediately. The transition jitter is estimated from deviations of 144 zero-crossings of the read back signal for each case. The read head parameters are the same as that used in our previous paper [88]. Figure 6.6 shows one of the typical recorded patterns of the three media FePt(6nm), FePt(12nm) and FeRh(15nm)/FePt(6nm). The transition jitters are 1.22, 1.14 and 0.98 nm respectively. In an attempt to know how close we are to the grain-size limited jitter, we employ the formula used to predict theoretical grain-size limited jitter [106]

$$\sigma^2_{\text{jitter,theory}} = \frac{1}{WR/D}\frac{D^2}{12}, \tag{6.1}$$

except that here D is defined as $D_{\text{avg}} + Bnd$, where D_{avg} is the average grain diameter (5.6 nm) and Bnd is the grain boundary (1 nm). WR is the read width (24 nm). The jitter calculated from Eq. (6.1) gives 1.0 nm, from which we can infer that the obtained jitter of

0.98 nm for FeRh/FePt-based media is fairly close, or already equal, to the grain-size limited value.

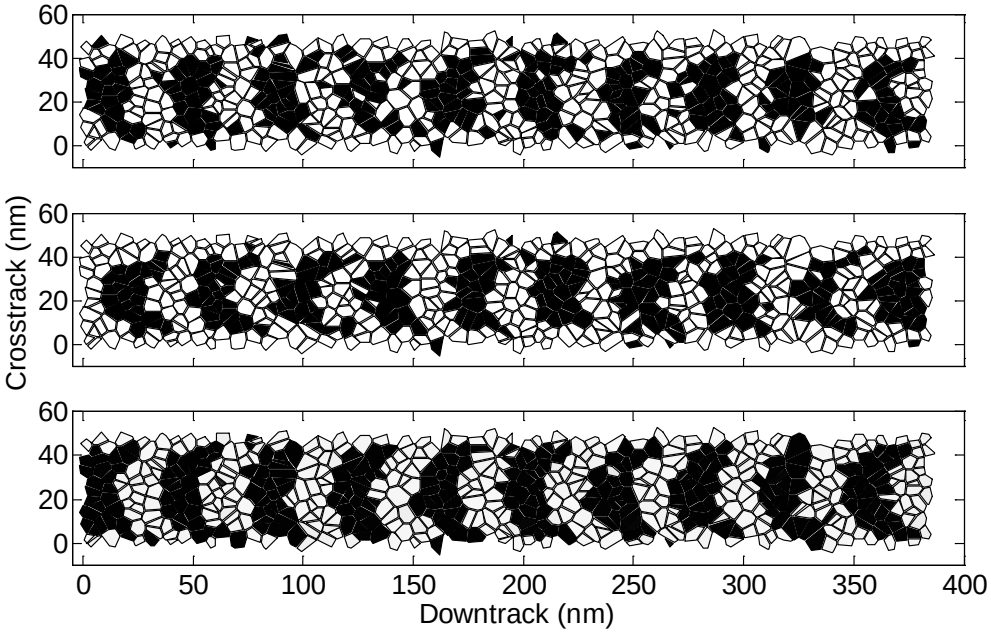

Figure 6.6: Recorded patterns: (a) FePt(6nm), v = 20 m/s, σ_{jitter} = 1.22 nm; (b) FePt(12nm), v=20 m/s, σ_{jitter} = 1.14 nm; (c) FeRh(15nm)/FePt(6nm), v = 20 m/s, σ_{jitter} = 0.98 nm.

6.5 Conclusion

The previously proposed FeRh/FePt for HAMR seems to be an excellent solution for the issues confronting HAMR from many perspectives. Our calculations show that for FeRh to best assist the switching of FePt, the cooling rate has to be low enough to ensure sharp transitions. They also show that 15-nm-thick FeRhrequires the field to have particular magnitudes of either very near 5.5 kOe or >10 kOe and a canting angle around 45° for successful switching within a limited amount of time (100 pS).The recording simulations

verify that by the use of FeRh/FePt media for HAMR recording, we can obtain jitter almost equal to the grain-size limited value.

CHAPTER 7. SUMMARY

In the final chapter of this thesis, the results presented in the previous chapters are summarized. First, a torque-based method is developed to calculate magnetic anisotropy constants and fields in the time domain at different temperatures. It is important to have the information of anisotropy field varying with time because in HAMR the thermal fluctuations in sub-ns time frame will be a prominent noise source during recording processes. The renormalization group theory allows the aggregation of a number of atomic spins into spin blocks at high temperatures especially near the Curie temperature. The magnetic parameters for renormalized media cells are then found and serve as new inputs to the LLG equations on renormalized scales. Switching time tests validate the use of renormalized system to represent the original atomistic system, and the computational time can be drastically reduced without losing much fidelity of the original physical system. The correct damping constant should be used due to its large influence on the recording performance. The simulation results show that the grains of size smaller than 4 nm will not be advantageous due to large thermal fluctuations at the high write temperature. FeRh as an assisting layer atop the FePt layer is found to be a promising solution to the thermal issues emerging with HAMR, allowing writing the transitions to the grain size limit.

BIBLIOGRAPHY

[1] (2013, Nov.) HGST Ships 6TB Ultrastar® He6 Helium-filled Drives for High-density, Massive Scale-out Data Center Environments. [Online]. Available: http://www.hgst.com/press-room/press-releases/hgst-ships-6TB-Ultrastar-HE6-helium-filled

[2] S. Thompson, "The discovery, development and future of GMR: The Nobel Prize 2007," *J. Phys. D: Appl. Phys.*, vol. 41, p. 093001, 2008.

[3] S. Piramanayagam, "Perpendicular recording media for hard disk drives," *J. Appl. Phys.*, vol. 102, p. 011301, 2007.

[4] R. Victora and X. Shen, "Exchange Coupled Composited Media," *Proc. IEEE*, vol. 96, no. 11, pp. 1799–809, Nov. 2008.

[5] R. Wood, M. Williams, A. Kavcic, and J. Miles, "The Feasibility of Magnetic Recording at 10 Terabits Per Square Inch on Conventional Media," *IEEE Trans. Magns.*, vol. 45, no. 2, pp. 917–923, Feb. 2009.

[6] M. Kryder, E. Gage, T. McDaniel, W. Challener, R. Rottmayer, G. Ju, Y.-T Hsia, and M. Erden, "Heat Assisted Magnetic Recording," *Proc. IEEE*, vol. 96, no. 11, pp. 1810–1835, Nov. 2008.

[7] A. Dobin, O. Heinonen, K. Gao, R. Veerdonk, R. Lynch, J. Xue, D. Weller, P. Asselin, M. Erden, and R. Brockie, "Recording on Bit-Patterned Media at Densities of 1 Tb/in^2 and Beyond," *IEEE Trans. Magn.*, vol. 42, no. 10, pp. 2255–2260, Oct. 2006.

[8] C. Ross, "Patterned Magnetic Recording Media," *Annu. Rev. Mater. Res.*, vol. 31, pp.

203–235, 2001.

[9] S. Wang and A. Taratorin, *Magnetic Information Storage Technology*. New York: Academic, 1999.

[10] W. Heisenberg, "Zur theorie des ferromagnetismus," *Z. Phys*, vol. 49, pp. 619–636, 1928.

[11] Kryder, M.H., Review of nonconventional recording: Approaches to 100 Gbit/in2, *The Magnetic Recording Conf*., Minneapolis, MN, 1993.

[12] H. Katayama, S. Sawamura, Y. Ogimoto, J. Nakajima, K. Kojima, and K. Ohta, *J. Magn. Soc. Jpn.*, vol. 23, Suppl. S1, p. 233, 1999; H. Nemoto, H. Saga, H. Sukeda, and M. Takahashi, *Proc. of MORIS'99, J. Magn. Soc. Jpn.*, vol. 23, Suppl. S1, p. 229, 1999; H. Saga, H. Nemoto, H. Sukeda, and M. Takahashi, *Proc. Of MORIS'99, J. Magn. Soc. Jpn.*, vol. 23, Suppl. S1, p. 225, 1999.

[13] J. J. M. Ruigrok, R. Coehoorn, S. R. Cumpson, and H. W. Kesteren, "Disk recording beyond 100 Gb/in^2: Hybrid recording?" *J. Appl. Phys.*, vol. 87, p. 5398, 2000.

[14] K. Matsumoto, A. Inomata and S.-Y. Hasegawa, "Thermally Assisted MAgentic Recording," *FUJITSU Sci. Tech. J.*, vol. 42, no. 1, pp. 158–167, 2006.

[15] "Voronoi diagrams." Wikipedia: The Free Encyclopedia. Wikimedia Foundation, Web. 10 Aug. 2004. <http://en.wikipedia.org/wiki/Voronoi_diagram>

[16] Y. Peng, J. Zhu, and D. Laughlin, "$L1_0$ FePt–MgO perpendicular thin film deposited by alternating sputtering at elevated temperature," *J. Appl. Phys*., vol. 99, p. 08F907, 2006.

[17] Y. Kawada, Y. Ueno, and K. Shibata, ”Magnetic properties, microstructure, and read-write performance of $CoSiO_2$-Pt granular multilayer perpendicular recording media,” *IEEE Trans. Magn.*, vol. 40, no. 4, pp. 2489–2491, July 2004.

[18] Y. Kawada, Y. Ueno, and K. Shibata, “Co-Pt multilayers perpendicular magnetic recording media with thin Pt layer and High perpendicular anisotropy,” *IEEE Trans. Magn.*, vol. 38, no. 5, pp. 2045–2047, Sep. 2002.

[19] S. Kardelky, A. Gebert, O. Gutfleisch, V. Hoffmann, and L. Schultz, “Prediction of the oxidation behabiour of Sm–Co-based magnets,” *J. Magn. Magn. Mater.*, vol. 290–291, pp. 1226–1229, 2005.

[20] L. Schultz, A. El-Aziz, G. Barkleit, and K. Mummert, “Corrosion behavior of Nd–Fe–B permanent magnetic alloys,” *Mat. Sci. Eng.*, vol. A267, pp. 307–313, 1999.

[21] T. Klemmer, D. Hoydick, H. Okumura, B. Zhang, and W. A. Soffa, “Magnetic hardening and coercivity mechanisms in L10 ordered FePd ferromagnets,” *Scripta Metallurgica et Materialia*, vol. 33, p. 1793, 1995.

[22] J.-U. Thiele, K. R. Coffey, M. F. Toney, J. A. Hedstrom, and A. J. Kellock, “Temperature dependent magnetic properties of highly chemically ordered $FePt_{55-x}Ni_xPt_{45}$ $L1_0$ films,” *J. Appl. Phys.*, vol. 91, p. 6595, 2002.

[23] T. Moriya, H. Nakata, K. Komiyama, S. Okamoto, N. Kikuchi, O. Kitakami and T. Shimatsu, “Curie temperature and magnetic anisotropy for $L1_0$ type Fe-Pt-Cu single crystal films,” Session BT-05, *58th MMM conference*, Denver (2013).

[24] O. Hovorka, S. Devos, Q. Coopman, W. Fan, C. Aas, R. Evans, X. Chen, G. Ju and R. Chantrell, "The Curie temperature distribution of FePt granular magnetic recording media," *Appl. Phys. Lett*., vol. 101, p. 052406, 2012.

[25] C. Rong, D. Li, V. Nandwana, N. Poudyal, Y. Ding, Z. Wang, H. Zeng, and J. Liu, "Size-Dependent Chemical and Magnetic Ordering in $L1_0$-FePt Nanoparticles," *Adv. Mater*., vol. 18, no. 22, pp. 2984–2988, 2006.

[26] H. Richter, N. Supper, B. Wilson, and B. Terris, "Magnetic Recording Near the Grain Size Limit," *IEEE Trans. Magn*., vol. 48, no. 11, pp. 3887–3890, Nov. 2012.

[27] H.N. Bertram, *Theory of Magnetic Recording*. Cambridge, U.K.: Cambridge Univ. Press, 1994.

[28] X. Wang and H.N. Bertram, "Simple transition parameter expression including grain size and intergranular exchange," *J. Appl. Phys*., vol. 93, p. 7005, 2003.

[29] X. Wang, B. Valcu, and N.-H. Yeh, "Transition width limit in magnetic recording," *Appl. Phys. Lett*., vol. 94, p. 202508, 2009.

[30] J. Caroselli and J. Wolf, "Applications of a new simulation model for media noise limited magnetic recording channels," *IEEE Trans. Magn*., vol. 32, no. 5, pp. 3917–3919, Sep. 1996.

[31] K. Barmak, J. Kim, L. H. Lewis, K. R. Coffey, M. F. Toney, A. J. Kellock, and J.-U. Thiele, "Stoichiometry–anisotropy connections in epitaxial $L1_0$ FePt(001) films," *J. Appl. Phys*., vol. 95, p. 7501, 2004.

[32] K. Barmak, J. Kim, L. H. Lewis, K. R. Coffey, M. F. Toney, A. J. Kellock, and J.-U. Thiele, "On the relationship of magnetocrystalline anisotropy and stoichiometry in

epitaxial $L1_0$ CiPt (001) and FePt (001) thin films," *J. Appl. Phys.*, vol. 98, p. 033904, 2005.

[33] O. Hovorka, S. Devos, Q. Coopman, W. J. Fan, C. J. Aas, R. F. L. Evans, Xi Chen, G. Ju, and R. W. Chantrell, "The Curie temperature distribution of FePt granular magnetic recording media," *Appl. Phys. Lett.*, vol. 101, p. 052406, 2012.

[34] H. Li and J.-G. Zhu, "Understanding the impact of T_c and H_K variation on signal-to-noise ratio in heat-assisted magnetic recording," *J. Appl. Phys.*, vol. 115, p. 17B744, 2014.

[35] B. Terris, T. Thomson, and G. Hu, "Patterned media for future magnetic data storage," *Microsyst. Technol.*, vol. 13, p. 189, 2006.

[36] H. Ritchter, A. Lyberatos, U. Nowak, R. Evans, and R. Chantrell, "The thermodynamic limits of magnetic recording," *J. Appl. Phys.*, vol. 111, p. 033909 (2012).

[37] R. Evans, R. Chantrell, U. Nowak, A. Lyberatos, and H.-J. Richter, "Thermally induced error: Density limit for magnetic data storage," *Appl. Phys. Lett.*, vol. 100, p. 102402, 2012.

[38] F. West, "General Superparamagnetic Behavior of an Aligned Assembly of Uniaxially Anisotropic Particles," *J. Appl. Phys.*, vol. 32, p. S249, 1961.

[39] X. Wang, K. Gao, H. Zhou, A. Itagi, M. Seigler, and E. Gage, "HAMR Recording Limitations and Extendibility," *IEEE Trans. Magn.*, vol. 49, no. 2, pp. 686–692, Feb. 2013.

[40] W. A. Challener, C. Peng, A. V. Itagi, D. Karns, W. Peng, Y. Peng, X. Yang, X. Zhu, N. J. Gokemeijer, Y.-T. Hsia, G. Ju, R. E. Rottmayer, M. A. Seigler, and E. C. Gage, "Heat-assisted magnetic recording by a near-field transducer with efficient optical energy transfer," *Nature Photon.*, vol. 3, pp. 220–224, 2009.

[41] T. W. Ebbesen, H. J. Lezec, H. F. Ghaemi, T. Thio, and P. A. Wolff, "Extraordinary optical transmission through subwavelength hole arrays," *Nature*, vol. 391, pp. 667–669, 1998.

[42] R. Ikkawi, N. Amos, A. Lavrenov, A. Krichevsky, D. Teweldebrhan, S. Ghosh, A., A. Balandin, D. Litvinov, and S. Khizroev, "Near-Field Optical Transducer for Heat-Assisted Magnetic Recording for Beyond-10-Tbit/in^2 Densities," *J. Nanoelectron. Optoelectron.*, vol. 3, pp. 44–54, 2008.

[43] S. Ghai, W. Kim, C. Amon, and M. Jhon, "A novel heat transfer model and its application to information storage systems," *J. Appl. Phys.*, vol. 97, p. 10P703, 2005.

[44] A. Chernyshov, D. Treves, T. Le, F. Zong, A. Ajan, and R. Acharya, "Measurement of FePt thermal properties relevant to heat-assisted magnetic recording," *Appl. Phys.*, vol. 115, p. 17B735, 2014.

[45] H. Ho, A. Sharma, W.-L. Ong, J. Malen, J. Bain, and J.-G. Zhu, "Experimental estimates of in-plane thermal conductivity in FePt-C Granular thin film heat assisted magnetic recording media using a model layered system," *Appl. Phys. Lett.*, vol. 103, p. 131937, 2013.

[46] B. Xu, Z. Liu, R. Ji, Y. Toh, J. Hu, J. Li, J. Zhang, K. Ye, and C. Chia, “Thermal issues and their effects on heat-assisted magnetic recording system,” *J. Appl. Phys*., vol. 111, p. 07B701, 2012.

[47] J. Mallinson, “On extremely high density magnetic recording,” *IEEE Trans. Magn.*, vol. 10, no. 2, pp. 368–373, Jun. 1974.

[48] W. Xia, C. Xiao, and D. Shindo, “Changes of Magnetic Anisotropy of CoPtCr Perpendicular Films Due to Ru Intermediate Layer Under High Gas Pressure,” *IEEE Trans. Magn*., vol. 46, no. 10, pp. 3711–3714, Oct. 2010.

[49] B. Xu, J. Yang, H. Yuan, J. Zhang, Q. Zhang, and T. Chong, “Thermal Effects in Heat Assisted Bit Patterned Media Recording,” *IEEE Trans. Magn*. vol. 45, no. 5, pp. 2292–2295, May 2009.

[50] F. Akagi, M. Mukoh, M. Mochizuki, J. Ushiyama, T. Matsumoto, and H. Miyamoto, “Thermally assisted magnetic recording with bit-patterned media to achieve areal recording density beyond 5 Tb/in^2,” *J. Magn. Magn. Mater.*, vol 324, pp. 309–313, 2012.

[51] T. McDaniel, “Areal density limitation in bit-patterned, heat-assisted magnetic recording using FePtX media,” *J. Appl. Phys.*, vol. 112, p. 093920, 2012.

[52] A. Ghoreyshi and R. Victora, “Heat assisted magnetic recording with patterned FePt recording media using a lollipop near field transducer,” *J. Appl. Phys*., vol. 115, p. 17B719, 2014.

[53] (2013, Sep.) Seagate delivers on technology milestone: First to ship hard drives using next-generation shingled magnetic recording. [Online]. Available: http://www.seagate.com/

[54] S. Greaves, Y. Kanai, and H. Muraoka, "Shingled Thermally Assisted Magnetic Recording For 8 Tbit/in^2," *IEEE Trans. Magn*. (accepted in 2014).

[55] L. Landau and E. Lifshits, "On the Theory of the Dispersion of Magnetic Permeability in Ferromagnetic Bodies," *Phys. Zeitsch. Der Sow*., vol. 8, pp. 153–169, 1935. Reprinted in *Ukr. J. Phys*., vol. 53, Special Issue, 2008.

[56] W. F. Brown, *Micromagnetics*. New York: Interscience, 1963.

[57] R. C. O'Handley, *Modern Magnetic Materials: Principles and Applications.* New York: Wiley, 2000.

[58] J. Fidler, R. W. Chantrell, T. Schrefl, and M. Wongsam, "Micromagnetics I: Basic principles," *Encyclopedia of Materials: Science and Technology*, K. H. J. Buschow, R. W. Cahn, M. C. Flemings, B. Ilschner, E. J. Kramer, S. Mahajan (eds.), Elsevier, 2001, pp. 5642–5651.

[59] R. H. Victora, "Quantitative Theory for Hysterestic Phenomena in CoNi Magnetic Thin Films," *Phys. Rev. Lett*., vol. 27, no. 17, pp. 1788–1791, 1987.

[60] W. F. Brown, "Thermal Fluctuations of a Single-Domain Particle," *Phys. Rev.*, vol. 130, no. 5, pp. 1677–1686, 1963.

[61] D. Weller, A. Moser, L. Folks, M. E. Best, W. Lee, M.F. Toney, M. Schwickert, J.-U. Thiele, M. F. Doerner, "High K_u materials approach to 100 Gbits/in^2," *IEEE Trans. Magn*., vol. 36, no. 1, pp. 10–15, Feb. 2000.

[62] Y. Shimizu and H.N. Bertram, “Micromagnetic study of the transition parameter and position jitter in perpendicular recording,” *IEEE Trans. Magn*., vol. 39, no. 3, pp. 1846–1850, May 2003.

[63] P. Asselin, R. F. L. Evans, J. Barker, R. W. Chantrell, R. Yanes, O. Chubykalo-Fesenko, D. Hinzke, and U. Nowak, “Constrained Monte Carlo method and calculation of the temperature dependence of magnetic anisotropy,” *Phys. Rev. B*, vol. 82, p. 054415, 2010.

[64] Y. Nakatani, Y. Uesaka, and N.Hayashi, “Direct Solution of the Landau-Lifshitz-Gilbert Equation for Micromagnetics,” *Jpn. J. Appl. Phys*. vol. 28, p. 2485, 1989.

[65] R. S. de Biasi and T. C. Devezas, “Anisotropy field of small magnetic particles as measured by resonance,” *J. Appl. Phys.*, vol. 49, p. 2466, 1978.

[66] Y. Liu, D. Sellmyer, and D. Shindo, *Handbook of Advanced Magnetic Materials.* New York: Springer, 2005, vol. 1, p. 17.

[67] H. B. Callen and E. Callen, “The present status of the temperature dependence of magnetocrystalline anisotropy, and the $l(l+1)/2$ power law,” *J. Phys. Chem. Solids*, vol. 27, p. 1271, 1966.

[68] O. N. Mryasov, U. Nowak, K. Y. Guslienko, and R. R. Chantrell, “Temperature-dependent magnetic properties of FePt: Effective spin Hamiltonian model,” *Europhys. Lett*., vol. 69, no. 5, pp. 805–811, 2005.

[69] D. Hinzke, N. Kazantseva, U. Nowak, O. N. Mryasov, P. Asselin, and R. W. Chantrell, “Domain waoo properties of FePT: From Bloch to linear walls,” *Phys. Rev. B*, vol. 77, p. 094407, 2008.

[70] A. Seigler, W. A. Challener, E. Gage, N. Gokemeijer, G. Ju, B. Lu, K. Pelhos, C. Peng, R. E. Rottmayer, X. Yang, H. Zhou, and T. Rausch, "Intergrated heat assisted magnetic recording head: Design and recording demonstration," *IEEE Trans. Magn*., vol. 44, no. 1, pp. 119–124, Jan. 2008.

[71] T. W. McDaniel, "Ultimate limits to thermally assisted magnetic recording," *J. Phys.: Condens. Matter*, vol. 17, pp. R315–R332, 2005.

[72] X. Wang, K. Gao, and M. Seigler, "Magnetization switching variations and transition-width limit in heat-assisted magnetic recording," *IEEE Trans. Magn*., vol. 47, no. 10, pp. 2371–2374, Oct. 2011.

[73] A. F. Torabi, J. Van Ek, E. Champion, and J. Wang, "Micromagnetic modeling study of thermal gradient effect in heat-assisted magnetic recording (HAMR)," *IEEE Trans. Magn*., vol. 45, no. 10, pp. 3848–3850, Oct. 2009.

[74] S.-K. Ma, *Modern Theory of Critical Phenomena.* Reading, MA: Benjamin, 1976.

[75] P.-W. Huang, Xi. Chen, and R. H. Victora, "Time dependence of magnetic anisotropy at finite temperature for homogeneous and composite media," *IEEE Trans. Magn*., vol. 48, no. 11, pp. 3188–3191, Nov. 2012.

[76] X. Feng and P. B. Visscher, "Coarse-graining Landau-Lifshitz damping," *J. Appl. Phys*., vol. 89, pp. 6988–6990, 2001.

[77] A. Y. Dobin and R. H. Victora, "Intrinsic nonlinear ferromagnetic relaxation in thin metallic films," *Phys. Rev. Lett*., vol. 90, p. 167203, 2003.

[78] A. Y. Dobin and R. H. Victora, "Surface roughness induced extrinsic damping in thin magnetic films," *Phys. Rev. Lett*., vol. 92, p. 257204, 2004.

[79] R. Rottmayer, S. Batra, D. Buechel, W. A. Challener, J. Hohlfeld, Y. Kubota, L. Li, B. Liu, C. Mihalcea, K. Mountfield, K. Pelhos, C. Peng, T. Rausch, M. A. Seigler, D. Weller, and X. Yang, "Heat-assisted magnetic recording," *IEEE Trans. Magn.*, vol. 42, no. 10, pp. 2417–2421, Oct. 2006.

[80] B. Van de Wiele, F. Olyslager, L. Dupre, and D. De Zutter, "On the accuracy of FFT based magnetostatic field evaluation schemes in micromagnetic hysteresis modeling," J. Magn. Magn. Mater., vol. 322, pp. 469–476, 2010.

[81] Y. Dong and R. H. Victora, "Micromagnetic study of medium noise plateau," *IEEE Trans. Magn.*, vol. 45, no. 10, pp. 3714–3717, Oct. 2009.

[82] H. Sohn and R. H. Victora, "Recording comparison of ECC versus conventional media at equal grain size," *IEEE Trans. Magn.*, vol. 47, no. 10, pp. 4073–4076, Oct. 2011.

[83] J. Baker, R. F. L. Evans, R. W. Chantrell, D. Hinzke, and U. Nowak, "Atomistic spin model simulation of magnetic reversal modes near the Curie point," *Appl. Phys. Lett.*, vol. 97, p. 192504, 2010.

[84] S. Greaves, Y. Kanai, and H. Muraoka, "Magnetization switching in energy assisted recording," *IEEE Trans. Magn.*, vol. 48, no. 5, pp. 1794–1800, May 2012.

[85] M. Benakli, A. F. Torabi, M. L. Mallary, H. Zhou, and H. N. Bertram, "Micromagnetic study of switching speed in perpendicular recording media," *IEEE Trans. Magn.*, vol. 37, no. 4, pp. 1564–1566, Jul. 2001.

[86] Y. Wang and J.-G. Zhu, "Understanding field angle for heat assisted magnetic recording via dynamic modeling," *Appl. Phys. Lett.*, vol. 109, p. 07B706, 2011.

[87] A. Q. Wu, Y. Kubota, T. Klemmer, T. Rausch, C. Peng, Y. Peng, D. Karns, X. Zhu, Y. Ding, E. K. C. Chang, Y. Zhao, H. Zhou, K. Gao, J.-U. Thiele, M. Seigler, G. Ju, and E. Gage, "HAMR Areal Density Demonstration of 1+ Tbpsi on Spinstand," *IEEE Trans. Magn*., vol. 49, no. 2, pp. 779–782, Feb. 2013.

[88] R. H. Victora and P.-W. Huang, "Simulation of Heat Assisted Magnetic Recording Using Renormalized Media Cells," *IEEE Trans. Magn*., vol. 49, no. 2, pp. 751–757, Feb. 2013.

[89] J.-G. Zhu and H. Li, "Understanding Signal and Noise in Heat Assisted Magnetic Recording," *IEEE Trans. Magn*., vol. 49, no. 2, pp. 765–772, Feb. 2013.

[90] Q. Tao and R. H. Victora, private communication, 2013.

[91] E. Beaurepaire, J.-C. Merle, A. Daunois, and J.-Y. Bigot, "Ultrafast Spin Dynamics in Ferromagnetic Nickel," *Phys. Rev. Lett*., vol. 76, p. 4250, 1996.

[92] B. V. Budaev and D. B. Bogy, "On the lifetime of plasmonic transducers in heat assisted magnetic recording," *J. Appl. Phys*., vol. 112, p. 034512, 2012.

[93] N. Wang, K. Komvopoulos, F. Rose and B. Marchon, "Structural stability of hydrogenated amorphous carbon overcoats used in heat-assisted magnetic recording investigated by rapid thermal annealing," *J. Appl. Phys.*, vol. 113, p. 083517, 2013.

[94] H. J. Richter, A. Lyberatos, U. Nowak, R. F. L, Evans, and R. W. Chantrell, "The thermodynamic limits of magnetic recording," *J. Appl. Phys*., vol. 111, p. 033909, 2012.

[95] D. Suess and T. Schrefl, “Breaking the thermally induced write error in heat assisted recording by using low and high Tc materials,” *Appl. Phys. Lett.*, vol. 102, p. 162405, 2013.

[96] J. U. Thiele, S. Matt, and E. E. Fullerton, “FeRh/FePt exchange spring films for thermally assisted magnetic recording media,” *Appl. Phys. Lett.*, vol. 82, p. 2859, 2003.

[97] G. C. Han, J. J. Qiu, Q. J. Yap, P. Luo, D. E. Laughlin, J. G. Zhu, T. Kanbe and T. Shige, “Magnetic stability of ultrathin FeRh films,” *J. Appl. Phys.*, vol. 113, p. 17C107, 2013.

[98] D. Kande, S. Pisana, D. Weller, D. E. Laughlin, and J.-G. Zhu, “Enhanced B2 Ordering of FeRh Thin Films Using B2 NiAl Underlayers,” *IEEE Trans. Magn.*, vol. 47, no. 10, pp. 3296-3299, Oct. 2011.

[99] P.-W. Huang and R. H. Victora, “Heat assisted magnetic recording: Grain size dependency, enhanced damping, and a simulation/experiment comparison,” *J. Appl. Phys.*, vol. 115, p. 17B710, 2014.

[100] E Mancini, F. Pressacco, M. Haertinger, E. E. Fullerton, T. Suzuki, G. Woltersdorf and C. H. Back, “Magnetic phase transition in iron–rhodium thin films probed by ferromagnetic resonance,” *J. Phys. D: Appl. Phys.*, vol. 46, p. 245302, 2013.

[101] K. Uebayashi, H. Shimizu and H. Yamada, “Structure and Magnetism of Fe(Rh, Pd) Alloys,” *Mater. Trans.*, vol. 47, no. 3, pp. 456-459, Mar. 2006.

[102] A. Y. Dobin and H. J. Richter, “Domain wall assisted magnetic recording,” *Appl. Phys. Lett.*, vol. 89, p. 062512, 2006.

[103] D. Suess, T. Schrefl, and J. Fidler, “Reversal modes, thermal stability and exchange length in perpendicular recording media,” *IEEE Trans. Magn.*, vol. 37, no. 4, pp. 1664-1666, Jul. 2001.

[104] K.-Z. Gao and J. Fernandez-de-Castro, “Energy surface model and magnetization switching for exchange coupled magnetic particles,” *J. Appl. Phys.*, vol. 99, p. 08K503, 2006.

[105] B. Hillebrands and K. Ounadjela, Eds., *Spin Dynamics in Confined Magnetic Structures I, II and III*. New York: Springer-Verlag, 2001–2007.

[106] B. Valcu and N.-H. Yeh, “Jitter in a Voronoi Pattern Media-Effect of Grain Size Distribution and Reader Width,” *IEEE Trans. Magn.*, vol. 46, no. 6, pp. 2160-2162, June 2010.

APPENDIX

As shown in Fig. 2.1, there is a magnetic slab with dimensions $0 < x < L_x$, $0 < y < L_y$, and $-h/2 < z < h/2$, divided into $d \times d \times d$ cubic cells:

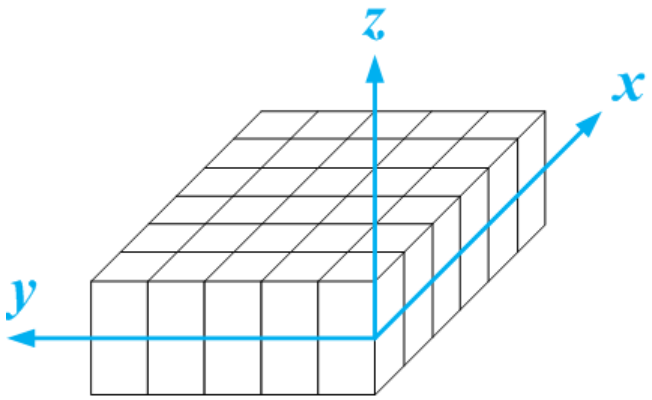

Figure 2.1: Schematic of the magnetic sample of rectangular shape for demagnetization field calculation.

As mentioned in Sec. 2.3, the magnetostatic field $\vec{H}_{\text{ms}}(\vec{r})$ is function of $\vec{M}(\vec{r}')$ and can be written as a general form

$$\vec{H}_{\text{ms}}(\vec{r}) = \sum_{\vec{r}';\, \vec{r}' \neq \vec{r}} \overleftrightarrow{G}(\vec{r} - \vec{r}') \cdot \vec{M}(\vec{r}') \tag{2.22}$$

where

$$\overleftrightarrow{G}(\vec{r} - \vec{r}') \equiv \begin{bmatrix} G^{xx}_{\vec{r}\vec{r}'} & G^{xy}_{\vec{r}\vec{r}'} & G^{xz}_{\vec{r}\vec{r}'} \\ G^{yx}_{\vec{r}\vec{r}'} & G^{yy}_{\vec{r}\vec{r}'} & G^{yz}_{\vec{r}\vec{r}'} \\ G^{zx}_{\vec{r}\vec{r}'} & G^{zy}_{\vec{r}\vec{r}'} & G^{zz}_{\vec{r}\vec{r}'} \end{bmatrix} \tag{2.23}$$

Notice that the self-contribution of each cell can be ignored ($\vec{r} \neq \vec{r}'$) in Eq. (2.22) as we use cubic discretized cells (a cubic magnet results in no shape anisotropy). If the cells are not cubic, the case $\vec{r} = \vec{r}'$ should be included. As mentioned in Sec. 2.3, the goal is to

transform Eq. (2.22) into Fourier space, in which the discrete convolution of G and M will turn into a direct product (see Eq. (2.24)).

Define the central coordinates of any two different cubes: $\vec{r} = (x, y, z)$, $\vec{r}' = (x', y', z')$. The coordinates (denoted (x'', y'', z'')) of the 6 surfaces ($l = 1, 2, \ldots, 6$) of the cube at $\vec{r}'$ are

$$
\begin{aligned}
l=1:&\ \left(x''=x'+\frac{d}{2},\ y'-\frac{d}{2}<\ y''<\ y'+\frac{d}{2},\ z'-\frac{d}{2}<\ z''<\ z'+\frac{d}{2}\right)\\
l=2:&\ \left(x''=x'-\frac{d}{2},\ y'-\frac{d}{2}<\ y''<\ y'+\frac{d}{2},\ z'-\frac{d}{2}<\ z''<\ z'+\frac{d}{2}\right)\\
l=3:&\ \left(x'-\frac{d}{2}<x''<x'+\frac{d}{2},\ y''=y'+\frac{d}{2},\ z'-\frac{d}{2}<\ z''<\ z'+\frac{d}{2}\right)\\
l=4:&\ \left(x'-\frac{d}{2}<x''<x'+\frac{d}{2},\ y''=y'-\frac{d}{2},\ z'-\frac{d}{2}<\ z''<\ z'+\frac{d}{2}\right)\\
l=5:&\ \left(x'-\frac{d}{2}<x''<x'+\frac{d}{2},\ y'-\frac{d}{2}<y''<y'+\frac{d}{2},\ z''=z'+\frac{d}{2}\right)\\
l=6:&\ \left(x'-\frac{d}{2}<x''<x'+\frac{d}{2},\ y'-\frac{d}{2}<y''<y'+\frac{d}{2},\ z''=z'-\frac{d}{2}\right),
\end{aligned}
\tag{A.1}
$$

and the surface charges on the surfaces are $\sigma_1(\vec{r}') = M_x(\vec{r}')$, $\sigma_2(\vec{r}') = -M_x(\vec{r}')$, $\sigma_3(\vec{r}') = M_y(\vec{r}')$, $\sigma_4(\vec{r}') = -M_y(\vec{r}')$, $\sigma_5(\vec{r}') = M_z(\vec{r}')$, $\sigma_6(\vec{r}') = -M_z(\vec{r}')$, where M_x, M_y, and M_z are the magnitudes of the directional components of the magnetization at $\vec{r}'$. Then Eq. (2.25) can rewritten as follows

$$l=1:\int_{z'-\frac{d}{2}}^{z'+\frac{d}{2}}\int_{y'-\frac{d}{2}}^{y'+\frac{d}{2}}\left(\sigma_1(\vec{r}')\right)\frac{\left[x-\left(x'+\frac{d}{2}\right)\right]\hat{x}+\left(y-y''\right)\hat{y}+\left(z-z''\right)\hat{z}}{\left\{\left[x-\left(x'+\frac{d}{2}\right)\right]^2+\left(y-y''\right)^2+\left(z-z''\right)^2\right\}^{\frac{3}{2}}}dy''dz''$$

$$l=2:\int_{z'-\frac{d}{2}}^{z'+\frac{d}{2}}\int_{y'-\frac{d}{2}}^{y'+\frac{d}{2}}\left(\sigma_2(\vec{r}')\right)\frac{\left[x-\left(x'-\frac{d}{2}\right)\right]\hat{x}+\left(y-y''\right)\hat{y}+\left(z-z''\right)\hat{z}}{\left\{\left[x-\left(x'-\frac{d}{2}\right)\right]^2+\left(y-y''\right)^2+\left(z-z''\right)^2\right\}^{\frac{3}{2}}}dy''dz''$$

$$l=3:\int_{z'-\frac{d}{2}}^{z'+\frac{d}{2}}\int_{x'-\frac{d}{2}}^{x'+\frac{d}{2}}\left(\sigma_3(\vec{r}')\right)\frac{\left(x-x''\right)\hat{x}+\left[y-\left(y'+\frac{d}{2}\right)\right]\hat{y}+\left(z-z''\right)\hat{z}}{\left\{\left(x-x''\right)^2+\left[y-\left(y'+\frac{d}{2}\right)\right]^2+\left(z-z''\right)^2\right\}^{\frac{3}{2}}}dx''dz''$$

$$l=4:\int_{z'-\frac{d}{2}}^{z'+\frac{d}{2}}\int_{x'-\frac{d}{2}}^{x'+\frac{d}{2}}\left(\sigma_4(\vec{r}')\right)\frac{\left(x-x''\right)\hat{x}+\left[y-\left(y'-\frac{d}{2}\right)\right]\hat{y}+\left(z-z''\right)\hat{z}}{\left\{\left(x-x''\right)^2+\left[y-\left(y'-\frac{d}{2}\right)\right]^2+\left(z-z''\right)^2\right\}^{\frac{3}{2}}}dx''dz''$$

$$l=5:\int_{y'-\frac{d}{2}}^{y'+\frac{d}{2}}\int_{x'-\frac{d}{2}}^{x'+\frac{d}{2}}\left(\sigma_5(\vec{r}')\right)\frac{\left(x-x''\right)\hat{x}+\left(y-y''\right)\hat{y}+\left[z-\left(z'+\frac{d}{2}\right)\right]\hat{z}}{\left\{\left(x-x''\right)^2+\left(y-y''\right)^2+\left[z-\left(z'+\frac{d}{2}\right)\right]^2\right\}^{\frac{3}{2}}}dx''dy''$$

$$l=6:\int_{y'-\frac{d}{2}}^{y'+\frac{d}{2}}\int_{x'-\frac{d}{2}}^{x'+\frac{d}{2}}\left(\sigma_6(\vec{r}')\right)\frac{\left(x-x''\right)\hat{x}+\left(y-y''\right)\hat{y}+\left[z-\left(z'-\frac{d}{2}\right)\right]\hat{z}}{\left\{\left(x-x''\right)^2+\left(y-y''\right)^2+\left[z-\left(z'-\frac{d}{2}\right)\right]^2\right\}^{\frac{3}{2}}}dx''dy''\quad.\qquad(A.2)$$

We can rewrite Eq. (2.22) and the 9 entries of Eq. (2.23) now read

$$G_{xx}(\vec{r}-\vec{r}') = (M_s)\left[\int_{z'-\frac{d}{2}}^{z'+\frac{d}{2}}\int_{y'-\frac{d}{2}}^{y'+\frac{d}{2}} \frac{\left[x-\left(x'+\frac{d}{2}\right)\right]}{\left\{\left[x-\left(x'+\frac{d}{2}\right)\right]^2+(y-y'')^2+(z-z'')^2\right\}^{\frac{3}{2}}}\,dy''dz'' - \int_{z'-\frac{d}{2}}^{z'+\frac{d}{2}}\int_{y'-\frac{d}{2}}^{y'+\frac{d}{2}} \frac{\left[x-\left(x'-\frac{d}{2}\right)\right]}{\left\{\left[x-\left(x'-\frac{d}{2}\right)\right]^2+(y-y'')^2+(z-z'')^2\right\}^{\frac{3}{2}}}\,dy''dz''\right]$$

$$G_{xy}(\vec{r}-\vec{r}') = (M_s)\left[\int_{z'-\frac{d}{2}}^{z'+\frac{d}{2}}\int_{x'-\frac{d}{2}}^{x'+\frac{d}{2}} \frac{(x-x'')}{\left\{(x-x'')^2+\left[y-\left(y'+\frac{d}{2}\right)\right]^2+(z-z'')^2\right\}^{\frac{3}{2}}}\,dx''dz'' - \int_{z'-\frac{d}{2}}^{z'+\frac{d}{2}}\int_{x'-\frac{d}{2}}^{x'+\frac{d}{2}} \frac{(x-x'')}{\left\{(x-x'')^2+\left[y-\left(y'-\frac{d}{2}\right)\right]^2+(z-z'')^2\right\}^{\frac{3}{2}}}\,dx''dz''\right]$$

$$G_{xz}(\vec{r}-\vec{r}') = (M_s)\left[\int_{y'-\frac{d}{2}}^{y'+\frac{d}{2}}\int_{x'-\frac{d}{2}}^{x'+\frac{d}{2}} \frac{(x-x'')}{\left\{(x-x'')^2+(y-y'')^2+\left[z-\left(z'+\frac{d}{2}\right)\right]^2\right\}^{\frac{3}{2}}}\,dx''dy'' - \int_{y'-\frac{d}{2}}^{y'+\frac{d}{2}}\int_{x'-\frac{d}{2}}^{x'+\frac{d}{2}} \frac{(x-x'')}{\left\{(x-x'')^2+(y-y'')^2+\left[z-\left(z'-\frac{d}{2}\right)\right]^2\right\}^{\frac{3}{2}}}\,dx''dy''\right]$$

$$G_{yx}(\vec{r}-\vec{r}') = (M_s)\left[\begin{array}{l}\displaystyle\int_{z'-\frac{d}{2}}^{z'+\frac{d}{2}}\int_{y'-\frac{d}{2}}^{y'+\frac{d}{2}} \frac{y-y''}{\left\{\left[x-\left(x'+\frac{d}{2}\right)\right]^2+(y-y'')^2+(z-z'')^2\right\}^{\frac{3}{2}}}\,dy''dz'' - \\ \displaystyle\int_{z'-\frac{d}{2}}^{z'+\frac{d}{2}}\int_{y'-\frac{d}{2}}^{y'+\frac{d}{2}} \frac{y-y''}{\left\{\left[x-\left(x'-\frac{d}{2}\right)\right]^2+(y-y'')^2+(z-z'')^2\right\}^{\frac{3}{2}}}\,dy''dz''\end{array}\right]$$

$$G_{yy}(\vec{r}-\vec{r}') = (M_s)\left[\begin{array}{l}\displaystyle\int_{z'-\frac{d}{2}}^{z'+\frac{d}{2}}\int_{x'-\frac{d}{2}}^{x'+\frac{d}{2}} \frac{y-\left(y'+\frac{d}{2}\right)}{\left\{(x-x'')^2+\left[y-\left(y'+\frac{d}{2}\right)\right]^2+(z-z'')^2\right\}^{\frac{3}{2}}}\,dx''dz'' - \\ \displaystyle\int_{z'-\frac{d}{2}}^{z'+\frac{d}{2}}\int_{x'-\frac{d}{2}}^{x'+\frac{d}{2}} \frac{y-\left(y'-\frac{d}{2}\right)}{\left\{(x-x'')^2+\left[y-\left(y'-\frac{d}{2}\right)\right]^2+(z-z'')^2\right\}^{\frac{3}{2}}}\,dx''dz''\end{array}\right]$$

$$G_{yz}(\vec{r}-\vec{r}') = (M_s)\left[\begin{array}{l}\displaystyle\int_{y'-\frac{d}{2}}^{y'+\frac{d}{2}}\int_{x'-\frac{d}{2}}^{x'+\frac{d}{2}} \frac{y-y''}{\left\{(x-x'')^2+(y-y'')^2+\left[z-\left(z'+\frac{d}{2}\right)\right]^2\right\}^{\frac{3}{2}}}\,dx''dy'' - \\ \displaystyle\int_{y'-\frac{d}{2}}^{y'+\frac{d}{2}}\int_{x'-\frac{d}{2}}^{x'+\frac{d}{2}} \frac{y-y''}{\left\{(x-x'')^2+(y-y'')^2+\left[z-\left(z'-\frac{d}{2}\right)\right]^2\right\}^{\frac{3}{2}}}\,dx''dy''\end{array}\right]$$

$$G_{zx}(\vec{r}-\vec{r}') = (M_s)\left[\int_{z'-\frac{d}{2}}^{z'+\frac{d}{2}}\int_{y'-\frac{d}{2}}^{y'+\frac{d}{2}} \frac{z-z''}{\left\{\left[x-\left(x'+\frac{d}{2}\right)\right]^2+(y-y'')^2+(z-z'')^2\right\}^{\frac{3}{2}}}\,dy''dz'' - \int_{z'-\frac{d}{2}}^{z'+\frac{d}{2}}\int_{y'-\frac{d}{2}}^{y'+\frac{d}{2}} \frac{z-z''}{\left\{\left[x-\left(x'-\frac{d}{2}\right)\right]^2+(y-y'')^2+(z-z'')^2\right\}^{\frac{3}{2}}}\,dy''dz''\right]$$

$$G_{zy}(\vec{r}-\vec{r}') = (M_s)\left[\int_{z'-\frac{d}{2}}^{z'+\frac{d}{2}}\int_{x'-\frac{d}{2}}^{x'+\frac{d}{2}} \frac{z-z''}{\left\{(x-x'')^2+\left[y-\left(y'+\frac{d}{2}\right)\right]^2+(z-z'')^2\right\}^{\frac{3}{2}}}\,dx''dz'' - \int_{z'-\frac{d}{2}}^{z'+\frac{d}{2}}\int_{x'-\frac{d}{2}}^{x'+\frac{d}{2}} \frac{z-z''}{\left\{(x-x'')^2+\left[y-\left(y'-\frac{d}{2}\right)\right]^2+(z-z'')^2\right\}^{\frac{3}{2}}}\,dx''dz''\right]$$

$$G_{zz}(\vec{r}-\vec{r}') = (M_s)\left[\int_{y'-\frac{d}{2}}^{y'+\frac{d}{2}}\int_{x'-\frac{d}{2}}^{x'+\frac{d}{2}} \frac{z-\left(z'+\frac{d}{2}\right)}{\left\{(x-x'')^2+(y-y'')^2+\left[z-\left(z'+\frac{d}{2}\right)\right]^2\right\}^{\frac{3}{2}}}\,dx''dy'' - \int_{y'-\frac{d}{2}}^{y'+\frac{d}{2}}\int_{x'-\frac{d}{2}}^{x'+\frac{d}{2}} \frac{z-\left(z'-\frac{d}{2}\right)}{\left\{(x-x'')^2+(y-y'')^2+\left[z-\left(z'-\frac{d}{2}\right)\right]^2\right\}^{\frac{3}{2}}}\,dx''dy''\right]. \quad (A.3)$$

The integrals in Eq. (*A*.3) are all analytical, and Eq. (*A*.3) is further simplified as

$$\frac{G_{xx}(\vec{r}-\vec{r}')}{M_s} =$$

$$\left(\left\{\tan^{-1}\left[\frac{\left[y-\left(y'+\frac{d}{2}\right)\right]\left[z-\left(z'+\frac{d}{2}\right)\right]}{\alpha_{xx'}\sqrt{\alpha_{xx'}{}^2+\left[y-\left(y'+\frac{d}{2}\right)\right]^2+\left[z-\left(z'+\frac{d}{2}\right)\right]^2}}\right]+\tan^{-1}\left[\frac{\left[y-\left(y'-\frac{d}{2}\right)\right]\left[z-\left(z'-\frac{d}{2}\right)\right]}{\alpha_{xx'}\sqrt{\alpha_{xx'}{}^2+\left[y-\left(y'-\frac{d}{2}\right)\right]^2+\left[z-\left(z'-\frac{d}{2}\right)\right]^2}}\right]\right\}-\right.$$

$$\left.\left\{\tan^{-1}\left[\frac{\left[y-\left(y'+\frac{d}{2}\right)\right]\left[z-\left(z'-\frac{d}{2}\right)\right]}{\alpha_{xx'}\sqrt{\alpha_{xx'}{}^2+\left[y-\left(y'+\frac{d}{2}\right)\right]^2+\left[z-\left(z'-\frac{d}{2}\right)\right]^2}}\right]+\tan^{-1}\left[\frac{\left[y-\left(y'-\frac{d}{2}\right)\right]\left[z-\left(z'+\frac{d}{2}\right)\right]}{\alpha_{xx'}\sqrt{\alpha_{xx'}{}^2+\left[y-\left(y'-\frac{d}{2}\right)\right]^2+\left[z-\left(z'+\frac{d}{2}\right)\right]^2}}\right]\right\}\right)-$$

$$\left(\left\{\tan^{-1}\left[\frac{\left[y-\left(y'+\frac{d}{2}\right)\right]\left[z-\left(z'+\frac{d}{2}\right)\right]}{\beta_{xx'}\sqrt{\beta_{xx'}{}^2+\left[y-\left(y'+\frac{d}{2}\right)\right]^2+\left[z-\left(z'+\frac{d}{2}\right)\right]^2}}\right]+\tan^{-1}\left[\frac{\left[y-\left(y'-\frac{d}{2}\right)\right]\left[z-\left(z'-\frac{d}{2}\right)\right]}{\beta_{xx'}\sqrt{\beta_{xx'}{}^2+\left[y-\left(y'-\frac{d}{2}\right)\right]^2+\left[z-\left(z'-\frac{d}{2}\right)\right]^2}}\right]\right\}-\right.$$

$$\left.\left\{\tan^{-1}\left[\frac{\left[y-\left(y'+\frac{d}{2}\right)\right]\left[z-\left(z'-\frac{d}{2}\right)\right]}{\beta_{xx'}\sqrt{\beta_{xx'}{}^2+\left[y-\left(y'+\frac{d}{2}\right)\right]^2+\left[z-\left(z'-\frac{d}{2}\right)\right]^2}}\right]+\tan^{-1}\left[\frac{\left[y-\left(y'-\frac{d}{2}\right)\right]\left[z-\left(z'+\frac{d}{2}\right)\right]}{\beta_{xx'}\sqrt{\beta_{xx'}{}^2+\left[y-\left(y'-\frac{d}{2}\right)\right]^2+\left[z-\left(z'+\frac{d}{2}\right)\right]^2}}\right]\right\}\right)$$

where

$$\alpha_{xx'} = \left[x-\left(x'+\frac{d}{2}\right)\right]$$

$$\beta_{xx'} = \left[x-\left(x'-\frac{d}{2}\right)\right]$$

(*A*.4)

$$\frac{G_{xy}(\vec{r}-\vec{r}')}{M_s} =$$

$$\left\{ \ln\left\{ \frac{4\left[-\left[z-\left(z'+\frac{d}{2}\right)\right]+\sqrt{\left[x-\left(x'+\frac{d}{2}\right)\right]^2+\alpha_{yy'}{}^2+\left[z-\left(z'+\frac{d}{2}\right)\right]^2}\right]}{\left[-\left[z-\left(z'-\frac{d}{2}\right)\right]+\sqrt{\left[x-\left(x'-\frac{d}{2}\right)\right]^2+\alpha_{yy'}{}^2+\left[z-\left(z'-\frac{d}{2}\right)\right]^2}\right]} \right\} - \right.$$

$$\left. \ln\left\{ \frac{4\left[-\left[z-\left(z'+\frac{d}{2}\right)\right]+\sqrt{\left[x-\left(x'-\frac{d}{2}\right)\right]^2+\alpha_{yy'}{}^2+\left[z-\left(z'+\frac{d}{2}\right)\right]^2}\right]}{\left[-\left[z-\left(z'-\frac{d}{2}\right)\right]+\sqrt{\left[x-\left(x'+\frac{d}{2}\right)\right]^2+\alpha_{yy'}{}^2+\left[z-\left(z'-\frac{d}{2}\right)\right]^2}\right]} \right\} \right\} -$$

$$\left\{ \ln\left\{ \frac{4\left[-\left[z-\left(z'+\frac{d}{2}\right)\right]+\sqrt{\left[x-\left(x'+\frac{d}{2}\right)\right]^2+\beta_{yy'}{}^2+\left[z-\left(z'+\frac{d}{2}\right)\right]^2}\right]}{\left[-\left[z-\left(z'-\frac{d}{2}\right)\right]+\sqrt{\left[x-\left(x'-\frac{d}{2}\right)\right]^2+\beta_{yy'}{}^2+\left[z-\left(z'-\frac{d}{2}\right)\right]^2}\right]} \right\} - \right.$$

$$\left. \ln\left\{ \frac{4\left[-\left[z-\left(z'+\frac{d}{2}\right)\right]+\sqrt{\left[x-\left(x'-\frac{d}{2}\right)\right]^2+\beta_{yy'}{}^2+\left[z-\left(z'+\frac{d}{2}\right)\right]^2}\right]}{\left[-\left[z-\left(z'-\frac{d}{2}\right)\right]+\sqrt{\left[x-\left(x'+\frac{d}{2}\right)\right]^2+\beta_{yy'}{}^2+\left[z-\left(z'-\frac{d}{2}\right)\right]^2}\right]} \right\} \right\}$$

where

$$\alpha_{yy'} = \left[y-\left(y'+\frac{d}{2}\right)\right]$$

$$\beta_{yy'} = \left[y-\left(y'-\frac{d}{2}\right)\right]$$

(*A*.5)

$$\frac{G_{xz}(\vec{r}-\vec{r}')}{M_s} =$$

$$\left\{ \ln\left\{ \frac{4\left[-\left[y-\left(y'+\frac{d}{2}\right)\right]+\sqrt{\left[x-\left(x'+\frac{d}{2}\right)\right]^2+\left[y-\left(y'+\frac{d}{2}\right)\right]^2+\alpha_{zz'}{}^2}\right]}{\left[-\left[y-\left(y'-\frac{d}{2}\right)\right]+\sqrt{\left[x-\left(x'-\frac{d}{2}\right)\right]^2+\left[y-\left(y'-\frac{d}{2}\right)\right]^2+\alpha_{zz'}{}^2}\right]} \right\} - \right.$$

$$\left. \ln\left\{ \frac{4\left[-\left[y-\left(y'+\frac{d}{2}\right)\right]+\sqrt{\left[x-\left(x'-\frac{d}{2}\right)\right]^2+\left[y-\left(y'+\frac{d}{2}\right)\right]^2+\alpha_{zz'}{}^2}\right]}{\left[-\left[y-\left(y'-\frac{d}{2}\right)\right]+\sqrt{\left[x-\left(x'+\frac{d}{2}\right)\right]^2+\left[y-\left(y'-\frac{d}{2}\right)\right]^2+\alpha_{zz'}{}^2}\right]} \right\} \right\} -$$

$$\left\{ \ln\left\{ \frac{4\left[-\left[y-\left(y'+\frac{d}{2}\right)\right]+\sqrt{\left[x-\left(x'+\frac{d}{2}\right)\right]^2+\left[y-\left(y'+\frac{d}{2}\right)\right]^2+\beta_{zz'}{}^2}\right]}{\left[-\left[y-\left(y'-\frac{d}{2}\right)\right]+\sqrt{\left[x-\left(x'-\frac{d}{2}\right)\right]^2+\left[y-\left(y'-\frac{d}{2}\right)\right]^2+\beta_{zz'}{}^2}\right]} \right\} - \right.$$

$$\left. \ln\left\{ \frac{4\left[-\left[y-\left(y'+\frac{d}{2}\right)\right]+\sqrt{\left[x-\left(x'-\frac{d}{2}\right)\right]^2+\left[y-\left(y'+\frac{d}{2}\right)\right]^2+\beta_{zz'}{}^2}\right]}{\left[-\left[y-\left(y'-\frac{d}{2}\right)\right]+\sqrt{\left[x-\left(x'+\frac{d}{2}\right)\right]^2+\left[y-\left(y'-\frac{d}{2}\right)\right]^2+\beta_{zz'}{}^2}\right]} \right\} \right\}$$

where

$$\alpha_{zz'} = \left[z-\left(z'+\frac{d}{2}\right)\right]$$

$$\beta_{zz'} = \left[z-\left(z'-\frac{d}{2}\right)\right]$$

(*A*.6)

$$\frac{G_{yx}(\vec{r}-\vec{r}')}{M_s} =$$

$$\left\{ \ln\left\{ \frac{4\left[-\left[z-\left(z'+\frac{d}{2}\right)\right]+\sqrt{\alpha_{xx'}{}^2+\left[y-\left(y'+\frac{d}{2}\right)\right]^2+\left[z-\left(z'+\frac{d}{2}\right)\right]^2}\right]}{\left[-\left[z-\left(z'-\frac{d}{2}\right)\right]+\sqrt{\alpha_{xx'}{}^2+\left[y-\left(y'-\frac{d}{2}\right)\right]^2+\left[z-\left(z'-\frac{d}{2}\right)\right]^2}\right]} \right\} - \right.$$

$$\left. \ln\left\{ \frac{4\left[-\left[z-\left(z'+\frac{d}{2}\right)\right]+\sqrt{\alpha_{xx'}{}^2+\left[y-\left(y'-\frac{d}{2}\right)\right]^2+\left[z-\left(z'+\frac{d}{2}\right)\right]^2}\right]}{\left[-\left[z-\left(z'-\frac{d}{2}\right)\right]+\sqrt{\alpha_{xx'}{}^2+\left[y-\left(y'+\frac{d}{2}\right)\right]^2+\left[z-\left(z'-\frac{d}{2}\right)\right]^2}\right]} \right\} \right\} -$$

$$\left\{ \ln\left\{ \frac{4\left[-\left[z-\left(z'+\frac{d}{2}\right)\right]+\sqrt{\beta_{xx'}{}^2+\left[y-\left(y'+\frac{d}{2}\right)\right]^2+\left[z-\left(z'+\frac{d}{2}\right)\right]^2}\right]}{\left[-\left[z-\left(z'-\frac{d}{2}\right)\right]+\sqrt{\beta_{xx'}{}^2+\left[y-\left(y'-\frac{d}{2}\right)\right]^2+\left[z-\left(z'-\frac{d}{2}\right)\right]^2}\right]} \right\} - \right.$$

$$\left. \ln\left\{ \frac{4\left[-\left[z-\left(z'+\frac{d}{2}\right)\right]+\sqrt{\beta_{xx'}{}^2+\left[y-\left(y'-\frac{d}{2}\right)\right]^2+\left[z-\left(z'+\frac{d}{2}\right)\right]^2}\right]}{\left[-\left[z-\left(z'-\frac{d}{2}\right)\right]+\sqrt{\beta_{xx'}{}^2+\left[y-\left(y'+\frac{d}{2}\right)\right]^2+\left[z-\left(z'-\frac{d}{2}\right)\right]^2}\right]} \right\} \right\}$$

where

$$\alpha_{xx'} = \left[x-\left(x'+\frac{d}{2}\right)\right]$$

$$\beta_{xx'} = \left[x-\left(x'-\frac{d}{2}\right)\right]$$

(*A*.7)

$$\frac{G_{yy}(\vec{r}-\vec{r}')}{M_s} =$$

$$\left(\left\{\tan^{-1}\left[\frac{\left[x-\left(x'+\frac{d}{2}\right)\right]\left[z-\left(z'+\frac{d}{2}\right)\right]}{\alpha_{yy'}\sqrt{\left[x-\left(x'+\frac{d}{2}\right)\right]^2+\alpha_{yy'}{}^2+\left[z-\left(z'+\frac{d}{2}\right)\right]^2}}\right]+\tan^{-1}\left[\frac{\left[x-\left(x'-\frac{d}{2}\right)\right]\left[z-\left(z'-\frac{d}{2}\right)\right]}{\alpha_{yy'}\sqrt{\left[x-\left(x'-\frac{d}{2}\right)\right]^2+\alpha_{yy'}{}^2+\left[z-\left(z'-\frac{d}{2}\right)\right]^2}}\right]\right\}-\right.$$

$$\left.\left\{\tan^{-1}\left[\frac{\left[x-\left(x'+\frac{d}{2}\right)\right]\left[z-\left(z'-\frac{d}{2}\right)\right]}{\alpha_{yy'}\sqrt{\left[x-\left(x'+\frac{d}{2}\right)\right]^2+\alpha_{yy'}{}^2+\left[z-\left(z'-\frac{d}{2}\right)\right]^2}}\right]+\tan^{-1}\left[\frac{\left[x-\left(x'-\frac{d}{2}\right)\right]\left[z-\left(z'+\frac{d}{2}\right)\right]}{\alpha_{yy'}\sqrt{\left[x-\left(x'-\frac{d}{2}\right)\right]^2+\alpha_{yy'}{}^2+\left[z-\left(z'+\frac{d}{2}\right)\right]^2}}\right]\right\}\right)-$$

$$\left(\left\{\tan^{-1}\left[\frac{\left[x-\left(x'+\frac{d}{2}\right)\right]\left[z-\left(z'+\frac{d}{2}\right)\right]}{\beta_{yy'}\sqrt{\left[x-\left(x'+\frac{d}{2}\right)\right]^2+\beta_{yy'}{}^2+\left[z-\left(z'+\frac{d}{2}\right)\right]^2}}\right]+\tan^{-1}\left[\frac{\left[x-\left(x'-\frac{d}{2}\right)\right]\left[z-\left(z'-\frac{d}{2}\right)\right]}{\beta_{yy'}\sqrt{\left[x-\left(x'-\frac{d}{2}\right)\right]^2+\beta_{yy'}{}^2+\left[z-\left(z'-\frac{d}{2}\right)\right]^2}}\right]\right\}-\right.$$

$$\left.\left\{\tan^{-1}\left[\frac{\left[x-\left(x'+\frac{d}{2}\right)\right]\left[z-\left(z'-\frac{d}{2}\right)\right]}{\beta_{yy'}\sqrt{\left[x-\left(x'+\frac{d}{2}\right)\right]^2+\beta_{yy'}{}^2+\left[z-\left(z'-\frac{d}{2}\right)\right]^2}}\right]+\tan^{-1}\left[\frac{\left[x-\left(x'-\frac{d}{2}\right)\right]\left[z-\left(z'+\frac{d}{2}\right)\right]}{\beta_{yy'}\sqrt{\left[x-\left(x'-\frac{d}{2}\right)\right]^2+\beta_{yy'}{}^2+\left[z-\left(z'+\frac{d}{2}\right)\right]^2}}\right]\right\}\right)$$

where

$$\alpha_{yy'} = \left[y-\left(y'+\frac{d}{2}\right)\right]$$

$$\beta_{yy'} = \left[y-\left(y'-\frac{d}{2}\right)\right]$$

(*A*.8)

$$\frac{G_{yz}(\vec{r}-\vec{r}')}{M_s} =$$

$$\left\{ \ln\left\{ \frac{4\left[-\left[x-\left(x'+\frac{d}{2} \right) \right] + \sqrt{\left[x-\left(x'+\frac{d}{2} \right) \right]^2 + \left[y-\left(y'+\frac{d}{2} \right) \right]^2 + \alpha_{zz'}{}^2} \right]}{\left[-\left[x-\left(x'-\frac{d}{2} \right) \right] + \sqrt{\left[x-\left(x'-\frac{d}{2} \right) \right]^2 + \left[y-\left(y'-\frac{d}{2} \right) \right]^2 + \alpha_{zz'}{}^2} \right]} \right\} - \right.$$

$$\ln\left\{ \frac{4\left[-\left[x-\left(x'+\frac{d}{2} \right) \right] + \sqrt{\left[x-\left(x'+\frac{d}{2} \right) \right]^2 + \left[y-\left(y'-\frac{d}{2} \right) \right]^2 + \alpha_{zz'}{}^2} \right]}{\left[-\left[x-\left(x'-\frac{d}{2} \right) \right] + \sqrt{\left[x-\left(x'-\frac{d}{2} \right) \right]^2 + \left[y-\left(y'+\frac{d}{2} \right) \right]^2 + \alpha_{zz'}{}^2} \right]} \right\} \Bigg\} -$$

$$\left\{ \ln\left\{ \frac{4\left[-\left[x-\left(x'+\frac{d}{2} \right) \right] + \sqrt{\left[x-\left(x'+\frac{d}{2} \right) \right]^2 + \left[y-\left(y'+\frac{d}{2} \right) \right]^2 + \beta_{zz'}{}^2} \right]}{\left[-\left[x-\left(x'-\frac{d}{2} \right) \right] + \sqrt{\left[x-\left(x'-\frac{d}{2} \right) \right]^2 + \left[y-\left(y'-\frac{d}{2} \right) \right]^2 + \beta_{zz'}{}^2} \right]} \right\} - \right.$$

$$\ln\left\{ \frac{4\left[-\left[x-\left(x'+\frac{d}{2} \right) \right] + \sqrt{\left[x-\left(x'+\frac{d}{2} \right) \right]^2 + \left[y-\left(y'-\frac{d}{2} \right) \right]^2 + \beta_{zz'}{}^2} \right]}{\left[-\left[x-\left(x'-\frac{d}{2} \right) \right] + \sqrt{\left[x-\left(x'-\frac{d}{2} \right) \right]^2 + \left[y-\left(y'+\frac{d}{2} \right) \right]^2 + \beta_{zz'}{}^2} \right]} \right\} \Bigg\}$$

where

$$\alpha_{zz'} = \left[z-\left(z'+\frac{d}{2} \right) \right]$$

$$\beta_{zz'} = \left[z-\left(z'-\frac{d}{2} \right) \right]$$

(*A*.9)

$$\frac{G_{zx}(\vec{r}-\vec{r}')}{M_s} =$$

$$\left\{ \ln\left\{ \frac{4\left[-\left[y-\left(y'+\frac{d}{2}\right)\right]+\sqrt{\alpha_{xx'}{}^2+\left[y-\left(y'+\frac{d}{2}\right)\right]^2+\left[z-\left(z'+\frac{d}{2}\right)\right]^2}\right]}{\left[-\left[y-\left(y'-\frac{d}{2}\right)\right]+\sqrt{\alpha_{xx'}{}^2+\left[y-\left(y'-\frac{d}{2}\right)\right]^2+\left[z-\left(z'-\frac{d}{2}\right)\right]^2}\right]} \right\} - \right.$$

$$\left. \ln\left\{ \frac{4\left[-\left[y-\left(y'+\frac{d}{2}\right)\right]+\sqrt{\alpha_{xx'}{}^2+\left[y-\left(y'+\frac{d}{2}\right)\right]^2+\left[z-\left(z'-\frac{d}{2}\right)\right]^2}\right]}{\left[-\left[y-\left(y'-\frac{d}{2}\right)\right]+\sqrt{\alpha_{xx'}{}^2+\left[y-\left(y'-\frac{d}{2}\right)\right]^2+\left[z-\left(z'+\frac{d}{2}\right)\right]^2}\right]} \right\} \right\} -$$

$$\left\{ \ln\left\{ \frac{4\left[-\left[y-\left(y'+\frac{d}{2}\right)\right]+\sqrt{\beta_{xx'}{}^2+\left[y-\left(y'+\frac{d}{2}\right)\right]^2+\left[z-\left(z'+\frac{d}{2}\right)\right]^2}\right]}{\left[-\left[y-\left(y'-\frac{d}{2}\right)\right]+\sqrt{\beta_{xx'}{}^2+\left[y-\left(y'-\frac{d}{2}\right)\right]^2+\left[z-\left(z'-\frac{d}{2}\right)\right]^2}\right]} \right\} - \right.$$

$$\left. \ln\left\{ \frac{4\left[-\left[y-\left(y'+\frac{d}{2}\right)\right]+\sqrt{\beta_{xx'}{}^2+\left[y-\left(y'+\frac{d}{2}\right)\right]^2+\left[z-\left(z'-\frac{d}{2}\right)\right]^2}\right]}{\left[-\left[y-\left(y'-\frac{d}{2}\right)\right]+\sqrt{\beta_{xx'}{}^2+\left[y-\left(y'-\frac{d}{2}\right)\right]^2+\left[z-\left(z'+\frac{d}{2}\right)\right]^2}\right]} \right\} \right\}$$

where

$$\alpha_{xx'} = \left[x-\left(x'+\frac{d}{2}\right)\right]$$

$$\beta_{xx'} = \left[x-\left(x'-\frac{d}{2}\right)\right]$$

(*A*.10)

$$\frac{G_{zy}(\vec{r}-\vec{r}')}{M_s} =$$

$$\left\{ \ln\left\{ \frac{4\left[-\left[x-\left(x'+\frac{d}{2}\right)\right]+\sqrt{\left[x-\left(x'+\frac{d}{2}\right)\right]^2+\alpha_{yy'}{}^2+\left[z-\left(z'+\frac{d}{2}\right)\right]^2}\right]}{\left[-\left[x-\left(x'-\frac{d}{2}\right)\right]+\sqrt{\left[x-\left(x'-\frac{d}{2}\right)\right]^2+\alpha_{yy'}{}^2+\left[z-\left(z'-\frac{d}{2}\right)\right]^2}\right]} \right\} - \right.$$

$$\left. \ln\left\{ \frac{4\left[-\left[x-\left(x'+\frac{d}{2}\right)\right]+\sqrt{\left[x-\left(x'+\frac{d}{2}\right)\right]^2+\alpha_{yy'}{}^2+\left[z-\left(z'-\frac{d}{2}\right)\right]^2}\right]}{\left[-\left[x-\left(x'-\frac{d}{2}\right)\right]+\sqrt{\left[x-\left(x'-\frac{d}{2}\right)\right]^2+\alpha_{yy'}{}^2+\left[z-\left(z'+\frac{d}{2}\right)\right]^2}\right]} \right\} \right\} -$$

$$\left\{ \ln\left\{ \frac{4\left[-\left[x-\left(x'+\frac{d}{2}\right)\right]+\sqrt{\left[x-\left(x'+\frac{d}{2}\right)\right]^2+\beta_{yy'}{}^2+\left[z-\left(z'+\frac{d}{2}\right)\right]^2}\right]}{\left[-\left[x-\left(x'-\frac{d}{2}\right)\right]+\sqrt{\left[x-\left(x'-\frac{d}{2}\right)\right]^2+\beta_{yy'}{}^2+\left[z-\left(z'-\frac{d}{2}\right)\right]^2}\right]} \right\} - \right.$$

$$\left. \ln\left\{ \frac{4\left[-\left[x-\left(x'+\frac{d}{2}\right)\right]+\sqrt{\left[x-\left(x'+\frac{d}{2}\right)\right]^2+\beta_{yy'}{}^2+\left[z-\left(z'-\frac{d}{2}\right)\right]^2}\right]}{\left[-\left[x-\left(x'-\frac{d}{2}\right)\right]+\sqrt{\left[x-\left(x'-\frac{d}{2}\right)\right]^2+\beta_{yy'}{}^2+\left[z-\left(z'+\frac{d}{2}\right)\right]^2}\right]} \right\} \right\}$$

where

$$\alpha_{yy'} = \left[y-\left(y'+\frac{d}{2}\right)\right]$$

$$\beta_{yy'} = \left[y-\left(y'-\frac{d}{2}\right)\right]$$

(*A*.11)

$$\frac{G_{zz}(\vec{r}-\vec{r}')}{M_s} =$$

$$\left(\left\{\tan^{-1}\left[\frac{\left[x-\left(x'+\frac{d}{2}\right)\right]\left[y-\left(y'+\frac{d}{2}\right)\right]}{\alpha_{zz'}\sqrt{\left[x-\left(x'+\frac{d}{2}\right)\right]^2+\left[y-\left(y'+\frac{d}{2}\right)\right]^2+\alpha_{zz'}{}^2}}\right]+\tan^{-1}\left[\frac{\left[x-\left(x'-\frac{d}{2}\right)\right]\left[y-\left(y'-\frac{d}{2}\right)\right]}{\alpha_{zz'}\sqrt{\left[x-\left(x'-\frac{d}{2}\right)\right]^2+\left[y-\left(y'-\frac{d}{2}\right)\right]^2+\alpha_{zz'}{}^2}}\right]\right\}-\right.$$

$$\left.\left\{\tan^{-1}\left[\frac{\left[x-\left(x'+\frac{d}{2}\right)\right]\left[y-\left(y'-\frac{d}{2}\right)\right]}{\alpha_{zz'}\sqrt{\left[x-\left(x'+\frac{d}{2}\right)\right]^2+\left[y-\left(y'-\frac{d}{2}\right)\right]^2+\alpha_{zz'}{}^2}}\right]+\tan^{-1}\left[\frac{\left[x-\left(x'-\frac{d}{2}\right)\right]\left[y-\left(y'+\frac{d}{2}\right)\right]}{\alpha_{zz'}\sqrt{\left[x-\left(x'-\frac{d}{2}\right)\right]^2+\left[y-\left(y'+\frac{d}{2}\right)\right]^2+\alpha_{zz'}{}^2}}\right]\right\}\right)-$$

$$\left(\left\{\tan^{-1}\left[\frac{\left[x-\left(x'+\frac{d}{2}\right)\right]\left[y-\left(y'+\frac{d}{2}\right)\right]}{\beta_{zz'}\sqrt{\left[x-\left(x'+\frac{d}{2}\right)\right]^2+\left[y-\left(y'+\frac{d}{2}\right)\right]^2+\beta_{zz'}{}^2}}\right]+\tan^{-1}\left[\frac{\left[x-\left(x'-\frac{d}{2}\right)\right]\left[y-\left(y'-\frac{d}{2}\right)\right]}{\beta_{zz'}\sqrt{\left[x-\left(x'-\frac{d}{2}\right)\right]^2+\left[y-\left(y'-\frac{d}{2}\right)\right]^2+\beta_{zz'}{}^2}}\right]\right\}-\right.$$

$$\left.\left\{\tan^{-1}\left[\frac{\left[x-\left(x'+\frac{d}{2}\right)\right]\left[y-\left(y'-\frac{d}{2}\right)\right]}{\beta_{zz'}\sqrt{\left[x-\left(x'+\frac{d}{2}\right)\right]^2+\left[y-\left(y'-\frac{d}{2}\right)\right]^2+\beta_{zz'}{}^2}}\right]+\tan^{-1}\left[\frac{\left[x-\left(x'-\frac{d}{2}\right)\right]\left[y-\left(y'+\frac{d}{2}\right)\right]}{\beta_{zz'}\sqrt{\left[x-\left(x'-\frac{d}{2}\right)\right]^2+\left[y-\left(y'+\frac{d}{2}\right)\right]^2+\beta_{zz'}{}^2}}\right]\right\}\right)$$

where

$$\alpha_{zz'} = \left[z-\left(z'+\frac{d}{2}\right)\right]$$

$$\beta_{zz'} = \left[z-\left(z'-\frac{d}{2}\right)\right] \qquad (A.12)$$

After a change of variables $\vec{r} \equiv \vec{r} - \vec{r}'$, we obtain Eq. (2.26–33).